

Structural and kinetic studies of a copper
sensor protein in *Streptomyces lividans*

Tatiana de V. Porto

A thesis submitted for the degree of PhD in Biochemistry

School of Biological Sciences

University of Essex

Revised Version

21th October 2015

Abstract

The production of antibiotics, antifungal, enzymes and anti-tumoral agents of economical importance in *Streptomyces lividans* occurs during the copper-dependant morphological switch step of its distinct lifecycle. However, copper can be toxic to the cell if it is not well regulated, affecting copper homeostasis. The regulation of the concentrations of copper is performed by CsoR, a Cu(I)-metalloregulator of the CsoR/RcnR family, on upon Cu(I) binding, it dissociates from its own *csoR* regulon. This event leads to Cu(I) to be trafficked outside the cytosol via a CopZ chaperoning system. Although Cu(I)-bound structures of CsoR/RcnR family members have been solved, its still unclear how CsoR dissociates from DNA upon Cu(I) binding and how promiscuous its metal ion binding site is, i.e., if it other metals bind and trigger a similar allosteric response as Cu(I) does. Through a structural and kinetic approach, these questions were explored on this work, in order to give insights at atomic and mechanistic level in this metalloregulator family. A novel CsoR structure at pH 6 revealed a striking quasi-Cu(I) bound state, which provides important information on how CsoR may bind to DNA. A mechanism of metal binding to Cu(I) and a non-cognate metal, Ni(II) is proposed, with novel insights on metal selectivity and specificity in this poorly understood family of bacterial metalloregulators.

Acknowledgments

First of all, I would like to thank to my parents for their constant support throughout my life and especially during 5 years and 8 months that I was been based in the UK for my postgraduate studies, first at Masters level and now culminating with my PhD. My Dad, my ultimate hero, my close friend and who was with me on my side during the most difficult period of my PhD. He was the very first person in my life that introduced me into science as a child and has always supported my career. My Mum, who was extremely crucial on my formative school years, providing precious support at all times and has taught me how to stay strong in life throughout adversities. I would like to thank to my European family in Germany – Vania, Michael and Pedro Winterberg – who have welcomed me various times over there and even attended my MSc Biotechnology graduation in July 2011.

My sincere thank you to my PhD supervisor, Dr. Jonathan A.R. Worrall, who was my first and only choice when I had to switchover projects in August 2011 for my own (and my PhD's) sake. His research skills and support have been important to bring the best out of me to shine as a researcher. I am very grateful to his guidance, pushing me when needed so I could work harder to catch up with the tight and challenging PhD schedule in front of me. I want to thank my fellow members of the Worrall research group during my time in 5.08 - Dr. Badri Rajagopal, Dr. Katie Blundell, Amanda Chaplin, Benedict Tan, Oliver Deacon and Dr. Andreas Karsisiotis for everything I have learned at every level. I would like to thank fellow lab colleagues Dr. Richard Crooks, Dr.

Nicola Acerra, Dr. Demet Kekilli and Andreea Manole for being part of my lab journey as well.

Throughout the years working on my PhD project, I had the chance to work with extremely talented Professors and lecturers whose feedback and guidance were extremely important on my training. I want to thank Dr. Brandon Reeder, who was my choice as my supervisory board member, whose valuable feedback helped me to improve my academic and research skills. Dr. Mike Hough, which collaborated with me on my x-ray crystallography experiments and helped me to develop my structural biology skills. Professor Mike Wilson, with his valuable and timeless research expertise, who I was very lucky enough to work with during my kinetic experiments and learn a lot about research in general. Professor Glyn Stanway, who has always been helpful throughout different phases of my PhD. Professor Nelson Fernandez, whose years of experience has taught him how to advice PhD students through their academic marathon with the right mindset. Professor Chris Cooper, whose years and years of presenting his research to a non-specialist audience have been extremely valuable to me. Finally, Dr. Selwa Aslam, who opened the doors for me to have the chance to present my PhD research at the Molecular Cell and Biology Group seminar to my fellow School members in January 2015.

Very special thanks to the following Essex staff – Julie Snell, Amanda Clements and Emma Revill (School of Biological Sciences). and Vicky Djordjevic (Wellbeing Centre). You have been amazing!

During my time at Essex, I have met a lot of fellow students who have been part of my PhD journey. My best friend and fellow PhD candidate Nicola

Don - our friendship first started at the PG Room way back in 2012 and we are team NicTat at all times providing mutual support to each other at every level. My two friends which I have met through the Mature Students Society – Steph Driver and Ruth Raymer, with whom I have learned a lot outside my field of study with a creative writing feel.

My fellow mates and friends from RED Radio – The House of Student Radio at Essex - 2013/2014 and 2014/2015 academic years, especially Oliver Morris, Lee Stansfield (who I did supervise on his 3rd year project), Scott Ampleford + Phil Toms (Epic Lunchtime and Doctor Puppet project). With my radioshow SX Soundtracks (Reboot), I have shared the soundtrack of my uni years while learning how to cope with things when they go wrong in the studio. And it did help me on my lab duties and also improve my communication skills a lot!

My fellow Braziiian expat friends – Ulisses and Angela Terto, Andre Mazzari, Debora Braga Vieira, Rubens Araujo and Dr. Carolina Matos – no matter if you are a fellow postgraduate student/postdoc/lecturer, we have all made the decision to come abroad in the search of knowledge. Despite being an ocean away, I want to thank to my best friends Aurelio Moraes and Marcos Ferasso for their friendship and constant support.

This thesis is dedicated to my late uncle Altair Nunes Porto Filho (1942 – 2005) who was an inspiration and taught me to respect my personal limits in life in order to achieve my dreams through knowledge.

Finally, I want to share special two quotes from two non-academic people that I do admire. Their life stories have helped me so much to stay strong while writing up this thesis and sum my approach to it:

“... The designs in nature are light-years ahead of anything we could create” – Mike Oldfield, English musician and composer, creator of Tubular Bells (1973) on his autobiography Changeling (2007).

“Everything just fell into place. It was one of those magical things (...) it was a labour of love” – Peter Davison, English actor, who portrayed the Fifth Doctor in Doctor Who (1981 – 1984) discussing about his Doctor Who 50th Anniversary special project called The Five(ish) Doctors Reboot (2013) in a 2014 interview.

Table of Contents

- I) List of Figures...page 13
- II) List of Tables...page 20
- III) List of Abbreviations...page 23

Chapter 1 – *Streptomyces*, Metalloregulators, Copper and the Cu(I) sensor CsoR: an overview

1.1 *Streptomyces*: habitat and morphology...page 27

1.2 The Biology of Copper...page 29

1.2.1 Copper and Life...page 29

1.2.2 Copper in Biological Systems...page 29

1.2.3 Copper dependency on morphological development of *Streptomyces*...page 32

1.2.3.1. Introduction...page 32

1.2.3.2 Extracellular copper metallochaperones and copper-dependent morphogenesis in *Streptomyces lividans*...page 32

1.3 Metalloregulators (Metal Sensors)...page 35

1.3.1 Introduction...page 35

1.3.2 Metal Selectivity and Specificity...page 37

1.3.3. Metalloregulator Families...page 37

1.3.3.1 Introduction...page 37

1.3.3.2 ArsR/SmtB...page 38

1.3.3.3 DtxR...page 40

1.3.3.4 Fur...page 41

1.3.3.5 NikR...page 42

1.3.3.6. MerR...page 45

1.3.3.7. CopY...page 46

1.3.3.8 CsoR/RcnR...page 49

1.4 Current knowledge on *S. lividans* CsoR...page 58

1.4.1 Introduction...page 58

1.4.2 CsoR, the *csor* regulon and the chaperoning properties of CopZs...page 59

1.4.3. The interplay between CsoR and CopZs in copper homeostasis...page 59

1.4.4. Current copper homeostatic regulation model in *S. lividans*...page 60

1.4.5. *S. lividans* CsoR structure and its putative Cu(I) binding residues...page 62

1.4.6. Insights on DNA binding to CsoR...page 67

1.5 Aims of this PhD project...page 70

Chapter 2 - Conformational Switching in CsoR visualised by X-ray Crystallography

2.1 Introduction...page 73

2.2. Materials and Methods...page 75

2.2.1 Crystallisation and data collection...page 75

2.2.2. Structure determination and coordinates...page 76

2.2.3 Structural movies...page 76

2.3 Results and Discussion...page 77

2.3.1. An apo-CsoR structure displaying shape similarity to Cu(I)-CsoR...page 77

2.3.2. Rearrangement of Cys104 side chain disrupts the α 2-helical geometry and alters the rotation of predicted DNA binding residues...page 83

2.3.3 Conformational switching involves a concertina effect of the α 2-helix...page 86

2.3.4 Conformational switching induces an electrostatic redistribution of the tetrameric surface...page 87

2.3.5 The effect of pH on the conformational switching in *S. lividans* CsoR...page 92

Chapter 3 - Structural Characterisation of CsoR mutants important for metal ion binding

3.1 Introduction...page 96

3.2 Materials and Methods...page 99

3.2.1 Construction of the H103A and C104A CsoR mutants...page 99

3.2.2 Over-expression and purification of CsoR and mutants...page 103

3.2.3 Absorbance and circular dichroism (CD) spectroscopy...page 105

3.2.4 Electrospray ionisation mass spectrometry (ESI-MS)...page 106

3.2.5 Crystallisation and structural determination of CsoR mutants...page 106

3.2.6 Data processing and analysis...page 107

3.3 Results and Discussion...page 108

3.3.1 Initial characterisation of the H103A and C104A mutants...page 108

3.3.2 CD spectroscopy of wild-type CsoR and mutants...page 110

3.3.3 Crystallisation of CsoR mutants...page 114

3.3.5 Crystal structures of the C75A and C104A mutants of *S. lividans* CsoR...page 114

3.3.4.1 C75A pH 4 and pH 5 structures...page 114

3.3.4.2 C104A pH 5 and pH 6 structures...page 119

3.3.4.3 Structural changes at the putative Cu(I) binding site in CsoR are pH dependent...page 125

Chapter 4 - Kinetics and mechanism of metal ion binding to CsoR in *S. lividans*

4.1 Introduction...page 127

4.2 Material and Methods...page 131

4.2.1 Site-directed mutagenesis, over-expression and purification of *S. lividans* CsoR...page 131

4.2.2 Cu(I) sample preparation...page 131

4.2.3 Protein preparation...page 131

4.2.4 Cu(I) titrations monitored by UV-Vis absorption spectroscopy...page 132

4.2.5 Ni(II) titrations at equilibrium monitored by UV-Vis absorption spectroscopy...page 132

4.2.6 Electrophoretic mobility shift assay (EMSA)...page 133

4.2.7 Stopped-flow spectroscopy...page 133

4.3 Results and Discussion...page 135

4.3.1 Cu(I) Binding to CsoR mutants H103A and C104A...page 135

4.3.2 Cu(I) binding kinetics to *S. lividans* CsoR and mutants...page 138

4.3.3 Ni(II) binding to *S. lividans* CsoR and mutants...page 142

4.3.4 The kinetics of Ni(II) binding to WT CsoR and mutants...page 145

4.3.5 Metal displacement studies of *S. lividans* CsoR...page 150

**4.3.6 Mechanism of Cu(I) and Ni(II) binding to *S. lividans*
CsoR...page 155**

Chapter 5 - Major Conclusions

5.1 Concluding Remarks and Future Perspectives...page 160

References...page 165

Appendix...page 185

**Structural insights into conformational switching in the copper
metalloregulator CsoR from *Streptomyces lividans***

Tatiana V. Porto, Michael A. Hough and Jonathan A. R. Worrall

Acta Cryst. (2015). D71, 1872–1878

I) List of Figures

Chapter 1 – *Streptomyces*, Metalloregulators, Copper and the Cu(I) sensor CsoR: an overview

Figure 1.1 - The lifecycle of *Streptomyces*...page 28

Figure 1.2 - The impact of dependency of copper on the morphological development of *S.lividans* on R5 media (medium containing yeast extract and glucose) plates...page 34

Figure 1.3 – The ribbon-helix-helix structure of *E.coli* NikR-DNA complex...page 44

Figure 1.4 – *E.coli* Cu(I)-CueR and its winged helix (helix-turn-helix DNA binding domain...page 47

Figure 1.5 - The structure of *E.coli* Cu(I)-CueR on the side...page 48

Figure 1.6 - The apo structure of *Thermus thermophilus* CsoR tetramer...page 54

Figure 1.7 - The apo structure of *Thermus thermophilus* CsoR formed by an antiparallel α -helix bundle, side view...page 55

Figure 1.8 - The holo structure of *Geobacillus thermodenitrificans* Cu(I)-CsoR represented as a dimer...page 56

Figure 1.9 - The holo structure of *Geobacillus thermodenitrificans* Cu(I)-CsoR represented as a dimer, side view...page 57

Figure 1.10 - The current Cu homeostasis model in *S. lividans*, represented by the CsoR regulon and its pathways...page 61

Figure 1.11 – *S. lividans* CsoR apo structure at pH 4, formed by four α -helical monomers, represented in different colours...page 64

Figure 1.12 - The putative Cu(I) binding residues in *S. lividans* CsoR...page 65

Figure 1.13 - C α superposition of the Cu(I) binding site of *M. tuberculosis* Cu(I)-CsoR (red) with *S. lividans* CsoR (blue)...page 66

Figure 1.14 – The proposed CsoR/DNA binding model...page 69

Chapter 2 - Conformational Switching in CsoR visualised by X-ray Crystallography

Figure 2.1 - Molecular surface representations of the homotetramer structure of *S. lividans* CsoR determined from crystals grown at pH 4 (left side, top and bottom, PDB accession number: 4ADZ) and (B) pH 6 (right side, top and bottom, PDB accession number: 4UIG)...page 81

Figure 2.2 - The inter-protomer Cu(I)-binding site in the pH 6 crystal structure of apo *S. lividans* CsoR...page 82

Figure 2.3 - Conformational changes at one of the Cu(I) binding sites (gray pH 4 and blue pH 6) in the *S. lividans* CsoR homotetramer...page 83

Figure 2.4 - Superposition of *S. lividans* CsoR at pH 4 (blue) with pH 6 (orange) structures focused on both predicted DNA and Cu(I) binding sites...page 85

Figure 2.5 - Cross-tetramer interface interactions for (A) the Arg102 side-chain upon interaction with Asp117 and (B) Arg129 and Thr80 (dashed lines) in the quasi Cu(I)-bound structure (blue, pH 6)...page 91

Figure 2.6 – (Top) C α superposition of the Cu(I) binding site of *M. tuberculosis* Cu(I)-CsoR (dark green) with *S. lividans* CsoR pH6 apo structure (orange). In the ‘quasi’-Cu(I) bound state in *S. lividans* CsoR...page 94

Chapter 3 - Structural Characterisation of CsoR mutants important for metal ion binding

Figure 3.1 - *S. lividans* CsoR sequence used as a template for site-directed mutagenesis using Quikchange method...page 100

Figure 3.2 - (A) G75 gel filtration elution profile for CsoR mutant C104A. Buffer F (50mM Tris pH 8, 150 mM NaCl, 2mM DTT and 4 mM EDTA. (B) Coomassie stained 15% SDS-PAGE gel for G75 Sephadex column fractions of CsoR^{Sl} mutant C104A...page 109

Figure 3.3 - Far-UV circular dichroism spectra for *S. lividans* WT CsoR (black) and C75A (red), H100A (light green), H103A (blue) and C104A (light blue) mutants at 20°C...page 111

Figure 3.4 - Thermal denaturation spectra at 222 nm for *S. lividans* WT CsoR and C75A (red), H100A (light green), H103A (blue) and C104A (light blue) mutants...page 112

Figure 3.5 - Crystal structures of *S. lividans* CsoR 1.72 Å C75A pH 4 (left) and 1.93 Å C75A pH 5 (right) mutants...page 116

Figure 3.6 - (A) Superposition of *S. lividans* CsoR pH 4 (green) with C75A pH 4 (orange). (B) Superposition of *S. lividans* CsoR pH 4 (green) with C75A pH 5 (pink). For Cu(I) binding, Cys104 must undergo into a “locked” position and closer to Cys75. (C) Interruption or a kink is observed at α -helix 2 for C75A pH 5 (purple), which is absent on CsoR pH 4 (green)...page 117

Figure 3.7 - Superposition of *S. lividans* CsoR pH 4 (light violet) with C75A pH 4 (deep teal) and pH 6 (orange)...page 118

Figure 3.9 - Structures of 2.02 Å C104A pH 5 structure (above) and 2.05 Å C104A pH 6 (below)...page 121

Figure 3.10 - Superposition of CsoR pH 4 (light purple) with C104A pH 5 (light green)...page 122

Figure 3.11 - Superposition of CsoR pH 4 (light purple) with C104A pH 6 (light red)...page 123

Chapter 4 - Kinetics and mechanism of metal ion binding to CsoR in *S. lividans*

Figure 4.1 – The structural and metal binding features of *Streptomyces lividans* CsoR...page 130

Figure 4.2 – Anaerobic UV-Vis absorption difference spectrum (top) and binding isotherm (bottom) at 240 nm of 36 μ M H103A mutant ...page 136

Figure 4.3 – Anaerobic UV-Vis absorption difference spectrum (top) and binding isotherm (bottom) at 240 nm of 40 μ M C104A mutant ...page 137

Figure 4.4 - Stopped-flow kinetics of Cu(I) binding to *S. lividans* CsoR...page 140

Figure 4.5 - Spectroscopic and regulatory properties of Ni(II) binding to *S. lividans* CsoR...page 144

Figure 4.6 - Stopped-flow kinetics of Ni(II) binding to *S. lividans* WT CsoR...page 148

Figure 4.7 - Stopped-flow kinetics of Ni(II) binding to *S. lividans* CsoR mutants...page 149

Figure 4.8 - Displacement studies for *S. lividans* CsoR...page 153

Figure 4.9 - Displacement studies for *S. lividans* CsoR mutant H103A...page 154

Figure 4.10 - Mechanism of Cu(I) and Ni(II) binding to *S. lividans* CsoR...page 158

II) List of Tables

Chapter 1 – Streptomyces, Metalloregulators, Copper and the Cu(I) sensor CsoR: an overview

Table 1.1 – CsoR/RcnR clades I to VII, organised by phylogenetic origin (adapted from Chang *et al*, 2014)...pages 51 and 52

Chapter 2 - Conformational Switching in CsoR visualised by X-ray Crystallography

Table 2.1 - Crystallographic data collection and processing statistics for apo *S. lividans* CsoR pH 6 structure...page 80

Chapter 3 - Structural Characterisation of CsoR mutants important for metal ion binding

Table 3.1 - The X-Y-Z primary coordination sphere residues in CsoR/RcnR family. The asterisk (*) indicates that Cu(I) was found to be coordinated to these residues on the crystal structure. (Taken from Dwarakanath *et al*, 2012; Chang *et al*, 2014 and Foster *et al*, 2014b)...page 97

Table 3.2 - Site-directed mutagenic reverse and forward primers used to construct *S. lividans* CsoR mutants (A) H103A and (B) C104A. The nucleotides in red indicate the desired nucleotide change...page 101

Table 3.3 - PCR program set up used for the amplification of genes that encodes *S. lividans* mutants H103A or C104A using the Quikchange site-directed mutagenesis method...page 102

Table 3.4 - Crystallisation conditions for CsoR mutants C75A and C104A at initial screening stage using 96-well robot plates...page 112

Table 3.5 - Crystallisation conditions for CsoR mutants C75A and C104A on 24-well optimisation plates...page 113

Table 3.6 - Data collection and processing statistics of WT CsoR, C75A and C104A mutants obtained through Scala (Evans, 2006) and Refmac5 (Murshudov *et al*, 2011) on the CCP4i suite...page 124

Chapter 4 - Kinetics and mechanism of metal ion binding to CsoR in *S. lividans*

Table 4.1 - Stopped-flow determined average pseudo first-order rate constants and amplitude change at 250 nm for Cu(I) binding to *S. lividans* CsoR and mutants (20 °C, pH 7.4)...page 141

Table 4.2 - Stopped-flow determined average pseudo first-order rates constants for Ni(II) binding to *S. lividans* CsoR and mutants (20 °C, pH 7.4)...page 147

Table 4.3 - Stopped-flow determined pseudo first-order rate constants for the displacement of Ni(II) from WT CsoR and the H103A mutant of *S. lividans* CsoR with Cu(I) (20 °C, pH 7.4). Standard deviations are given in parenthesis...page 152

III) List of Abbreviations

(In order of appearance in this thesis)

GOE - Great Oxidation Event

S. lividans - *Streptomyces lividans*

BCDA - Bathocuproinedisulfonic acid

Sco – Synthesis of cytochrome c oxidase

CcO - Cytochrome c oxidase

ECuC – Extracellular Cu chaperone

ArsR - Arsenic resistance repressor

S. aureus - *Staphylococcus aureus*

M. tuberculosis – *Mycobacterium tuberculosis*

Listeria monocytogenes - *L. monocytogenes*

DtxR - Diphtheria toxin repressor

C. diphtheriae - *Corynebacterium diphtheriae*

GC – Guanine-cytosin

Fur - Ferric uptake regulator

PDB – Protein Data Bank

MerR – mercury resistance

SAXS - small-angle X-ray scattering

CueR - Cu efflux regulator

E. coli - *Escherichia coli*

B. subtilis - *Bacillus subtilis*

CsoR - Copper-sensitive operon repressor

CstR - CsoR-like sulfurtransferase repressor

Cys – Cysteine

His – Histidine

Leu – Leucine

Thr – Threonine

Ser – Serine

Gly – Glycine

Lys – Lysine

Arg – Arginine

G. thermodenitrificans - *Geobacillus thermodenitrificans*

T. thermophilus - *Thermus thermophilus*

Met – Methionine

EMSA - Electrophoretic mobility assays

C α - Carbon alpha

Å – Ångstrom

Tyr – Tyrosine

Gln – Glutamine

Ni-NTA – Nickel-nitrilotriacetic acid

NMR – Nuclear Magnetic Resonance

WT – wild-type

T_m – Melting temperature

dNTPs – Deoxyribonucleotide triphosphate

DMSO – Dimethyl sulfoxide

LB – Luria-Bertani

OD₆₀₀ - optical density at 600 nm

IPTG - isopropyl- β -D-1-thiogalactopyranoside

NaCl – Sodium chloride

Tris - Tris(hydroxymethyl)aminomethane

EDTA – Ethylenediaminetetraacetic acid

Na₃PO₄ – Sodium phosphate

DTT – dithiothreitol

SDS-PAGE – Sodium Dodecyl Sulphate-Polyacrylamide gel electrophoresis

CD – Circular Dichroism

F_h - fractional helicity

ESI-MS - Electrospray ionisation mass spectrometry

K – Kelvin

Da – Dalton

MRE - mean residue ellipticity

T_m – thermal melt temperature

MES - 2-(N-morpholino) ethanesulfonic acid

CuCl – copper (I) chloride

MOPS- 3-(N-morpholino)propanesulfonic acid

BCA - bicinchoninic acid

HEPES - 4-(2-hydroxyethyl)-1-piperazineethanesulfonic acid

Ni₂SO₄ – Nickel (II) sulphate

SVD - Singular value decomposition

Chapter 1

Streptomyces, Metalloregulators, Copper and the Cu(I) sensor CsoR: an overview

1.1 Streptomyces: habitat and morphology

Within *Actinomycetes*, *Streptomyces* are Gram-positive bacteria with a high GC genome content, which can be found as saprophytes living freely in soils, rizosphere of plant roots and tissues, aquatic sediments and even marine environments with an ecological importance (Waksman and Henrici, 1943; Chalis and Hopwood, 2003; Olano *et al*, 2011; van Wezel and McDowall, 2011).

Many of the secondary metabolites produced have biotechnological applications in human welfare (antibiotics, immunosuppressives, antifungal, antihelmintic and anti-tumoral agents) and agriculture, such as growth promoters and herbicides (Bibb, 1996; Worrall and Vijgenboom, 2010; van Wezel and McDowall, 2011). In the 1950s and 1960s, between 70-80% of the discovered antibiotics for bacterial and fungi-related diseases were isolated from different *Streptomyces* species. With now more than 7,600 different *Streptomyces*-originated compounds, it is a primary leader in pharmaceutical exploration (Bérdy, 2005; Butler, 2005, Olano *et al*, 2011).

As one of the model organisms in bacterial morphology and physiological development studies, the distinguishing feature of *Streptomyces* lies in their mycelium life cycle, which resembles lower eukaryotes such as fungi to a certain extent (Bibb *et al*, 1996; Worrall and Vijgenboom, 2010; van Wezel and McDowall, 2011). From a germinated spore, three distinct developmental stages are observed in streptomycetes: the formation of a branched vegetative mycelium formed by a complex and tight hyphae matrix, with subsequent aerial mycelium formation and then sporulation (Keijser *et al*, 2000; Anderson and Wellington, 2001; Worrall and Vijgenboom, 2010). The

production of secondary metabolites in *Streptomyces* occurs just before or concomitantly with the morphological switch from the vegetative to aerial mycelium phase (Figure 1.1).

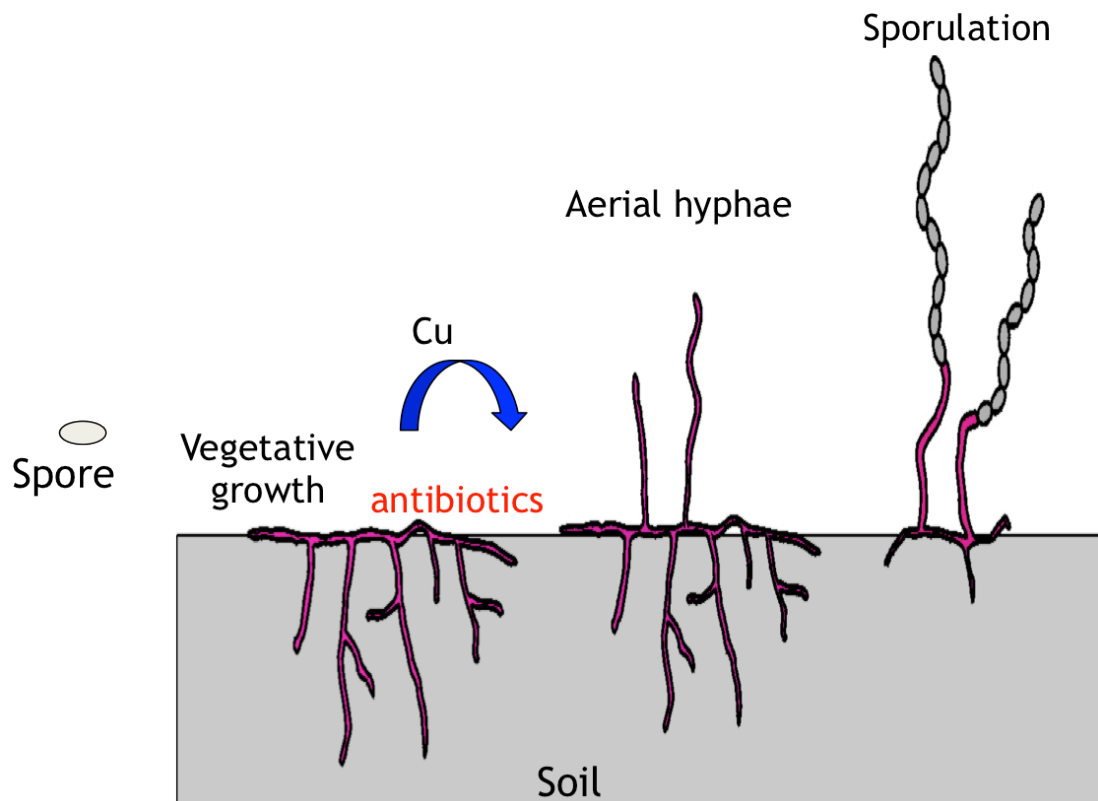


Figure 1.1 - The lifecycle of *Streptomyces*. A spore germinates in the soil and grows out as vegetative mycelium forming a dense network. Upon limited nutrient conditions, an aerial mycelium develops, feeding from its own vegetative part, with further sporulation. The production of antibiotics, anti-fungal and anti-tumoral agent, which is copper dependent, occurs during the morphological switch from vegetative to aerial mycelium. (Figure courtesy of Dr. Jonathan A.R. Worrall).

1.2 The Biology of Copper

1.2.1 Copper and Life

Copper is one of the most important transition (d-block) metals both in nature and everyday lives. First evidence of copper mining have been dated back to 5000 years ago, which puts copper as the first metal to be worked by humans (Osman and Cavet, 2008). During the Bronze Age in pre-historical times, copper was used in many applications, from tools, weapons, electric equipment and motors (Osman and Cavet, 2008). With a concentration of 68 ppm in the Earth's crust, copper can be found both in ores such as chalcopyrite (CuFeS_2), chalcocite (Cu_2S), cuprite (Cu_2O) and malachite ($\text{Cu}_2\text{CO}_3(\text{OH})_2$) (Solioz and Stoyanov, 2003; Osman and Cavet, 2008). The antimicrobial properties of copper have been known since Egyptian times for treating water and chest infections, with the subsequent medical use of copper firstly by the Greeks and Aztec civilizations, which still continues to the present day, with the use of copper surfaces in healthcare facilities (Hodgkinson and Petris, 2012).

1.2.2 Copper in Biological Systems

With the advent of an oxygen-rich atmosphere post-Great Oxidation Event (GOE) 2.4-2.7 billion years ago, copper became bioavailable, combined with the development of an oxidative metabolism (Rensing and Grass, 2003; Solioz *et al*, 2010; Dupont *et al*, 2011). Both eukaryotes and prokaryotes have copper as an essential micronutrient, which is the second transition metal in terms of biological importance after iron (Solioz and Stoyanov, 2003; Solioz *et al*, 2010). Copper has two distinct redox states with a high binding affinity for

biomolecules, Cu(I) and Cu(II). The Cu(I) ion (cuprous, with a $3d^{10}$ shell) normally bonds to sulfhydryl groups due to its soft metal character and exists in high-affinity complexes as a co-factor (e.g. Cu(I) ATPases and Cu(I) metallochaperones) (Solioz and Stoyanov, 2003). On the other hand, the Cu(II) ion (cupric, with a $3d^9$ shell) either forms stable bonds with nitrogen or labile ones with oxygen and even non-complexed Cu(II) ions can be found in neutral aqueous solutions (Rensing and Grass, 2003; Solioz and Stoyanov, 2003; Dupont *et al*, 2011). Cu(II) also binds tightly to sulphur and nitrogen-ligand metalloproteins, while Cu(I) is equally competitive in a reducing cytosolic environment (Waldron and Robinson, 2009).

The biological cycling between Cu(I) and Cu(II) allows enzymes or proteins harnessing copper to take part in redox reactions within the cell (Solioz and Stoyanov, 2003; Ma *et al*, 2009a; Worrall and Vijgenboom, 2010). A major drawback of transition metals is their potential toxicity within the cell and with copper it is no different, with known toxic effects in bacteria and other organisms, such as possible links to pathologic processes in humans such as Alzheimer's, Parkinson's and Wilson's diseases, caused by excessive copper levels (Gaggelli *et al*, 2006; Macomber and Imlay, 2009; Solioz *et al*, 2010). In Wilson's disease, copper is not properly pumped from the liver into the bile due to a genetic mutation that affects its efflux pathway (Macomber *et al*, 2007). In an unbound (unligated) state the Cu(I)/Cu(II) redox couple makes copper toxic to the cell, even if there are small changes to Cu(I) cytosolic concentrations (Ma *et al*, 2009a). Cu(I) ions are catalysts for Fenton-like chemistry reactions, with the production of highly reactive oxygen, superoxide, hydroxyl and sulfhydryl species that can be deleterious to the cell, causing

damage to biomolecules such as DNA, proteins and lipids; (Solioz and Stoyanov, 2003; Giedroc and Arunkmar, 2007; Osman and Cavet, 2008; Ma *et al*, 2009b; Solioz *et al*, 2010; Tottey *et al*, 2012). Meanwhile in *E. coli*, it is suggested that proteins can be damaged by the coordination of Cu(I) to sulfur atoms present in them (Macomber and Imlay, 2009), while DNA damage caused by reactive oxygen species in vivo is not induced by copper (Macomber *et al*, 2007). Furthermore, it is also now becoming apparent that copper toxicity also arises from its ability to outcompete iron in the assembly of Fe/S clusters (Macomber and Imlay, 2007). Therefore in bacteria tightly controlled copper homeostatic systems have evolved, which are based on three elements: binding, transport and regulation of copper-dependant gene expression (Solioz *et al*, 2010).

1.2.3 Copper dependency on morphological development of *Streptomyces*

1.2.3.1. Introduction

Copper ions play a prominent role on the morphological development of certain *Streptomyces* species, with *Streptomyces lividans* the best studied example. Morphological studies in *Streptomyces lividans* using a copper rich-medium demonstrated that copper has a major role in accelerating morphological differentiation compared to *Streptomyces coelicolor*. However, in the presence of a specific copper chelator BCDA (bathocuproinedisulfonic acid), a developmental block was observed and it was only with the addition of Cu(II) to the medium that it returned to normality (Keijser *et al*, 2000). This development block arrests the formation of aerial hyphae and stalls development at the vegetative stage (Figure 1.2). These observations suggested that copper proteins and enzymes must play a role in this copper-dependency (Worrall and Vijgenboom, 2010).

1.2.3.2 Extracellular copper metallochaperones and copper-dependent morphogenesis in *Streptomyces lividans*

Sco and ECuC are two extracellular copper chaperones in *S. lividans*, which have an involvement in the copper-dependent morphological development stage (Blundell *et al*, 2013; Blundell *et al*, 2014). Sco (synthesis of cytochrome c oxidase) is involved on initiating the morphological development switch from vegetative mycelium to aerial hyphae and also interplays with CcO (cytochrome c oxidase) as a co-factor facilitator. Upon lower copper concentrations, knockout studies with a Δsco mutant revealed

stagnation at morphological switch level and a considerable decrease on CcO activity; at higher copper concentrations, wild type levels of both morphological switch and CcO activity were observed, as a sign of not being Sco-dependent (Blundell *et al*, 2013).

ECuC (extracellular Cu chaperone) is a Cu(I) chaperone that is involved on an unidirectional Cu(I) trafficking pathway with Sco. ECuC has the ability to transfer Cu(I) to Sco through the formation of a transient electrostatic complex on which one of the cysteines from the copper binding motif of Sco (Cys86) participates in a ligand-exchange mechanism. At lower exogenous copper concentrations *in vivo*, studies involving genetic knockouts Δsco , $\Delta ecuc$ and $\Delta sco/ecuc$ revealed that ECuC is not required for morphological development, but CcO activity is affected by reduction in comparison to wild-type (Blundell *et al*, 2014).

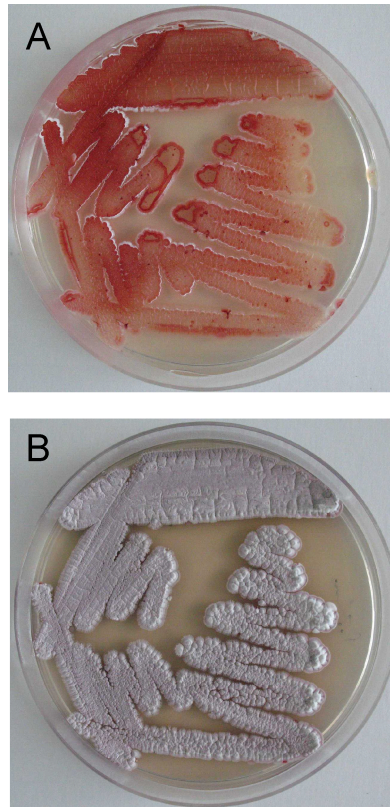


Figure 1.2 - The impact of dependency of copper on the morphological development of *S.lividans* on R5 media (medium containing yeast extract and glucose) plates. (A) In the presence of bathocuproin disulfonic acid (a Cu-specific chelator), development is restricted to the vegetative growth phase only. (B) With the addition of 0.2 mM Cu^{1+/2+} to the media, the full development occurred until sporulation that was characterised by the grey ‘fluffy’ colonies (Worrall and Vijgenboom, 2010).

1.3 Metalloregulators (Metal Sensors)

1.3.1 Introduction

Based on the duality of essential macronutrient versus toxicity within the cell, bacteria have evolved a tightly controlled copper homeostatic system. Foundations of copper availability to the cell are dependent on the concerted interplay between various metal receptors (transporters, chaperones, metalloregulators) working on binding, transport and regulation of copper-dependant gene expression (Davis and O'Halloran, 2008; Solioz *et al*, 2010). The coordination of copper in proteins does influence its redox potential, which varies between 200 and 800 mV (Solioz *et al*, 2010). Due to its strongly reducing potential, the bacterial cytosolic environment has an overcapacity to chelate Cu(I) ions, which is performed by high affinity Cu(I)-specific sensing proteins (Giedroc and Arunkmar, 2007). All cytosolic Cu(I) has to be complexed with low molecular weight ligands or by metallochaperones to prevent catalysing the production of reactive oxygen species, which can be deleterious to the cell (Giedroc and Arunkmar, 2007; Ma *et al*, 2009a).

The tight regulation of metal ion homeostasis in bacteria is performed by transcriptional factors denominated as metalloregulatory proteins (or metal sensors) that direct an adequate response to control intracellular conditions (Penella and Giedroc, 2005; Hobman, 2007; Ma *et al*, 2009b). The bacterial cytosol is a metal-controlled environment in which the actions of metalloregulators help to maintain buffered metal ion concentrations (Waldron and Robinson, 2009; Foster *et al*, 2014a). Metalloregulators have the ability to bind to a specific d-block/transition metal ion (or ions) they 'sense' in the cytosol (hence the name metal sensor) based on the organism 'metallome'

(Giedroc and Arunkumar, 2007). Fluctuation in the set-metal concentration of the cytosol leads to the initiation of a response from the appropriate metalloregulator. The metal-dependent response in metalloregulators leads them to interact with specific DNA sequences located either on the promoter or nearby regions, which regulates protein expression (Hobman, 2007; Rubino and Franz, 2012). Structurally speaking, a metalloregulator has two very distinct binding regions. One of these regions is specific to bind to the all DNA sequences on which the metalloregulator regulates within its regulon. A second binding region is metal-specific, on which the metal(s) sensed by a metalloregulator binds to it.

A major challenge for any metalloregulator protein is to overcome the trend established by the Irving-Williams series of natural stability of divalent metal ions based on physical and chemical properties - $Mn < Fe < Co < Ni < Cu > Zn$, so it can then bind to its/their cognate metal(s) with a subsequent allosteric response. A specific and quick metal recognition is then achieved, in order to fulfill the necessities of the cell to avoid metal intoxication (Irving and Williams, 1948; Hobman, 2007; Waldron and Robinson, 2009, Foster *et al*, 2014a). It is in the conversion from apo (metal-free) to holoform (protein-metal complex), where the metal acts as a cofactor (Waldron and Robinson, 2009) that the allosteric ability of metalloregulators surfaces, as they are fully able to control the intracellular d-block metal ion concentration to threshold levels by the activation, repression or derepression of genes involved in membrane transport and metal trafficking proteins such as P_{1B} -type ATPases and metallochaperones in efflux systems (Penella and Giedroc, 2005; Waldron

and Robinson, 2009; Ma *et al*, 2009a, Ma *et al*, 2009b, Reyes-Caballero *et al*, 2011).

1.3.2 Metal Selectivity and Specificity

The relationship between metalloregulators and their sensed metal ion(s) is regulated by both metal selectivity and specificity, which are intrinsically related. The metal selectivity of a metalloregulator can be defined as the discrimination of the metal(s) that bind(s) to the metalloregulator metal site(s), while metal specificity is linked to the cognate metal(s) that when it binds to a metalloregulator, trigger(s) an allosteric effect that subsequently leads to a transcriptional response in metal ion homeostasis. The coordination chemistry of metalloregulators has a considerable but not definite influence on metal selectivity, but metal specificity is still poorly understood (Penella *et al*, 2003; Iwig *et al*, 2008).

1.3.3. Metalloregulator Families

1.3.3.1 Introduction

Seven major metalloregulator families have been reported in the literature so far, named after its founding members: ArsR-SmtB, MerR, DtxR, Fur, NikR, CopY and CsoR-RcnR (Ma *et al*, 2009b; Waldron and Robinson, 2009). These major families have been classified by their transcriptional response upon binding of their sensed metal(s). For de-repressors (e.g. ArsR-SmtB, CsoR-RcnR, CopY families), transcription is repressed after the formation of the holo-metalloregulator form. Co-repressors (e.g. Fur, NikR and DtxR families) depend on their sensed metal(s) to bind to them so they can bind to their operator/regulon. When a sensed metal binds to an activator (e.g.

MerR family), a conformational change occurs within the structure, which allows transcription to happen.

Currently known cytosolic copper metalloregulators are CueR (a MerR family member) in *E. coli* (Otten *et al*, 2000; Stoyanov *et al*, 2001; Osman and Cavet, 2008), CopY (Odermatt and Solioz, 1995) in *E. hirae* and the CsoR/RcnR family initially identified in *M. tuberculosis* (Liu *et al*, 2007). CopY and CsoR, although structurally distinct from CueR, function as the primary copper metalloregulators in species that lack CueR (Osman and Cavet, 2008; Solioz *et al*, 2010).

1.3.3.2 ArsR/SmtB

The ArsR/SmtB or ArsR metalloregulator family comprises a major list of winged helix (a dimeric structure which features a helix-turn-helix DNA binding motif) transcriptional repressors, which are involved also in coping with heavy metal stress and their related resistance mechanisms in the cytosol – efflux/scavenging/detoxification (Busenlehner *et al*, 2003, Wang *et al*, 2005; Ma *et al*, 2009b). ArsR/SmtB family members have demonstrated a varied metal sensing repertoire despite their common ancestry, from essential metals such as Cu(I), Zn(II) and Ni(II) to highly environmental pollutants like As(III), Cd(II) and Pb(II), as a result of their distinct and partially overlapping metal-binding motifs (Busenlehner *et al*, 2002; Liu *et al*, 2004; Ma *et al*, 2009b).

The founding members are *E. coli* ArsR arsenic resistance repressor (Wu and Rosen, 1993) and SmtB from *Synechococcus* PCC 7942 (Morby *et al*, 1993). In *E. coli*, ArsR is a trans-acting metalloregulator that binds to the

arsenical resistance *ars* operon with specificity, which triggers a repressive response under arsenic Figoxyanions (Wu and Rosen, 1993). In *Synechococcus* PCC 7942, SmtB binds to the *smt* operator-promoter sequence, resulting on a repressive transcriptional response upon the Zn(II)-regulated *smtA* gene that encodes a class II metallothionein; dissociation occurs when Zn(II) binds to StmB (Morby *et al*, 1993; Cook *et al*, 1998). Multiple sequence alignment for *Synechococcus* PCC 7942 SmtB revealed a similarity with ArsR from *E. coli* and *Staphylococcus aureus* CadC (Morby *et al*, 1993). The crystal structure of SmtB from *Synechococcus* PCC 7942 revealed a winged helix dimer with a helix-turn-helix DNA binding motif and four suggested Zn(II) binding regions per monomer (Cook *et al*, 1998, Busenlehner *et al*, 2003).

Within ArsR/StmB metalloregulators, the diversity of sensed metals by their members is strongly related to their distinct types of metal binding sites. The classification of ArsR/SmtB metal binding sites is based on individual member reports of their reported or predicted secondary structure. The α 3/N-terminal α 3N sensors comprises of all reported ArsRs, *Listeria monocytogenes* CadC and *Staphylococcus aureus* pl258 CadC Cd(II)/Pb(II)/Zn(II) sensor (Busenlehner *et al*, 2003; Ye *et al*, 2005, Ma *et al*, 2009b). Highly polarised or thiophilic metals such as Cd(II) and Pb(II) binds to the α 4C site of *Mycobacterium tuberculosis* CmtB (Cavet *et al*, 2003; Banci *et al*, 2007; Ma *et al*, 2009b). The α 5/C-terminal α 5C sensors feature ArsR/SmtB founder *Synechococcus* SmtB (Busenlehner *et al*, 2003), *M. tuberculosis* Ni(II)/Co(II) sensor NmtR (Cavet *et al*, 2002), *S. aureus* Zn(II) sensor CzrA (Eicken *et al*, 2002, Arunkamar *et al*, 2009) and *M. tuberculosis* NmtR (Busenlehner *et al*,

2003; Lee *et al*, 2012). In *M. tuberculosis*, KmtR is a Ni(II)/Co(II) sensor that has a α 5-3 metal binding site (Campbell *et al*, 2007). In the *Oscillatoria brevis* Zn(II) sensor BxmR, its versatile α 3N metal coordination site also binds Cu(I)/Ag(I) with an allosteric response (Liu *et al*, 2004; Liu *et al*, 2008).

1.3.3.3 DtxR

This family of metalloregulators can be divided into two major subfamilies: DtxR-like sensors and MntR-like sensors. DtxR-like sensors are named after the diphtheria toxin repressor DtxR from *Corynebacterium diphtheriae* and it also includes IdeR from *M. tuberculosis* and SirR in staphylococci (Schmitt and Holmes, 1994; Andrews *et al*, 2003). In *C. diphtheriae*, DtxR binding to *tox* operator is Fe(II)-dependant and has strong links to its virulence; under higher Fe (II) concentrations, transcription is inhibited (Schmitt and Holmes, 1994; Chen *et al*, 2000; Spering *et al*, 2003, D'Aquino *et al*, 2005). In broader terms, DtxR has an important role in iron acquisition in low GC Gram-positive and a Gram-negative bacterium as Fur has for *E. coli*, although there is not a clear homology between each other (Schmitt and Holmes, 1994, Que and Helmann, 2000; Hantke 2001, Andrews *et al*, 2003).

X-ray crystallography data for DtxR revealed three domains, first an N-terminal DNA-binding domain with a winged helix shape (helix-turn-helix), a central dimerization metal domain and a C-terminal SH3-like domain (Glasfeld *et al*, 2003) which lacks a specific function so far, but it does not affect DNA binding and neither is present in other DtxR family members such as TroR from *Treponema pallidum* (Posey *et al*, 1999; Que and Helmann, 2000;

D'Aquino *et al*, 2005; Andrews *et al*, 2003). DtxR has two distinct metal sites, a primary one that is crucial to DNA binding and a secondary one that critically stabilises the repressor (D'Aquino *et al*, 2005).

MntR Mn(II) like sensors are named after *Bacillus subtilis* Mn(II)-sensor MntR, which is distantly related to DtxR in homologue terms (Que and Helmann, 2000). Mn(II)-MntR represses MntH, a Mn(II) ABC-type transporter that is active under low Mn(II) intracellular concentrations (Que and Helmann, 2000). The structure of MntR revealed similarities to DtxR, apart from the C-terminal SH3-like domain that it is only present in DtxR (Glasfeld *et al*, 2003).

1.3.3.4 Fur

While DtxR is the prototype Fe(II) metalloregulator in many high CG Gram positive bacteria such as *Corynebacterium*, *Mycobacterium* and *Streptomyces*, Fur family members are the equivalent for many Gram-positive bacteria in iron homeostasis, including human pathogens such as *Salmonella*, *Vibrio* and *Pseudomonas* (Escolar *et al*, 1999, Hantke, 2001, Andrews *et al*, 2003, Gueldon and Helmann, 2003). Its founding member, the ferric uptake regulator from *E. coli*, has a similar regulation model compared to DtxR in iron homeostasis by controlling global iron concentrations within the cell, from uptake to iron storage proteins expression and iron-utilizing enzymes (Pohl *et al*, 2003; Lee and Helmann, 2007). Fe(II)-Fur acquires a configuration that interacts with a specific target operator sequence known as 'iron box' or Fur boxes, leading to a protein-DNA complex with an α -helical DNA-binding domain that resembles DtxR, that represses the transcription of almost all Fe(II)-dependant genes and operons (Escolar *et al*, 1999; Pohl *et al*, 2003).

In structural terms, the N-terminal of Fur has a winged helix motif with a distinct turn, while its C-terminal has two metal sites, one for Fe(II) and other for Zn(II), which are important in the dimerisation process (Hantke, 2001). The crystal structure of *Pseudomonas aeruginosa* Zn(II) Fur revealed that the Zn(II) site is critical for protein structure, whereas the second metal site can be occupied by Fe (II) and trigger a transcriptional regulation response (Pohl *et al*, 2003). In *B. subtilis*, Zur is a Fur paralogue that senses Zn(II) and represses Zn(II) uptake systems, while PerR is a peroxide sensor whose DNA binding is Mn(II) or Fe(II) dependant (Moore and Helmann, 2005; Traoré *et al*, 2006).

1.3.3.5 NikR

This nickel-responsive metalloregulator family is named after the transcriptional regulator NikR from *E. coli*, which resembles Fur or DtxR metalloregulators in terms of functionality regarding metal uptake metabolism (De Pina *et al*, 1999). *E. coli* NikR is encoded by the *nikR* gene, which is responsible for the regulation of *nikABCDE* operon that encodes an ABC transporter responsible for nickel uptake in *E. coli* with a repressive role under high nickel concentrations (De Pina *et al*, 1999; Schreiter *et al*, 2003; Dosanjh and Michel, 2006).

The most distinguishable feature of NikR lies in its unique ribbon-helix-helix structure, first predicted (Chivers and Sauer, 1999) and then confirmed through its apo-NikR crystal structure, which features a dimeric N-terminal ribbon-helix-helix DNA-binding domains attached together through a tetrameric C-terminal nickel-regulatory domain with four binding sites, each

one composed by three histidines and one cysteine side chain in a square-planar coordination geometry, shown in Figure 1.3 (Schreiter *et al*, 2003).

Although *E. coli* NikR demonstrated to bind nickel at a very high affinity degree with a relevant allosteric effect, other divalent transition metal ions such as Co(II), Cu(II), Zn(II) and Cd(II) bind tightly to NikR, in accordance to the Irving-Williams series (Bloom and Zamble, 2004, Wang *et al*, 2004). In *E. coli* NikR, DNA binding to the *nik* promoter was suggested to occur through two metal-binding sites with a certain nickel affinity, however NikR-operator DNA complex structure demonstrated that it is through the two ribbon-helix-helix sites (Schereiter *et al*, 2006).

NikR from the human pathogen *Helicobacter pylori* represents a different nickel homeostatic model. Sequence analysis for *H. pylori* NikR revealed that it is not only homologous to *E. coli* NikR but with both similar DNA and nickel-binding domains (Contreras *et al*, 2003; Dosanjh and Michel, 2006). *H. pylori* NikR is a 'master regulator' nickel regulator, due to the ability to not only autoregulate its own *nikR* gene, but also represses operons involved in ferric iron uptake and urease production/activity under high nickel concentrations (Contreras *et al*, 2003; Dosanjh and Michel, 2006).

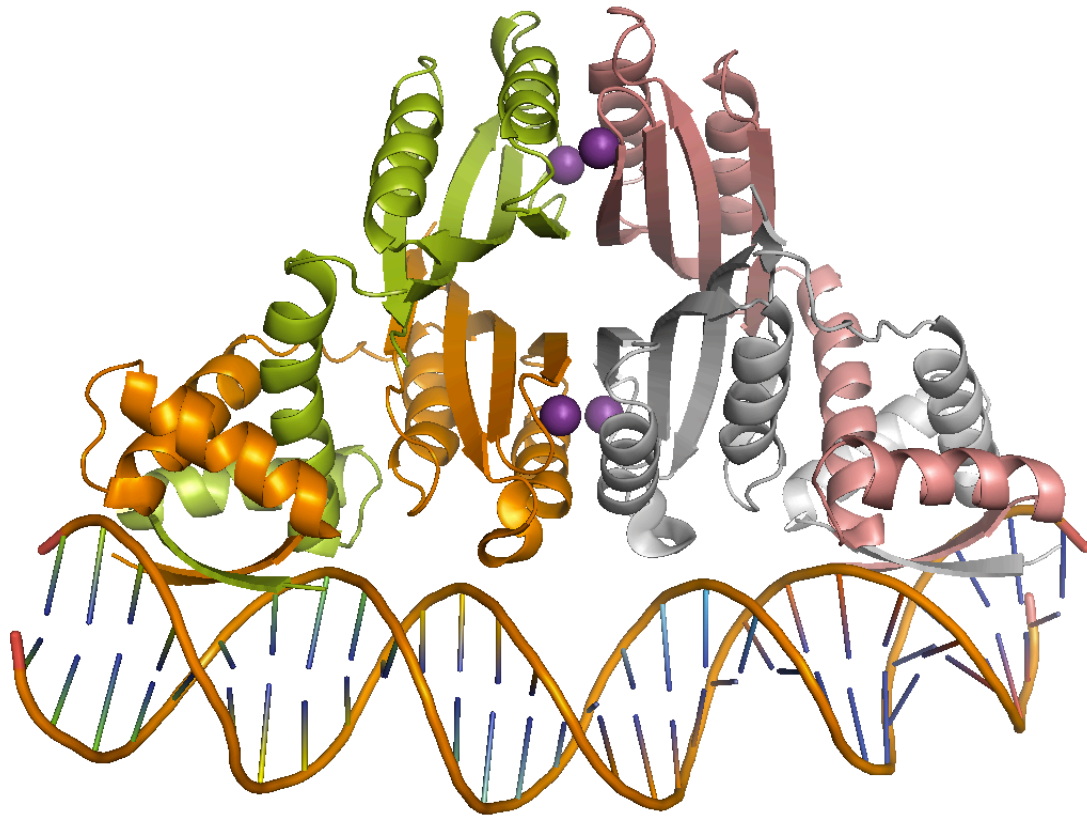


Figure 1.3 – The ribbon-helix-helix structure of *E.coli* NikR-DNA complex (Schreiter *et al*, 2006, PDB accession number: 2HZV). A dimeric N-terminal DNA binding domain is present, which is attached together through a tetrameric C-terminal Ni(II) (purple) regulatory domain. Image generated with MacPyMOL.

1.3.3.6. MerR

The MerR metalloregulator family is named after the cytoplasmatic MerR mercury-resistance (*mer*) gene that encodes a Hg(II) transcriptional regulator first found on the transposable elements Tn501 in *Pseudomonas aeruginosa* (Lund *et al*, 1986; O'Halloran and Walsh, 1987, Brown *et al*, 2003) and Tn21 in *Shigella flexneri* R100 plasmid (Foster and Ginnity, 1985).

All MerR regulators share similarity for the first one hundred amino acids and their dimeric structures feature a winged helix DNA binding region near the N-terminal and a metal binding C-terminal (Stoyanov *et al*, 2001, Brown *et al*, 2003). Small-angle X-ray scattering (SAXS) combined with molecular dynamics studies for both apo and Hg(II) bound MerR structures demonstrated Hg(II) to trigger a conformational change when it binds to MerR, from a metal/DNA-free compact shape to an extended one (Guo *et al*, 2010). Nanomolar concentrations of mercuric ion are sufficiently enough to trigger a transcriptional response by MerR, which activates transcription based on an allosteric effect that causes a DNA distortion at the promoter region; however, apo-MerR also binds to its target promoter sequence and represses its own transcription (Frantz and O'Halloran, 1990; Hobman, 2007; Guo *et al*, 2010).

1.3.3.7. CopY

CueR (**Cu** efflux regulator) is a cytoplasmatic MerR-like transcriptional activator involved in copper homeostasis in *Escherichia coli* by regulating the copper efflux ATPase CopA based on cytoplasmatic copper concentrations (Otten *et al*, 2000; Stoyanov *et al*, 2001). CueR has two binding regions, one for DNA with a winged helix motif at N-terminal and one for metal located at its C-terminal linked together through a dimerization helix (Figures 1.4 and 1.5), as also found in other MerR family members (Otten *et al*, 2000; Changela *et al*, 2003). The metal-binding region of *E. coli* CueR responds not only for copper with a zeptomolar sensitivity for free Cu(I) ions, but also silver and gold ions (Stoyanov *et al*, 2001, Changela *et al*, 2003).

In *Bacillus subtilis*, CueR regulates directly *in vitro* a copper-induced *copZA* operon system encoding CopZ (a Cu(I) chaperone) and CopA (CP_x-type ATPase), which are involved in a copper efflux system. The regulation occurs when CueR binds to *copZA* promoter *in vitro* and induces it *in vivo* (Gaballa *et al*, 2003).

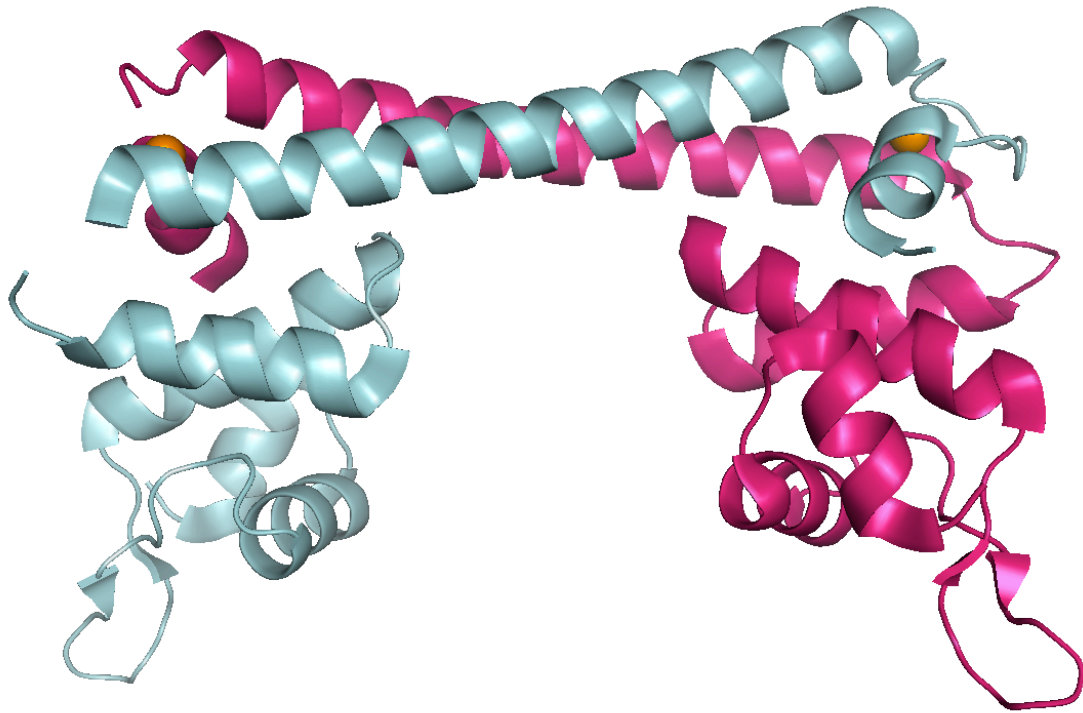


Figure 1.4 – *E.coli* Cu(I)-CueR and its winged helix (helix-turn-helix DNA binding domain (Changela *et al*, 2003, PDB accession number: 1Q05). Image generated with MacPyMOL.

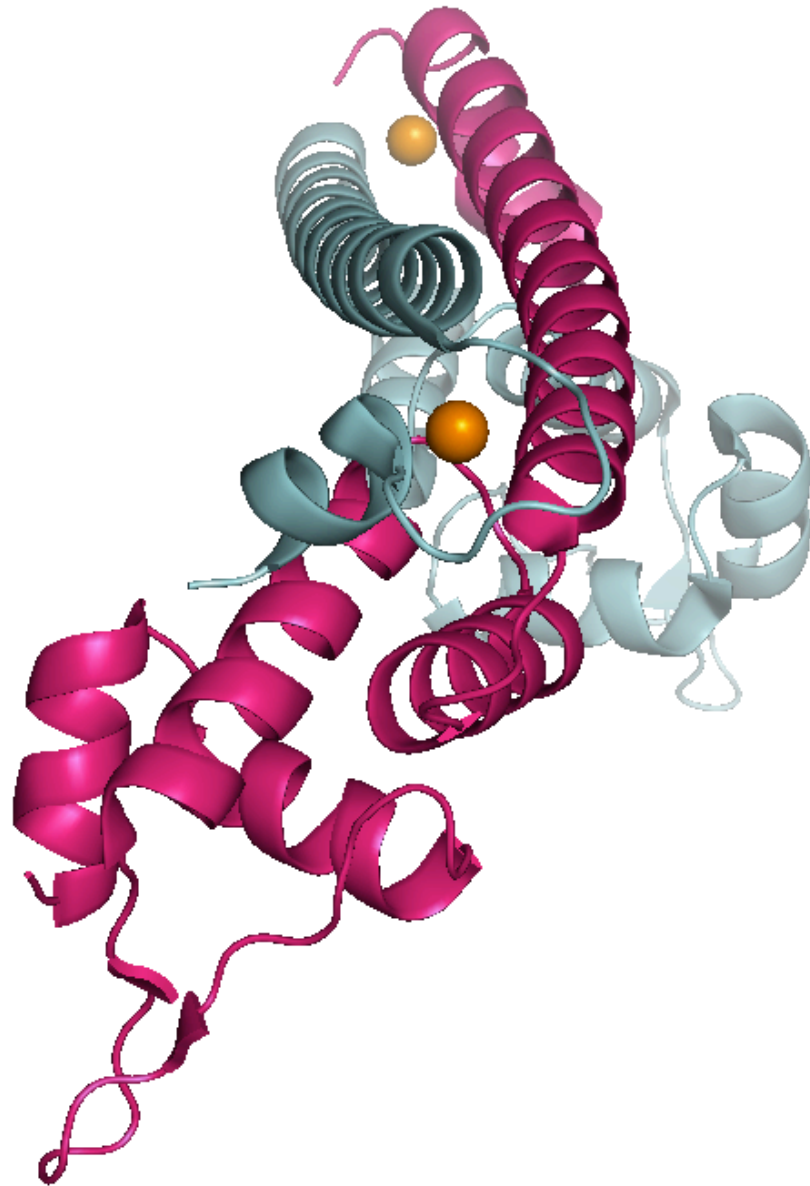


Figure 1.5 - The structure of *E.coli* Cu(I)-CueR on the side, with Cu(I) in orange and the interaction between the two dimers can be observed (Changela *et al*, 2003, PDB accession number: 1Q05). Image generated with MacPyMOL.

1.3.3.8 CsoR/RcnR

M. tuberculosis CsoR (**C**opper-**s**ensitive **o**peron **R**epressor) and *E. coli* RcnR are the founding members of a large, novel and poorly understood metalloregulator family, which is widely present in eubacterial genomes (Liu *et al*, 2007; Iwig *et al*, 2008). *M. tuberculosis* CsoR is a Cu(I) sensor which de-represses the *cso* operon which features the *csoR* gene itself and *ctpV*, a gene that encodes a P₁-type ATPase involved in copper transport (Liu *et al*, 2007). The crystal structure of *M. tuberculosis* Cu(I)-CsoR features a novel and non-canonical DNA-binding domain, described as an homodimeric antiparallel α -helix bundle (Liu *et al*, 2007; Chang *et al*, 2014). *E. coli* RcnR is a Ni(II)/Co(II) metalloregulator which de-represses its own *rcnR* gene and *rcnA*, which encodes RcnA, a Ni(II)/Co(II) efflux protein involved in metal homeostasis (Iwig *et al*, 2006; Iwig *et al*, 2008). *S. aureus* CstR [**C**soR-like **s**ulfur**t**ransferase **r**epressor] is a paralogous of CsoR of the very same species that senses persulfide and regulates the *cst* operon, a putative sulfide oxidation system (Grossoehme *et al*, 2011; Luebke *et al*, 2014).

An important characteristic of the CsoR/RcnR family lies in its signature W-X-Y-Z fingerprint motif that forms the first coordination shell, constituted by conserved ligands that coordinate the sensed metal(s). For CsoR-like proteins, the W-X-Y-Z fingerprint is represented by X-Cys-His-Cys motif (X-C-H-C, on which x can be any residue) and RcnR is His-Cys-His-His (H-C-H-H) (Liu *et al*, 2007; Higgins and Giedroc, 2014; Foster *et al*, 2014b). A cladogram of the CsoR/RcnR family suggested an extension of the fingerprint beyond the first coordination shell residues, a secondary one denominated A-B-(C) is also present, which may have an aiding role in metal ion coordination (Foster *et al*,

2014b). A recent phylogenetic study with 14 CsoR/RcnR proteins suggested how metal sensing has evolved between different metalloregulators within the family. Based on their evolutionary ancestors and individual W-X-Y-Z metal binding fingerprint, CsoR/RcnR members have been organised in seven major clades based on a common ancestor (I, II, III, IV, V, VI and VII) and are presented on Table 1.1 (Chang *et al*, 2014).

Table 1.1 – CsoR/RcnR clades I to III, organised by phylogenetic origin (adapted from Chang *et al*, 2014). The following residues are represented below: L, C, H, T, S, and G (Leu, Cys, His, Thr, Ser and Gly, respectively).

Clade	Examples	Species	Metal(s) ion or molecule sensed	W-X-Y-Z Fingerprint motif residues
Ia	CsoR	<i>Mycobacterium tuberculosis</i>	Cu(I)	LCHC
Ib	CsoR	<i>Thermus thermophilus</i>	Cu(I), Ni(II), Zn(II), Ag(I) and Cd(II)	LCHH
Ic	NcrB	<i>Leptospirillum ferriphilum</i>	Ni(II)/Co(II)	TCHC
IIa	RcnR	<i>Escherichia coli</i>	Ni(II)/Co(II)	HCHH
IIb	FrmR	<i>Escherichia coli</i>	-	SCHT
IIIa	cgR_0458	<i>Corynebacterium glutamicum</i>	-	GCHC
IIIb	CsoR	<i>Streptomyces lividans</i>	Cu(I)	GCHC
IIIc	RicR	<i>Mycobacterium tuberculosis</i>	Cu(I)	GCHC

Table 1.1 - (Continued) CsoR/RcnR clades IV to VII, organised by phylogenetic origin (adapted from Chang *et al*, 2014). The following residues are represented below: C, H, K and R (Cys, His, Lys and Arg, respectively).

Clade	Examples	Species	Metal(s) ion or molecule sensed	W-X-Y-Z Fingerprint motif residues
IVa	CsoR	<i>Bacillus subtilis</i>	Cu(I)	KCHC
IVb	CsoR	<i>Geobacillus thermodenitrificans</i>	Cu(I)	RCHC
IVc	Lmo1854	<i>Listeria monocytogenes</i>	-	RCHC
V	CstR	<i>Staphylococcus aureus</i>	persulfide	CNC
VI	CsoR	<i>Staphylococcus aureus</i>	Cu(I)	HCHC
VII	InrS	<i>Synechocystis PCC 6803</i>	Ni(II)	HCHC

M. tuberculosis also has another CsoR-like Cu(I) sensor, clade III RicR, which is involved in dealing with copper toxicity pathways and may be linked to its virulence factor (Festa *et al*, 2011; Shi *et al*, 2014). The CsoRs from *B. subtilis*, (clade IV), *S. aureus* (clade V) and *L. monocytogenes*, regulate a copper resistance *copZA* operon, where CopZ is a Cu(I) chaperone and CopA a P₁-type ATPase (Smaldone and Helmann, 2007; Baker *et al*, 2011; Corbett *et al*, 2011, Grosseohme *et al*, 2011).

The clade I *Thermus thermophilus* CsoR (Figures 1.6 and 1.7) was shown to bind not only copper ions, but also Zn(II), Ag(I), Cd(II) and Ni(II) leading to a transcriptional repressive response of the *copZRA* operon, which also encodes CopZ and Cop A (Sakamoto *et al*, 2010). Another CsoR/RcnR-like sensor of interest is the clade VII *Synechocystis* PCC 6803 IrnS, on which upon Ni(II) binding represses the *nrsD* gene both under *in vitro* and *in vivo conditions*, which also binds to Zn(II) *in vitro* (Foster *et al*, 2012; Foster *et al*, 2014b). Recent reported studies have been on the structural and allosteric studies of another Cu(I) sensor, clade IV *Geobacillus thermodenitrificans* CsoR in its Cu(I)-bound structure (Chang *et al*, 2014; Chang *et al*, 2015)(Figures 1.8 and 1.9).

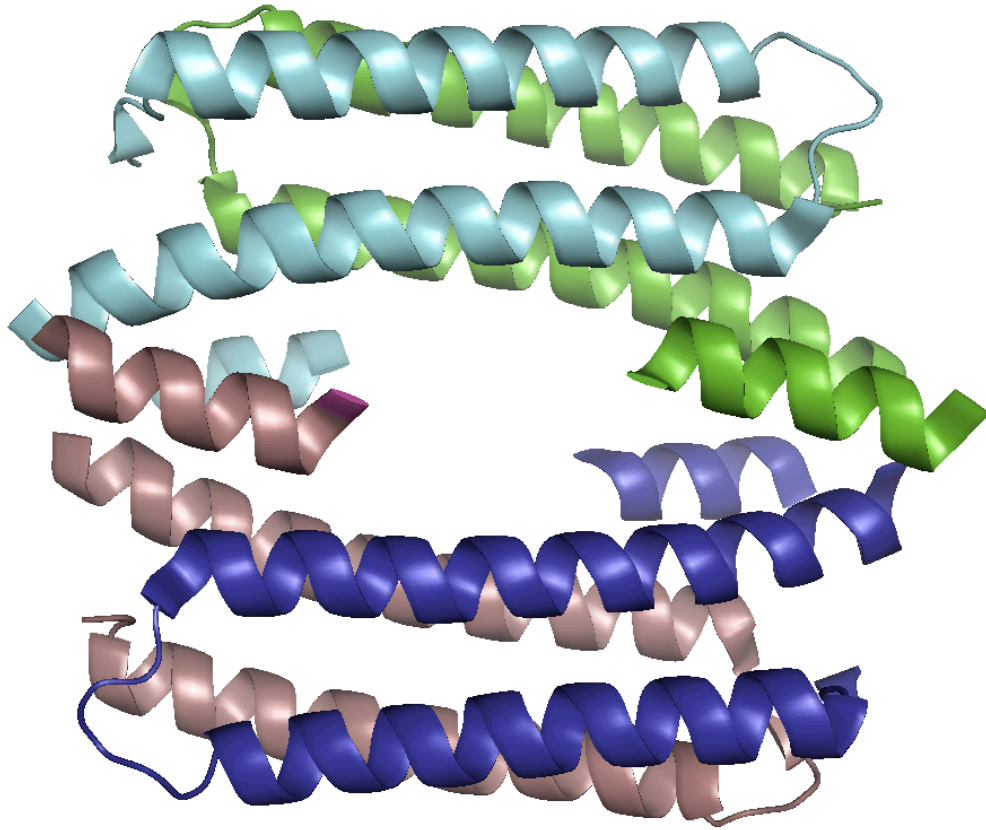


Figure 1.6 - The apo structure of *Thermus thermophilus* CsoR tetramer and its individual monomers, forming an antiparallel α -helix bundle (Sakamoto *et al*, 2010; PDB accession number: 3AAI). Image generated with MacPyMOL.

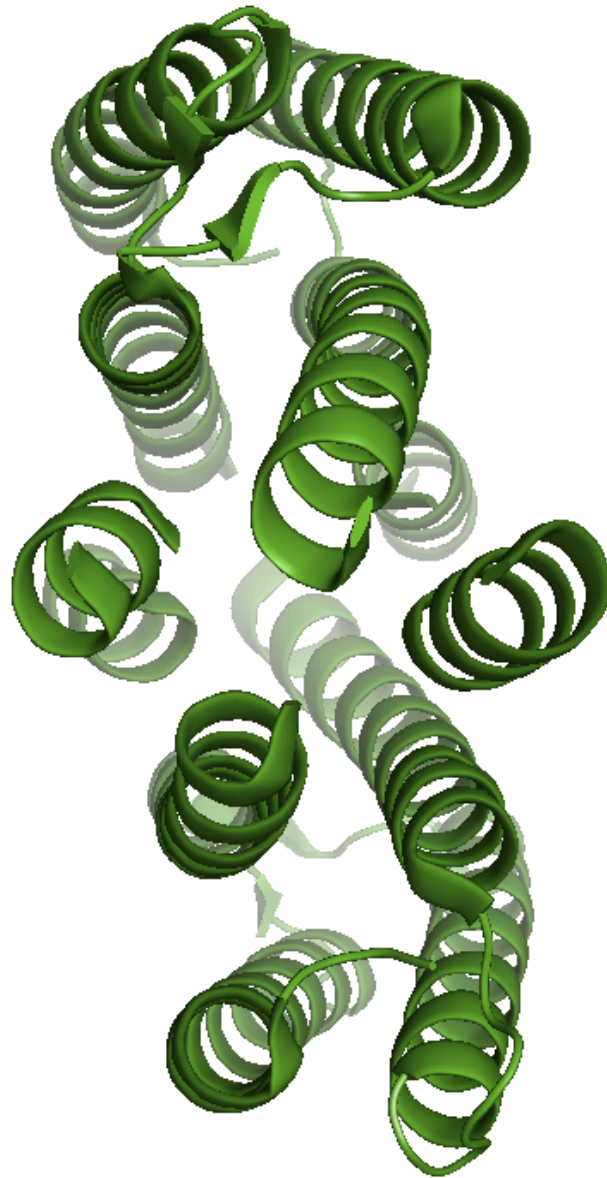


Figure 1.7 - The apo structure of *Thermus thermophilus* CsoR formed by an antiparallel α -helix bundle, side view (Sakamoto *et al*, 2010; PDB accession number: 3AAI). Image generated with MacPyMOL.

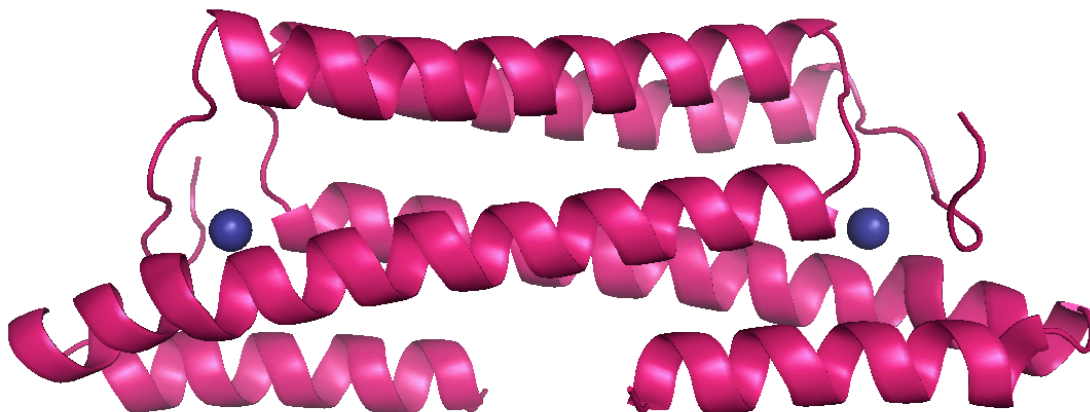


Figure 1.8 - The holo structure of *Geobacillus thermodenitrificans* Cu(I)-CsoR represented as a dimer. The N-terminal region lies down the Cu(I) (in violet) binding site located at the $\alpha 2$ helix (Chang *et al*, 2014; PDB accession number: 4M1P). Image generated with MacPyMOL.

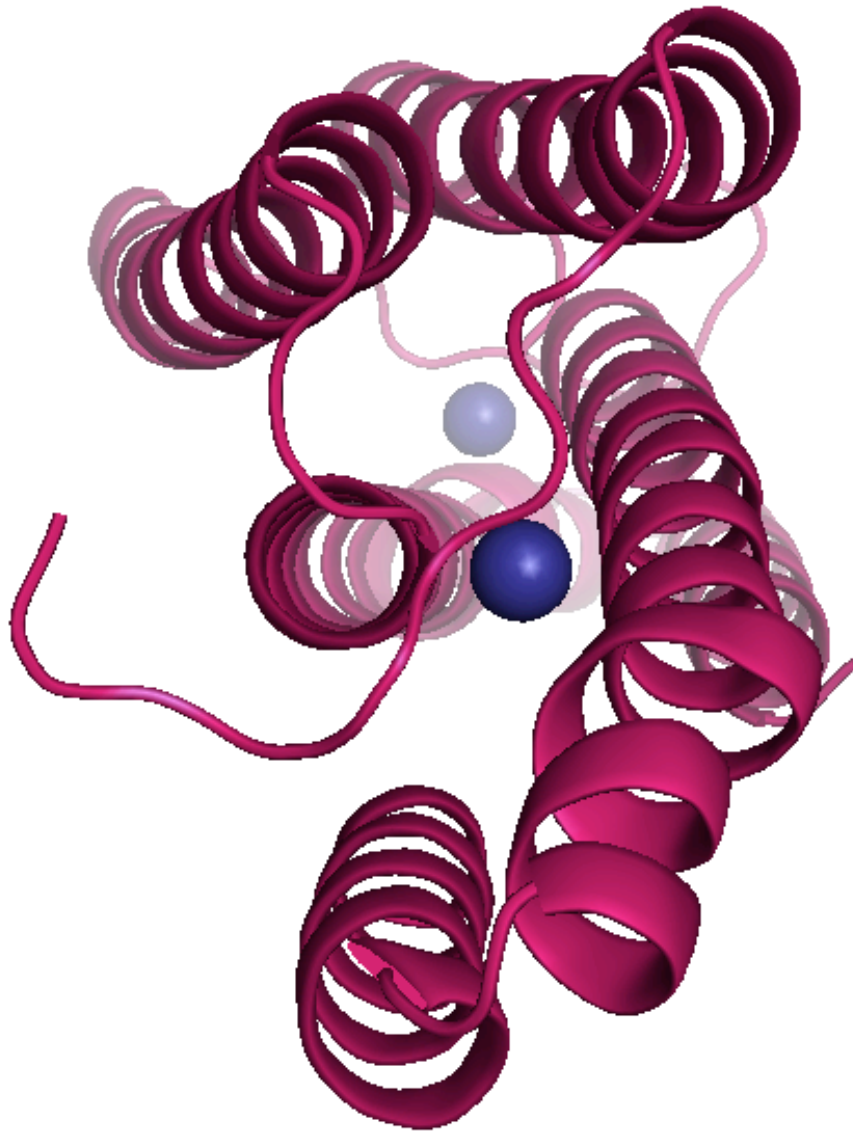


Figure 1.9 - The holo structure of *Geobacillus thermodenitrificans* Cu(I)-CsoR represented as a dimer, side view. The N-terminal region lies down the Cu(I) (in violet) binding site located at the α 2 helix (Chang *et al*, 2014; PDB accession number: 4M1P). Image generated with MacPyMOL.

1.4 Current knowledge on *S. lividans* CsoR

1.4.1 Introduction

In *Streptomyces*, copper has been shown to be crucial on the morphological switch phase between vegetative growth and aerial hyphae previously mentioned in section 1.3. Considering the biochemical dilemma between copper metabolism and toxicity, at least one copper sensor must be present within the copper proteome in *Streptomyces* species. In the early 2010s, a novel Cu(I) sensor was first identified and characterised in *S. lividans* 66 (previously reported as 1326) (Dwarakanath et al, 2012; Cruz-Morales et al, 2013). Sequence alignment studies revealed the gene *SLI4375* that encodes this new copper sensor to be a member of the CsoR/RcnR metalloregulator family, due to the conservation of residues which may be involved in Cu(I) and also DNA binding, so therefore it was then assigned as CsoR (Dwarakanath et al, 2012; Cruz-Morales et al, 2013).

1.4.2 CsoR, the *csoR* regulon and the chaperoning properties of CopZs

The *csoR* regulon is constituted by three genes, the first being *csoR* which encodes CsoR itself, followed downstream by a *copZA* operon (*copZ* and *copA* genes respectively). The *copZA* operon is suggested to be part of a CopZ/CopA Cu(I) efflux system (Cruz-Morales *et al*, 2013; Dwarakanath *et al*, 2012, Chaplin *et al*, 2015). CopZ is responsible for delivering Cu(I) as a chaperone to a CopA ATPase as well as delivering Cu(I) to DNA-bound CsoR in its apo state under Cu(I) induction/stress conditions *in vitro* the latter is reminiscent of *E. hirae* CopZ trafficking Cu(I) to the CopY (Chaplin *et al*, 2015). Based on *S. lividans* 66 genome sequence (Cruz-Morales *et al*, 2013) and re-analysis of previously RNA-sequence reported data (Dwarakanath *et al*, 2012), *copZ/copA* pairs 1063-1064 and 3079-3980 have a major importance in copper resistance due to their high expression levels (Chaplin *et al*, 2015). Another *copZ/copA* pair of interest is 1317-1318, which despite its low expression rate, has a strong repression effect due to the presence of two CsoR binding sites (Chaplin *et al*, 2015).

1.4.3. The interplay between CsoR and CopZs in copper homeostasis

Under Cu(I) homeostasis conditions, in which equal amounts of apo-CsoR and Cu(I)-CsoR are present in the cytosol, the *csoR* gene represses the expression of CopZ-1317 (Figure 1.10, left panel). Upon low Cu(I) concentrations, Cu(I) binds to CsoR, forming a Cu(I)-CsoR complex with subsequent dissociation from CopZ-1317 and also a second CopZ-like

chaperone, CopZ-3079. Therefore, the expression of both CopZ-1317 and CopZ-3079 are not repressed and more of these proteins are produced to cope with the increasing presence of intracellular Cu(I). A recent study (Chaplin *et al*, 2015) revealed that CopZ-3079 has a higher Cu(I) affinity in comparison to CopZ-1317 due to the acidic properties of the Cys residues from the Cu(I) binding Met-X₁-Cys-X₂-X₃-X (MX₁CX₂X₃X) motif. As a result, CopZ-3079 can optimise Cu(I) transfer and also has a buffer effect under Cu(I) stress conditions. Electrophoretic mobility assays (EMSA) studies revealed Cu(I) transfer to be unidirectional from both CopZ-1317 and CopZ-3079 to CsoR rather than from Cu(I)-CsoR to both CopZs .

1.4.4. Current copper homeostatic regulation model in *S. lividans*

Due to its higher Cu(I) affinity in comparison with CopZ-1317, CopZ-3079 may have Cu(I) buffering properties within copper homeostasis and basal metabolism. At Cu(I) induction/stress levels, initially CopZ-3079 is suggested to initialise Cu(I) transfer to DNA-bound CsoR, which leads to the dissociation of three *copZ/copA* Cu(I) efflux systems. In a second moment, CopZ-1317 starts assisting CopZ-3079 to transfer Cu(I) to CsoR while Cu(I) buffering by apo-CopZs is still on going in the cytoplasm. Cu(I)-CopZs also proceed to Cu(I) trafficking to their cognate CopA ATPases for Cu(I) removal from the cell. As a result of this interplay, partial derepression of the *csoR* operon occurs while for *copZ-1317* and *copZ-3079* is fully completed (Figure 1.10)

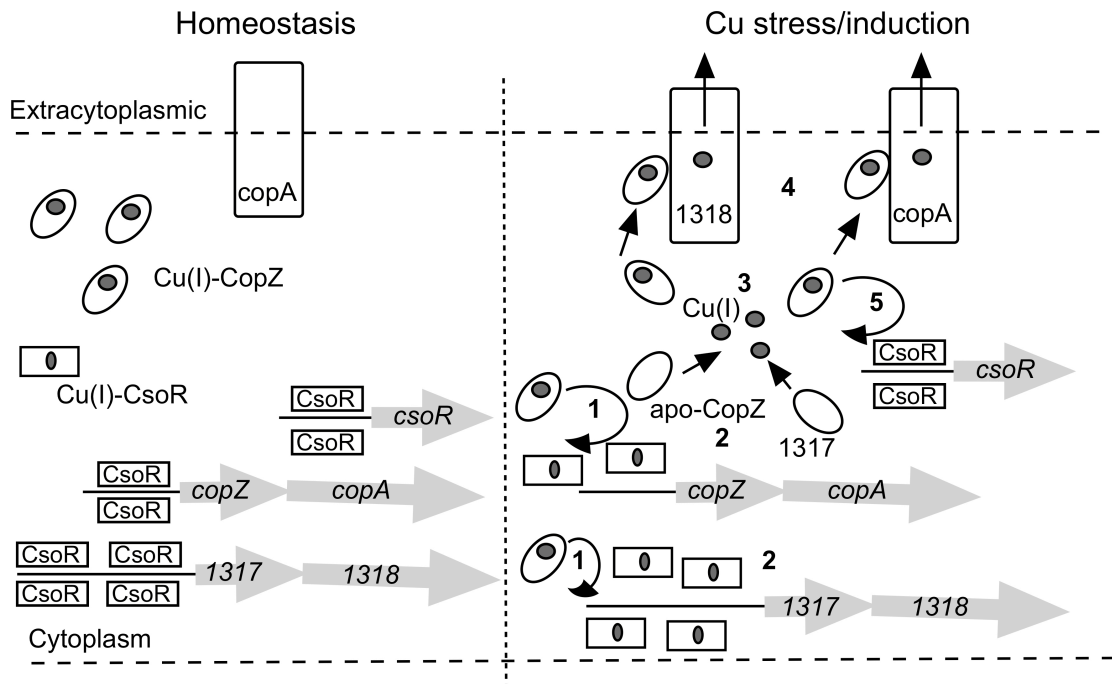


Figure 1.10 - The current Cu homeostasis model in *S. lividans*, represented by the CsoR regulon and its pathways (Chaplin et al, 2015). The following steps occur under Cu stress/induction: (1) CopZ 3079 initially transfers Cu(I) to CsoR (which is in its complexed form with DNA), causing repression of 3 copZ/copA Cu (I) efflux systems. (2) Resulting apo-CopZs are still buffering Cu(I). (3) CopZ 1317 eventually assists CopZ 3079 to buffer Cu(I) effectively. (4) Cu(I)-CopZs traffic their Cu(I) load to their cognate CopA transporters for Cu(I) export to outside the cytoplasm. (5) The *csoR* gene is partially derpressed due to different thermodynamic binding properties. Figure courtesy of Dr. Jonathan A. R. Worrall.

1.4.5. *S. lividans* CsoR structure and its putative Cu(I) binding residues

The 1.7-Å crystal structure of *S. lividans* apo-CsoR (Figure 1.11) revealed a homotetramer assembly, which would require a significant conformational change in order to allow Cu(I) binding (Dwarakanath *et al*, 2012). Through C α -secondary structure superposition with *M. tuberculosis* Cu(I)-CsoR structure at the Cu(I) binding site, the corresponding (and putative) Cu(I) binding residues in *S. lividans* CsoR are Cys75', His100 and Cys104 at the X-Y-Z positions of the fingerprint motif (Figure 1.12). Cys75 is positioned on a loop, which connects α -helix 1 to 2 in one monomer, while both His100 and Cys104 are located towards the end of α 2 helix of another monomer. A sulfate anion binds to His100 and His103; and Cu(I) is suggested to be accommodated at the sulphate position (Dwarakanath *et al*, 2012).

Initial investigation on the role of the putative Cu(I) binding residues in CsoR (Dwarakanath *et al*, 2012) started with the construction of mutants C75A and H100A, on which their Cu(I) binding properties were tested. Both mutations were shown not to disrupt the tetrameric assembly of CsoR as observed in size-exclusion chromatography. Anaerobic static titrations monitored by UV-Vis spectroscopy with C75A and H100A mutants revealed the corresponding Cu(I) binding peak at 240 nm was still present. A band at 320 nm, which was previously observed at wild-type (WT) CsoR, was absent for the H100A mutant upon Cu(I) addition.

The DNA binding properties of C75A and H100A were investigated *in vitro* through EMSAs. Upon mixing with each one of the three DNA target sequences (*SLI_1317*, *SLI_3079* and the *csoR* gene itself) from the *csoR* regulon, both mutants were still able to form a complex with them. When Cu(I)

was added, it did not affect the presence of a low mobility band related to the mutant-DNA complex nor a considerable increase of the high mobility, free DNA band (Dwarakanath *et al*, 2012).

At a structural level, the comparison with *M. tuberculosis* Cu(I)-CsoR structure has left a few unanswered questions on a possible mechanism of allosteric regulation of CsoR. Alongside Cys75' and His100, Cys104 is suggested to be a Cu(I) binding residue as mentioned before and through superposition (Figure 1.13). It is suggested that this residue must undergo a sufficient movement to coordinate Cu(I) properly; the sulfate ion observed on CsoR occupies a place on which Cu(I) was found in *M. tuberculosis* Cu(I)-CsoR. His103, a residue near His100 and an adjacent residue to Cys104, may have an involvement on Cu(I) binding to CsoR due to its location and its imidazole ring, which may be involved in metal ion coordination. Other CsoR/RcnR family members have histidines as part of their W-X-Y-Z metal binding fingerprint as shown on Table 1.1 previously in section 1.3.3.8 and they may be involved in binding other metals besides Cu(I) as in other family members.

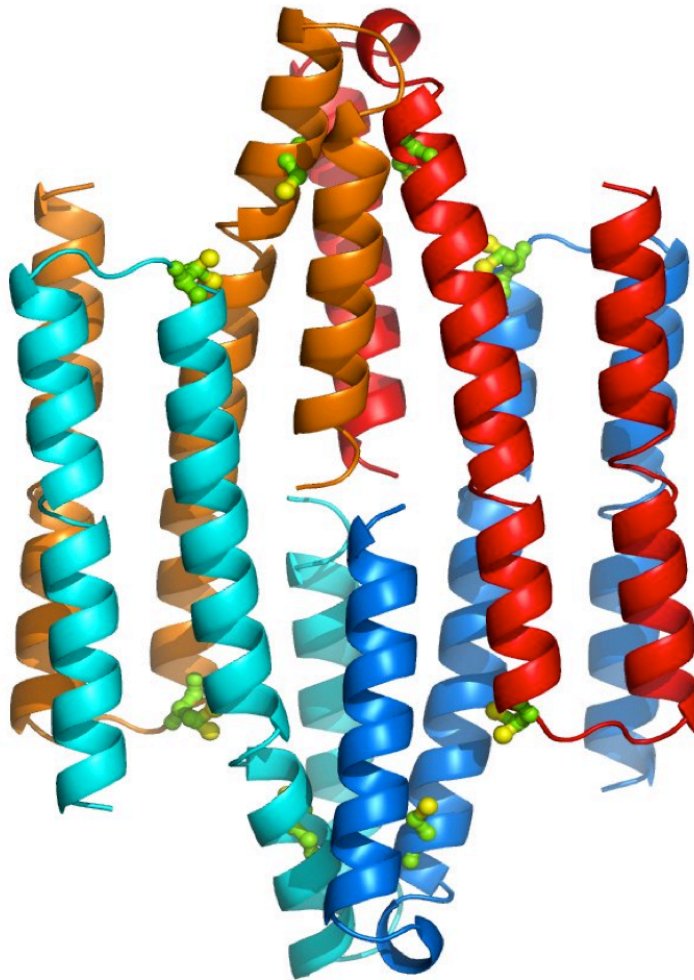


**Figure 1.11 – *S. lividans* CsoR apo structure at pH 4, formed by four α -helical monomers, represented in different colours. The putative Cu(I) binding region (green and yellow blobs) are also displayed on the structure (Dwarakanath et al, 2012; PDB accession number: 4ADZ).
Figure courtesy of Dr. Jonathan A. R. Worrall.**

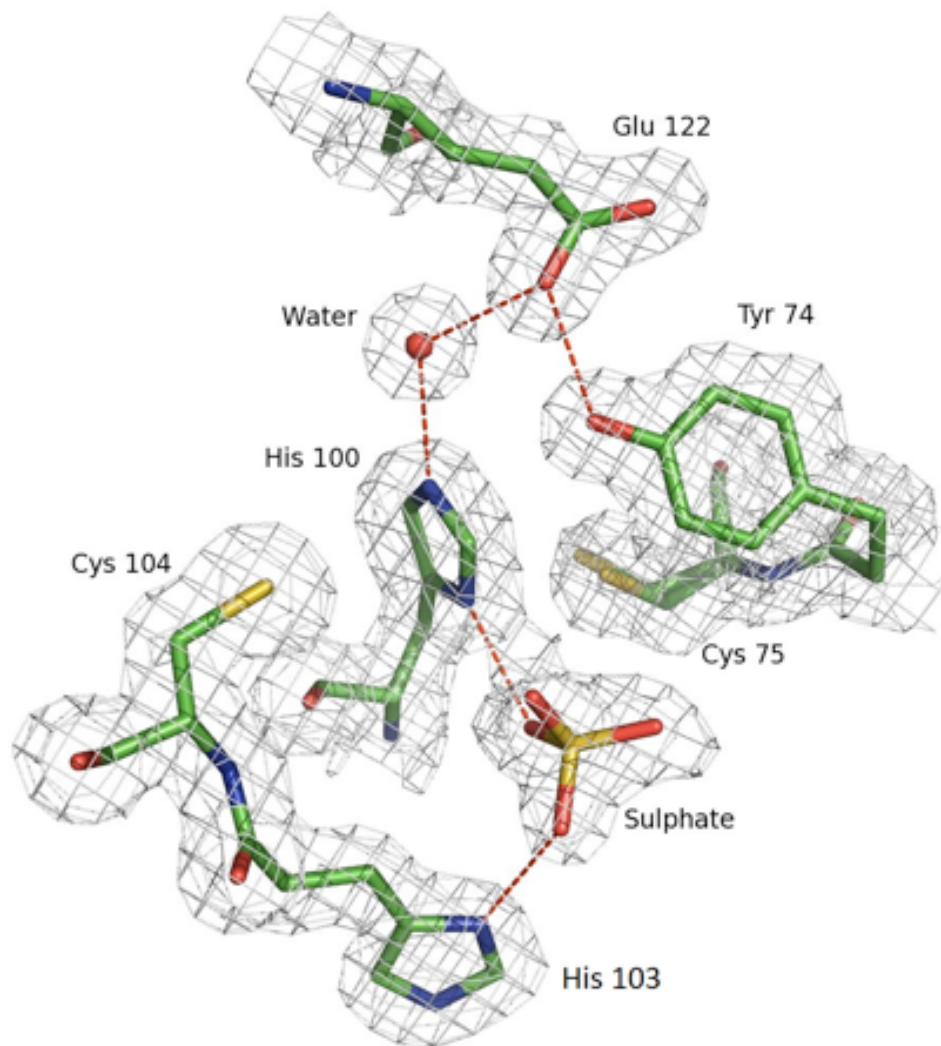


Figure 1.12 - The putative Cu(I) binding residues in *S. lividans* CsoR (Cys 75', His 100 and Cys 104) and vicinities (Tyr74, His103 and Glu122). Figure courtesy of Dr. Jonathan A. R. Worrall.

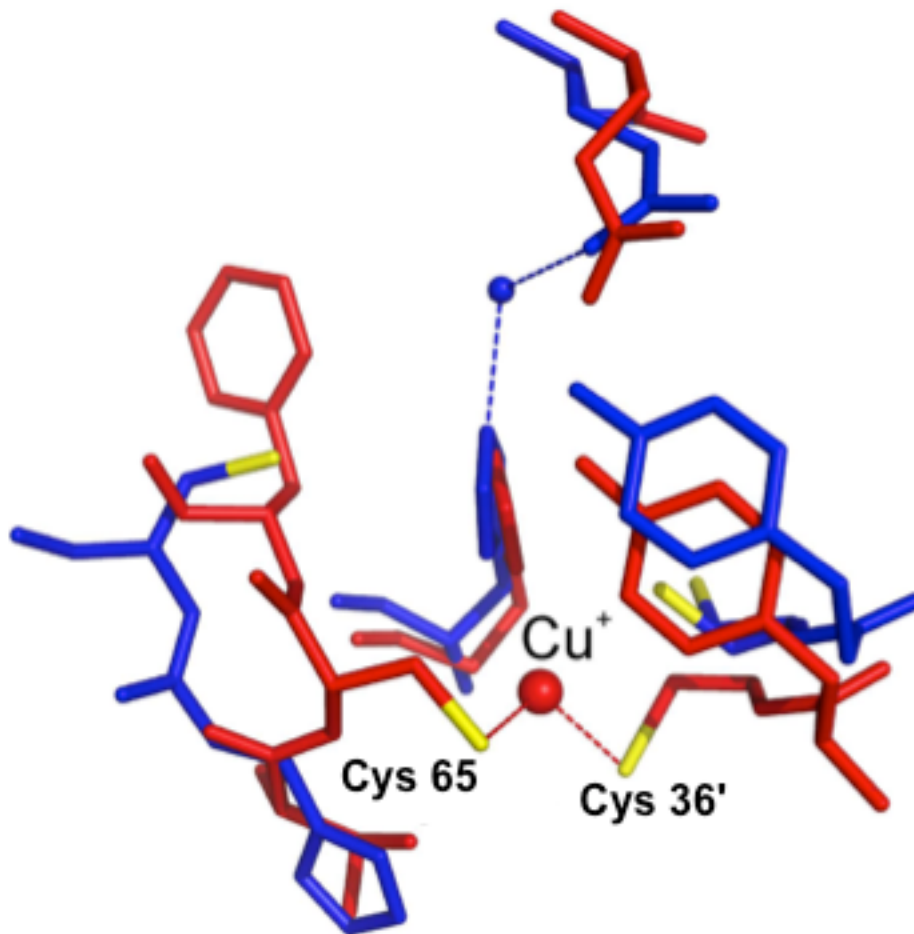


Figure 1.13 - C α superposition of the Cu(I) binding site of *M. tuberculosis* Cu(I)-CsoR (red) with *S. lividans* CsoR (blue). Cu(I) in *M. tuberculosis* CsoR is coordinated by Cys36' and Cys65. Figure courtesy of Dr. Jonathan A. R. Worrall.

1.4.6. Insights on DNA binding to CsoR

Despite the absence of a CsoR-DNA complex X-ray structure, a few insights on how CsoR binds to its DNA operator have been explored. A 2 CsoR : 1 DNA operator stoichiometric ratio have been constantly suggested across different CsoR/RcnR family members (Liu *et al*, 2007; Ma *et al*, 2009a; Grossoehme *et al*, 2011; Dwarakanath *et al*, 2012). CsoR operator sites feature 2-short G/C-tracts with 2-4 intervening bases and the AT-rich inverted repeat outside these tracts.

The homotetrameric structure of *S. lividans* CsoR features a diagonal electropositive surface area that spans across the antiparallel dimers (Dwarakanath *et al*, 2012; Tan *et al*, 2014). Bioinformatical studies suggest the electropositive residues Arg54, Arg57, Arg129 and Arg132, together with the polar residue Gln81 to be involved in DNA binding. Localised in the α 1 helix, Arg54 and Arg57 are part of a highly conserved RLXR motif across CsoR proteins. The α 1-helix Arg-Leu-X-Arg (RLXR, X is any residue) motif involves the ends of the electropositive tract that runs across each CsoR tetrameric face in a diagonal manner. Gln81 is localised nearby at the α 2 helix and acts as a link between α 1 and α 2 helices. Both Arg129 and Arg132 are localised at the α 3 helix and are suggested to modulate DNA binding to CsoR (Tan *et al*, 2014).

Thermodynamic studies with alanine mutants of these predicted DNA binding residues revealed that each Arg residue individually has a considerable impact on reducing CsoR binding affinity to DNA, especially the α 1 helix ones. With an alanine mutation at Arg129 located at α 3 helix, the

CsoR: DNA stoichiometric ratio was changed. Gln81 had an important contribution on establishing polar contacts required for strong DNA binding.

A proposed model for DNA binding to CsoR has been suggested in Figure 1.14 (Tan *et al*, 2014). The A and B forms of the *csoR* gene were both represented, with their major and minor grooves (large and small arrows) and GTA dyads (yellow). GTA dyads are a conserved 5'-TAC/GTA-3' inverted repeat sequence present at the DNA operator sequence itself (Figure 1.14A). Binding occurs via a 2-fold axis of symmetry with two CsoR tetramers to one DNA, on which both major and minor grooves interact (Figure 1.14B). In Figure 1.14C, the proposed points on which CsoR interacts with DNA in terms of α -helices and residues are presented with Arg residues located on α 1 (Arg54 and Arg57) and α 3 (Arg129 and Arg132) in purple, plus Gln81 at α 2 (orange). Figure 1.14D is a cartoon representation of the mechanism of CsoR binding to its operator site, focusing on the B-DNA configuration change to pure A-DNA between the GTA dyads (yellow)/ α -helices contact regions formed by two CsoR tetramers. The impact of Cu(I) binding on the CsoR-DNA complex flexibility is represented on a transverse view, with white dots representing no Cu(I). Upon binding to DNA, CsoR may adopt a 'relaxed' conformation that allows flexibility towards one of its DNA binding faces to bind to DNA. This conformational change may affect tetramer symmetry and also the predicted Cu(I) binding site region. As the predicted Cu(I) binding site is located near the α 1 helix, upon Cu(I) binding a loss of flexibility may occur, due to a restricted movement of the tetramer. This Cu(I) binding event may result in dissociation of DNA upon filling the four Cu(I) binding sites (blue) in CsoR (Figure 1.14E).

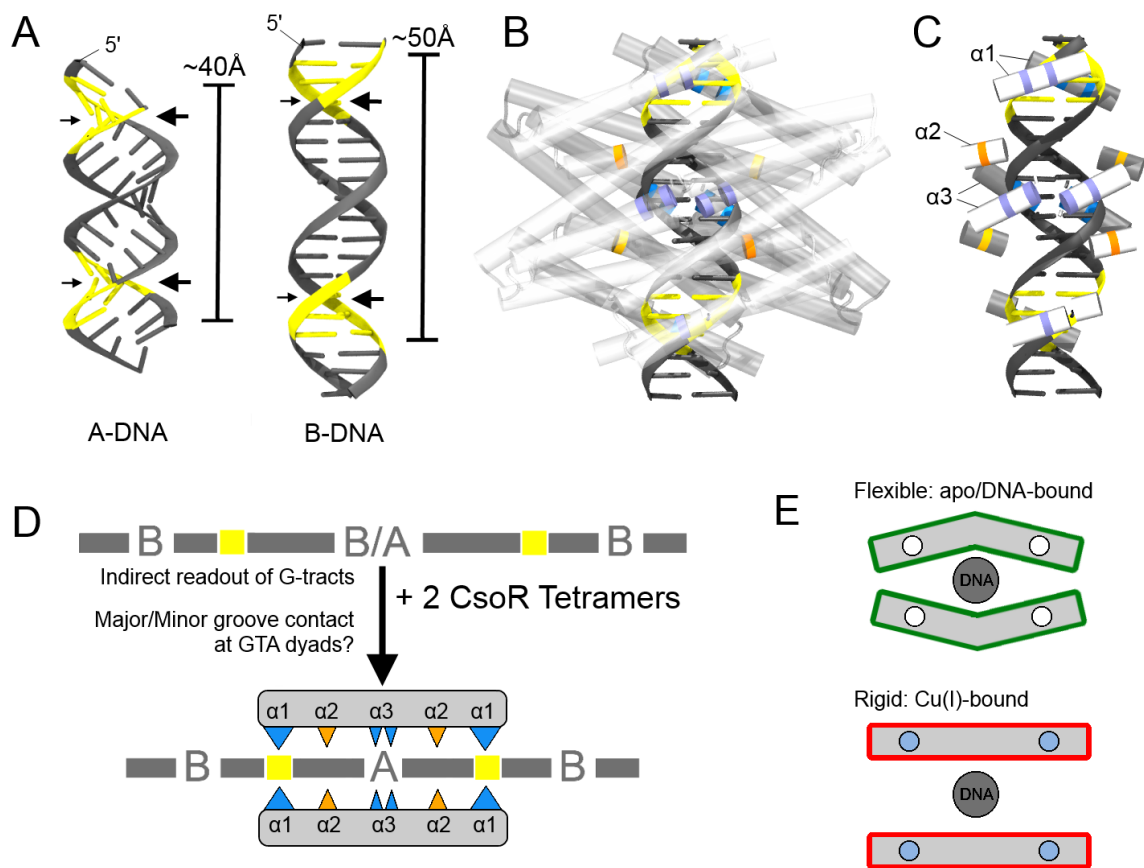


Figure 1.14 – The proposed CsoR/DNA binding model (Tan et al, 2014.)
(A) Operator site modeled in the A- and B-DNA forms. **(B)** and **(C)** represent the 2 CsoR : 1 DNA binding model and putative DNA bases, respectively. **(D)** The interaction between $\alpha 1$, $\alpha 2$ and $\alpha 3$ helices of CsoR with its DNA binding site. **(E)** The states of CsoR in its apo-DNA (top) and Cu(I)-bound form (bottom). Figure courtesy of Dr. Jonathan A. R. Worrall.

1.5 Aims of this PhD project

This PhD project was focused on the structural and kinetic studies of CsoR as a metalloregulator in *S. lividans*, in order to expand the current understanding on both metal selectivity and specificity of metalloregulators and its effects on metal-induced allostery within the CsoR/RcnR family.

The following questions were under investigation:

- How can structural changes within the *S. lividans* CsoR structure affect DNA binding and consequently provide insights on the Cu(I)-induced allosteric response?
- What does happen at structural level when one individual residue from the putative Cu(I) binding site is mutated? Are there considerable structural changes at either secondary or tertiary structure triggered by the mutation itself?
- How versatile is the predicted Cu(I) binding site of *S. lividans* CsoR in terms of metal selectivity in comparison to other CsoR/RcnR family members? If a different (i.e. non-cognate) metal from Cu(I) binds to CsoR in vitro, what is the mechanism of binding? What is the effect of Ni(II) binding to CsoR on the allosteric response in vitro?
- How does Cu(I) bind to *S. lividans* CsoR in terms of coordination chemistry and mechanism? And in the case of non-cognate metal binding, how does this binding mechanism occur?

In order to study both metal specificity and selectivity of the predicted Cu(I)-binding site in *S. lividans* CsoR, two new alanine mutants, H103A and

C104A, were constructed via site-directed mutagenesis to complete the full set of predicted Cu(I) binding residues, together with the previously reported C75A and H100A (Dwarakanath *et al*, 2012). Further heterologous over-expression in *E.coli* BL21 (DE3) cells and purification of these mutant fusion proteins using HisTrapTM Ni-NTA column/heparin/gel filtration were carried out. Structural biology studies of these CsoR mutants using circular dichroism and x-ray crystallography were conducted in order to observe the presence of relevant structural changes at the putative Cu(I)-binding site and how individual mutations can affect at secondary to tertiary structural level.

The metal selectivity properties of *S.lividans* CsoR were first investigated through titrations monitored by UV-Vis spectroscopy with Cu(I) for H103A and C104A and also for Ni(II) for both CsoR and mutants. For the very first time, the mechanism of metal binding of a CsoR/RcnR family member was investigated in detail using stopped-flow spectroscopy with Cu(I) and Ni(II). Furthermore, the displacement of Ni(II) from CsoR by Cu(I) was monitored and examined also through stopped-flow spectroscopy. The allosteric response of CsoR and mutants in the presence of Ni(II) and the *csoR* operon DNA target sequences together was also investigated in vitro via electrophoretic mobility shift assays (EMSA).

Chapter 2

Conformational Switching in CsoR visualised by X-ray Crystallography

2.1 Introduction

As previously introduced in section 1.4.6, on binding Cu(I) CsoR undergoes an allosteric conformational switching that drives negative regulation of DNA binding, i.e., dissociation from its DNA operator site. Apo-CsoR binds to its operator DNA in a 2:1 stoichiometry (Liu *et al*, 2007; Tan *et al*, 2014). A recent study presented a plausible model derived from experimental inputs as to how the tetrameric face of each apo-CsoR may 'sandwich' its DNA operator (Tan *et al*, 2014). A major challenge for research on CsoR/RcnR family members is to understand how Cu(I) drives this allosteric switching by disassembling or dissociating the 'sandwich' protein-DNA complex, which is still unclear (Chang *et al*, 2014).

Structures of CsoRs in apo-form from clade I *T. thermophilus* HB8 and clade III *S. lividans* or Cu(I)-bound form from clade I *M. tuberculosis* and clade IV *G. thermodenitrificans* have been determined via X-ray crystallography. All four structures revealed a protomer, consisting of three α -helices of varying lengths, arranged in a tetramer assembly (Liu *et al*, 2007; Sakamoto *et al*, 2010; Dwarakanath *et al.*, 2012; Chang *et al*, 2014). This α -helical disc-shaped structure is notable for the absence of a recognisable DNA binding domain. For the reported Cu(I)-bound structures, the presence of the Cu(I) ion does not have an overall impact on the α -helical character of these CsoRs (Liu *et al*, 2007; Chang *et al*, 2014). In comparison with apo-CsoR structures, Cu(I)-bound structures feature a helical discontinuity (described as a kink or bulge) located at the α 2 helix (Liu *et al*, 2007; Chang *et al*, 2014).

Recent small angle X-ray scattering (SAXS) studies using the clade IV *Geobacillus thermodenitrificans* CsoR have provided a molecular insight into the Cu(I) allosteric conformational switching associated with the regulation of DNA binding in CsoR (Chang *et al*, 2014). An important observation from these studies is a change in the hydrodynamic properties of the Cu(I)-bound form to a more compact state through scattering envelopes, with one dimer within the homotetramer proposed to reorient relative to the other (Chang *et al*, 2014). These global changes appear rather subtle but may be of significance for the destabilization or disassembly of the CsoR-DNA complex.

So far, current insights into the conformational switch between apo- and Cu(I)-bound states at the atomic level for CsoR/RcnR family have been inferred through comparison of the Cu(I)-bound form of one species to that of the apo-form of another species due to the absence of X-ray structures for both apo and Cu(I)-bound forms from the same species. In this chapter, a new X-ray apo structure of the clade III CsoR from *S. lividans* at a higher pH of 6 is reported. Through comparative analysis of this new CsoR structure at pH 6 with the previously reported CsoR apo structure at pH 4 (Dwarakanath *et al*, 2012), significant structural differences throughout the homotetramer assembly are apparent, which were based on NMR (Coyne & Giedroc, 2013) and SAXS (Chang *et al.*, 2014) observations of *G. thermodenitrificans* Cu(I)-CsoR structure. These observed structural changes are strongly consistent with features associated with a Cu(I)-bound form. Comparison of the structural transitions that occur between *S. lividans* CsoR pH 4 and pH 6 apo structures enables the allosteric conformational switch in a CsoR that drives repression of DNA binding to be visualised at an atomic level resolution.

Furthermore, comparison of the surface charge distribution between the apo- and 'quasi Cu(I)-bound' state reveals a striking variation, that supports dissociation of operator DNA via electrostatic occlusion (Chang *et al.*, 2015).

2.2. Materials and Methods

2.2.1 Crystallisation and data collection

Recombinant *S. lividans* CsoR was over-expressed in *E. coli* BL21 (DE3) cells and purified as previously described (Dwarakanath *et al.*, 2012). Protein was concentrated to 1 mM in a 500 μ l sample for crystallisation trials. Initial random crystal screening was carried out using a set of commercially available 96-well screen blocks mounted on a Gryphon robotic crystallisation suite (Art Robbins Instruments). A number of precipitant conditions were found to contain crystals, which differed to those previously used in determining the structure of apo-CsoR (Dwarakanath *et al.*, 2012). Most notable amongst the different conditions was the higher pH (> 5) compared to pH 4 previously used (Dwarakanath *et al.*, 2012). Crystals of apo CsoR were grown using the sitting drop vapour diffusion method at 20 °C. A suitable crystal hit was observed at this stage, in which the reservoir solution contained 0.01 M magnesium sulfate, 0.05 M sodium cacodylate pH 6.0, 1.8 M lithium sulfate. Manual optimization trials were conducted on 24-well plates, which were not successful. Single crystals from the 96-well robot tray suitable for x-ray diffraction were then transferred to a cryoprotectant solution containing the same reservoir solution and 20% glycerol prior to flash-cooling by plunging into liquid nitrogen. Crystallographic data were measured at

Diamond Light Source (beamline I03) using a Pilatus 6M-F detector and an X-ray wavelength of 0.9163 Å.

2.2.2. Structure determination and coordinates

Diffraction images were initially indexed, refined and then integrated with iMosflm (Battye *et al*, 2011). Integrated diffraction data was later merged using Scala (Evans, 2006) and Aimless on the CCP4i suite (Collaborative Computational Project, Number 4, 1994). Scala merges diffraction data into a high quality mtz file. *S. lividans* apo-CsoR at pH 4 structure (PDB accession number 4ADZ; Dwarakanath *et al*, 2012) was used as the search model for molecular replacement. The model was refined by maximum likelihood methods in Refmac5 (Murshudov *et al*, 2011) and rebuilt between refinement cycles in Coot (Emsley and Cowtan, 2004). Riding hydrogen atoms were added when refinement of the protein atoms had converged. The model was validated throughout using the Molprobity server (Davis *et al*, 2007) and the JCSG Quality Control Check server. Data and refinement statistics together with quality indicators are summarised in Table 2.1. Structure factors and coordinates have been deposited in the RCSB Protein Data Bank via the PDBe, with accession number 4UIG (published online on 09/09/15).

2.2.3 Structural movies

Movie files (S1 and S2, which are available at <http://scripts.iucr.org/cgi-bin/paper?S1399004715013012>, accessed on 20/10/2015) to reveal the extent of the structural changes between *S. lividans* CsoR at pH 4 (PDB accession

number: 4ADZ) and pH 6 (PDB accession number: 4UIG) overall as a homotetramer and at side level were generated using MacPyMOL.

2.3 Results and Discussion

2.3.1. An apo-CsoR structure displaying shape similarity to Cu(I)-CsoR

From crystals of *S. lividans* CsoR grown at pH 6 a tetragonal $I4_122$ space group symmetry was determined with a single protomer (one copy of the structure) found in the crystallographic asymmetric unit (Table 2.1). This is a contrast with crystals grown at pH 4, which have an orthorhombic $P2_122_1$ space group symmetry with two protomers located in the asymmetric unit (Dwarakanath *et al.*, 2012). The asymmetric unit is the smallest portion of a crystal structure at volume level on which symmetry operations (rotations, translations and a combination of both) can be applied to generate the crystal's repeating unit (unit cell). Different asymmetric units mean different structural organisation within the crystal structure.

Attempts to crystallise Cu(I)-bound CsoR from *S. lividans* using a wide range of crystal screens were conducted, but it yielded no crystals at all. In the pH 6 protomer structure a well-defined electron density was visible from residue number 42, up to the C-terminal residue 132 inclusive; no electron density was present for residues 1 to 41. By applying crystallographic symmetry a D_2 -symmetric homotetramer assembly that is prevalent in solution was generated, similar to apo-CsoR at pH 4 (Dwarakanath *et al.*, 2012). As previously described, each tetrameric face utilized to bind operator DNA is essentially dimeric, having two complete monomeric elements (*i.e.* $\alpha 1$ - $\alpha 2$ - $\alpha 3'$ helices) (Dwarakanath *et al.*, 2012). For CsoR members, the N-terminal

region is highly variable in sequence and length, with *S. lividans* CsoR having one of the longest N-terminal stretches before the start of the core protomer sequence. In the *G. thermodenitrificans* Cu(I)-CsoR structure electron density is visible for part of its N-terminal region, revealing it to be folded and lying over the Cu(I) binding site (Chang *et al.*, 2014). This folding of the tail is considered a factor in inhibiting the 2:1 CsoR:DNA assembly (Chang *et al.*, 2014; Chang *et al.*, 2015).

Molecular surfaces for the *S. lividans* CsoR X-ray structures at pH 4 (Dwarakanath *et al.*, 2012) and pH 6 were generated and are shown in Figure 2.1, with residues that are either known (Tan *et al.*, 2014) or suggested (*vide infra*) to interact with operator DNA indicated. These residues in question form a region on the tetrameric face with Gln 81 (green) as the boundary whereby the DNA is proposed to lie diagonally within this region in a northwest to southeast direction spanning between the $\alpha 1/\alpha 1'$ Arg54-X-X-Arg57 motif (X means any amino acid) (Chang *et al.*, 2011; Tan *et al.*, 2014) (Figure 2.1). It is apparent that significant shape differences exist between the two tetrameric structures of CsoR at different pH conditions (Figure 2.1).

The tetrameric face of pH 6 structure displays a clear constriction, as a direct result of the shortening of the axis running along the dimer-dimer interface, with a length decrease from 74 Å (pH 4) to 71 Å in the CsoR pH 6 structure (Figure 2.1). As a result, this constriction also leads to an overall 'swelling' of the homotetramer shape and a seemingly more rugged surface topology of the tetrameric face (bottom panel in Figure 2.1). The shape constriction is reminiscent of the differences observed in the calculated scattering envelopes derived from SAXS experiments between the apo- and

Cu(I)-bound states of the CsoR from *G. thermodenitrificans*, with the latter envelope clearly compacted relative to a more elongated apo-form (Chang *et al.*, 2014). In hydrodynamic terms, this observed difference was assigned solely to the presence of bound Cu(I) on the structure (Chang *et al.*, 2014). In fact, despite being from a different species and clade within the CsoR/RcnR family, the *S. lividans* CsoR pH 4 apo structure had a better superposition to the elongated scattering envelope calculated for the apo-structure of CsoR from *G. thermodenitrificans* CsoR than its X-ray Cu(I)-bound crystal structure (Chang *et al.*, 2014). The similarity of these calculated SAXS scattering profiles between two CsoRs from different species can be connected to the analysis of the phylogenetic tree for CsoR/RcnR proteins. Clades III and IV were branched at the same ancestor, one further away on the evolution tree than the ancestor which also originated clade I members (Chang *et al.*, 2014).

In the *S. lividans* CsoR pH 6 structure, the presence of an electron density consistent with a water molecule located between the putative Cu(I) ligands Cys75', His100 and Cys104 was observed (Figure 2.2). In the CsoR pH 4 structure, an electron density consistent with a sulfate ion was observed between His103 and His100 (Dwarakanath *et al.*, 2012). Thus the pH 6 homotetramer in the crystal is in an apo-state, but with a molecular shape bearing the hallmarks of a Cu(I)-bound CsoR in solution (Chang *et al.*, 2014).

Table 2.1 - Crystallographic data collection and processing statistics for apo *S. lividans* CsoR pH 6 structure. Values in parentheses refer to the outermost resolution shell (2.05-2.00 Å).

Wavelength (Å)	0.9163
Resolution (Å)	2.0
Space group	I4 ₁ 22
Unit cell (Å)	89.7, 89.7, 103.9
Unique reflections	14603
Completeness (%)	99.7 (99.8)
R _{merge} (%)	0.052 (0.728)
Mn(I/sd)	15.7 (2.3)
Redundancy	4.9 (4.5)
R _{cryst}	0.211
R _{free}	0.230
ESU based on ML (Å)	0.088
RMS dev. Bond lengths (Å)	0.015
RMS dev. Bond angles (°)	1.5
Ramachandran favoured (%)	98.9
Wilson B-factor (Å ²)	27.2
PDB accession code	4UIG

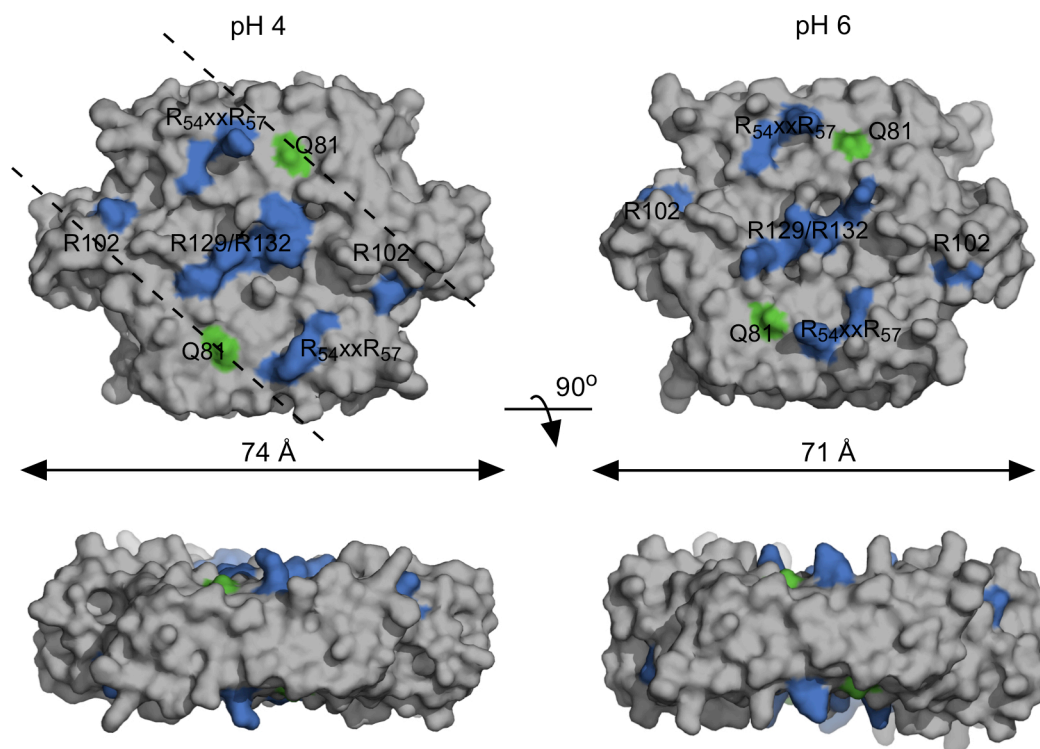


Figure 2.1 - Molecular surface representations of the homotetramer structure of *S. lividans* CsoR determined from crystals grown at pH 4 (left side, top and bottom, PDB accession number: 4ADZ) and (B) pH 6 (right side, top and bottom, PDB accession number: 4UIG). Residues known or predicted to interact with operator DNA are coloured in blue/green and properly labeled on the tetrameric surface. The dashed lines indicate the predicted boundary and direction of in that the operator DNA lies (Tan *et al*, 2014).

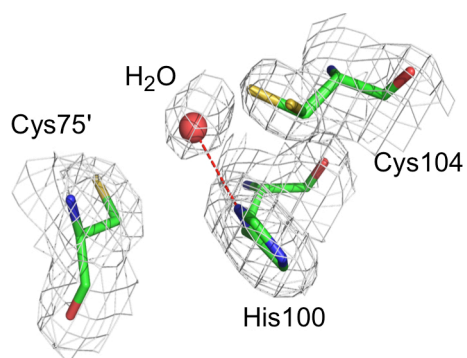


Figure 2.2 - The inter-protomer Cu(I)-binding site in the pH 6 crystal structure of apo *S. lividans* CsoR represented by an electron density map, which revealed the presence of a water molecule hydrogen bonded to His100. Cu(I) was absent.

2.3.2. Rearrangement of Cys104 side chain disrupts the α 2-helical geometry and alters the rotation of predicted DNA binding residues

A secondary-structure matching superposition of the pH 4 and pH 6 homotetramers reveals a number of features that are associated with the compaction of the pH 6 structure. In the pH 4 structure a continuous helical geometry of the α 2-helices in each protomer is present until residue 112 (Figure 2.3A). This geometry is clearly disrupted in the pH 6 homotetramer, where the distinctive presence of a 'bulge' or 'kink' in the helix beginning at His103 occurs (Figure 2.3A). Analysis of NMR chemical shifts have inferred a change in helix geometry between the Cu(I)-bound and apo-states of *G. thermodenitrificans* in the homologous region to *S. lividans* CsoR (Coyne and Giedroc, 2013).

Comparison between the *S. lividans* structures indicates that as a consequence of the bulge the side chain of His103 swings outwards and the Cu(I) ligand, Cys104, moves upwards into a spatial position that would now enable a metal ion to coordinate to Cys75', His100 and Cys104 (Figure 2.3A). This is not the case in the pH 4 structure, where the Cys104 thiol group is not spatially positioned to participate in a first sphere Cu-coordination shell with the other ligands (Figure 2.3A). Thus we suggest based on the constricting of the homotetramer and the movement of the Cys104 side chain to enable trigonal Cu(I) coordination that the conformation observed in the crystal at pH 6 can be considered as a 'quasi Cu(I)-bound' state. The rearrangement of Cys104 side chain at pH 6 also has an impact on a few of the predicted DNA binding residues mentioned in section 1.4.6, most notably Arg54, Arg57, Arg129 and Arg132 (Figure 2.4, orange). All arginines are rotated towards the

centre of the tetramer in the CsoR pH 6 structure and this rotational change may have an impact on decreasing DNA binding affinity by CsoR at a quasi Cu(I)-bound state.

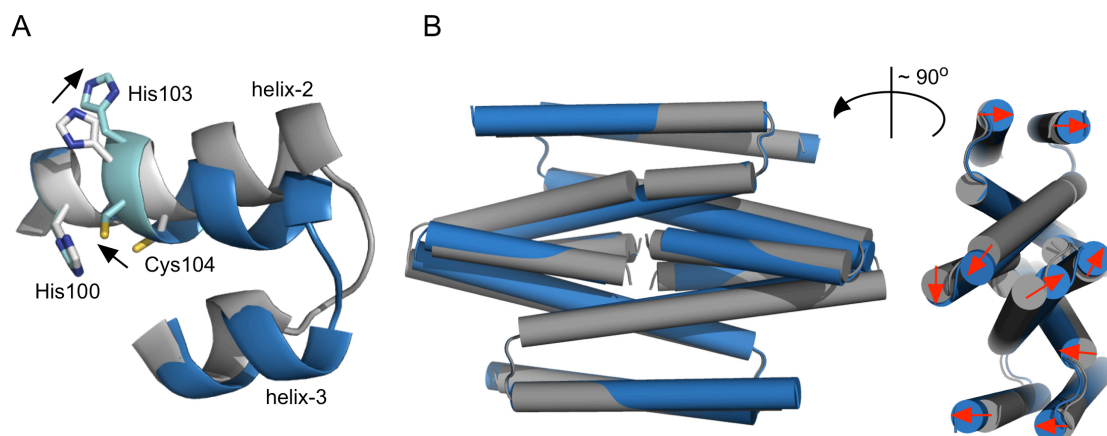


Figure 2.3 - (A) Conformational changes at one of the Cu(I) binding sites (gray pH 4 and blue pH 6) in the *S. lividans* CsoR homotetramer. The creation of the bulge as a result of breaking the helix-2 geometry is clearly seen and coloured light blue, with arrows indicating the direction' state. (B) Global structural changes between the pH 4 (gray) and pH 6 (blue) structures. The red arrows indicate the direction of helix movements from pH 4 to pH 6, revealing opposite directionality within each dimer pair.

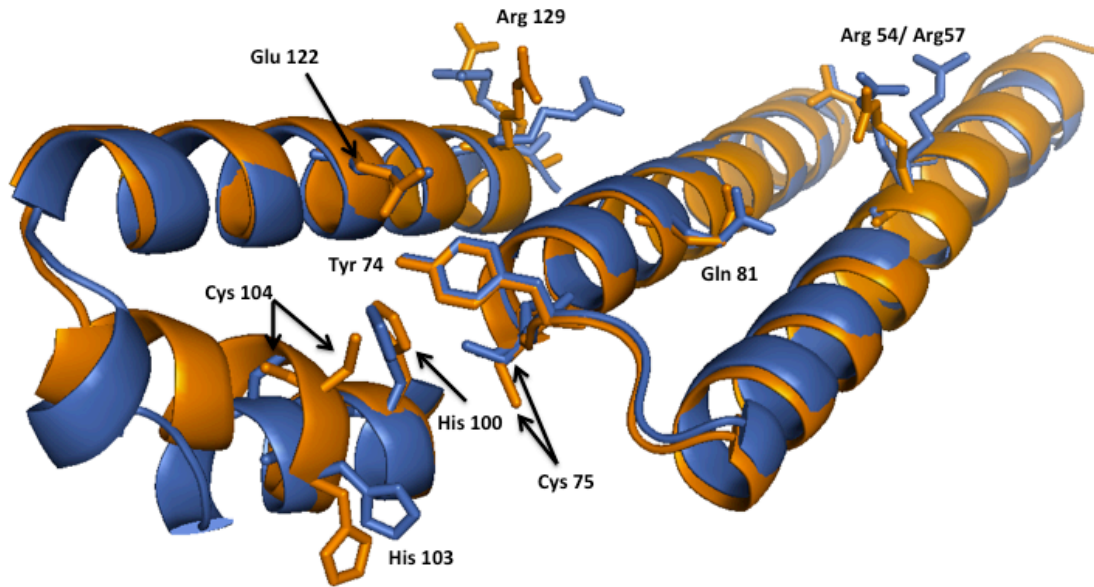


Figure 2.4 - Superposition of *S. lividans* CsoR at pH 4 (blue) with pH 6 (orange) structures focused on both predicted DNA and Cu(I) binding sites. Cys104 must go a movement into a “locked” position and closer to Cys75. Interruption or a kink is observed at $\alpha 2$ for CsoR pH 6 (orange), which is absent on CsoR pH 4 (blue). All images were generated with MacPyMOL.

2.3.3 Conformational switching involves a concertina effect of the α 2-helix

Figure 2.3B showed an overlay of the two *S. lividans* CsoR homotetramers, with red arrows to indicate the directionality of the movement in the helices between conformers. It is apparent from these static overlays that significant helical movement occurs, on which the α 2-helix is particularly affected. A better appreciation of these helical movements is documented on supplementary movies S1 and S2 through morphing between the two structures (front and rotated 90° to the side). A clear concertina effect is observed at the C-terminal ends of each of the α 2-helices creating the bulge and forcing the Cys104 side chain to reorientate into the Cu(I) binding site (movie S1) as seen from the front of the homotetramer. After an approximate 90° rotation to the side that permits a better observation of the dimer of dimers, each dimer in the homotetramer moves in the opposite direction to the other creating a twist-like motion as the α 2-helix bulge forms to accommodate the binding of Cu(I) (Figure 2.3B and movie S2).

Operator DNA sequences for Cu(I)-CsoR members consist of a 5'TAC/GTA-3' (known as a GTA dyad) inverted repeat flanking G-tracts of variable lengths (Grossoehme *et al.*, 2011; Dwarakanath *et al.*, 2012; Tan *et al.*, 2014). These poly-d(G) duplexes favour A-DNA conformation which is driven by guanine base interactions, but in aqueous solution result in a unique B/A-hybrid DNA structure that is different from A or B-DNA alone. It has been previously demonstrated that the apo-state of *S. lividans* CsoR binds operator DNA through a mechanism of conformational selectivity, whereby the binding of two CsoR homotetramers lock the G-tracts into the A-conformation (Tan *et*

al., 2014). Based on the flexibility inherent in the homotetramer as demonstrated by movies S1 and S2 and a conformational selective binding mechanism, it is proposed that the tetrameric face of the apo-state (representative in the pH 4 structure) is optimised at structural level to select and stabilise the A-conformation of the operator DNA to form a 'sandwich' complex.

2.3.4 Conformational switching induces an electrostatic redistribution of the tetrameric surface

Constriction of the homotetramer as observed in the 'quasi Cu(I)-bound state' of the *S. lividans* CsoR pH 6 structure coincides with a number of changes involving side chain orientations on the tetrameric DNA-binding surface as indicated by a more rugged topology (Figure 2.1). Whilst the discussion in section 2.3.2 has offered insight into the global changes that occur on conformational switching between different states, the local effects these changes have on the tetrameric surface in the form of electrostatic changes are likely to influence the complex formation and disassembly.

A recent study with clade IV *G. thermodenitrificans* CsoR indicated that electrostatic occlusion may play a role in the Cu(I) induced allosteric switch. This effect affects residues which have significant contacts with the operator DNA in the apo-state and later become 'sequestered' or 'occluded' via ion pairing in the Cu(I)-bound state, thus leading to reduced operator DNA contact (Chang *et al.*, 2015). These residues are suggested to be conserved within clades and may be considered as 'regulatory' (Chang *et al.*, 2015).

An example of the impact of electrostatic occlusion in a CsoR/RcnR family metalloregulator was first observed in the clade IV *G. thermodenitrificans* CsoR. A quaternary structural ion pair that stretches across the tetramer interface (dimer-dimer interface) has been identified in the Cu(I)-bound structure, involving the side chain interactions of Glu73 (α 2-helix) and Lys101 (α 3'-helix) located at different dimers (Chang *et al.*, 2015). Through charge reversal mutations of these residues (E73K/K101E), the DNA binding properties displayed were identical to the wild type *G. thermodenitrificans* CsoR, strongly suggestive of a key allosteric quaternary structural interaction, critical to maintaining the high affinity binding in the apo-state and/or driving CsoR off the DNA upon Cu(I) binding (Chang *et al.*, 2015). Moreover, Lys101 is protected from amidination in the DNA bound and Cu(I) bound states of *Bacillus subtilis* CsoR, indicative that the Lys101 side chain is no longer available for DNA binding and sequestered (Chang *et al.*, 2011).

In the clade III *S. lividans* CsoR, Glu73 is conserved (Glu98, *S. lividans* numbering) but a positively charged residue on the α 3'-helix in a location that would allow for an ion pair is absent. However, a cross-tetramer interface pseudo ion pair is identified in the pH 6 structure between the Ne atom of Arg102 (α 2-helix) and the O δ 1 atom of Asp117 (α 3'-helix) (Figure 2.5A). This interaction, together with a hydrogen bond formed between the Arg102 side chain N η 1 atom and its own backbone carbonyl atom, ensures that the positively charged guanidino group is orientated in the opposite direction to the DNA binding face (Figure 2.1 and Figure 2.5A). In contrast, the guanidino group of Arg102 is no longer sequestered in the apo-state pH 4 structure. This

is due to the reformation of the helical geometry in the $\alpha 2$ -helix as opposed to the presence of a bulge or a kink in the 'quasi Cu(I)-bound state', that leads to the reorientation of the Arg102 side chain to point towards the DNA binding face, therefore favouring a possible interaction with operator DNA. Arg102 has not been previously identified as participating in DNA binding in *S. lividans* CsoR, but its location in the vicinity of the DNA binding tract on the tetrameric face (Figure 2.1) and its switching of side chain availability between states suggests an involvement. Arg102 is located in the vicinity of two putative Cu(I) binding residues (His100 and Cys104) and adjacent to His103 at the $\alpha 2$ -helix. With a current model that suggests a rigid state for *S. lividans* Cu(I)-bound CsoR which subsequently triggers dissociation from the DNA (Tan *et al*, 2014), it is plausible the reorientation of Arg102 side chain due to His103 and Cys104 one may contribute to the formation of these rigid state upon Cu(I) binding.

A second notable cross-tetramer interface interaction involving a residue known to interact with DNA in *S. lividans* CsoR is identified in the 'quasi-Cu(I) bound' structure. The N η 1 atom of Arg129 and the side chain O γ 1 atom of Thr80 are involved. In this interaction, that is absent in the apo-structure at pH 4, again it is caused by the repositioning of the side chain, enabling the guanidino group of Arg129 to interact with the DNA (Tan *et al*, 2014). The effect of the above described local changes and others on switching between states can be further appreciated from the generation of electrostatic potential surfaces of the two homotetramers, (Figure 2.5C and D). These reveal a striking difference. The electropositively rich corridor running northwest to southeast in the apo-state (Figure 2.5C), which has been

experimentally determined to accommodate the operator DNA in the A-conformer (Chang *et al.*, 2011; Tan *et al.*, 2014) is abolished in the 'quasi Cu(I)-bound' state (Figure 2.5D). A redistribution of electropositive charge now runs north to south along the homotetramer face, flanked by increased electronegative potential (Figure 2.5D). Therefore the structural changes associated with the compaction of the homotetramer lead to a major redistribution of charge (positive and negative) over the tetrameric face that will disrupt favoured contact with the operator DNA to maintain the A-conformer and cause the complex to disassemble.

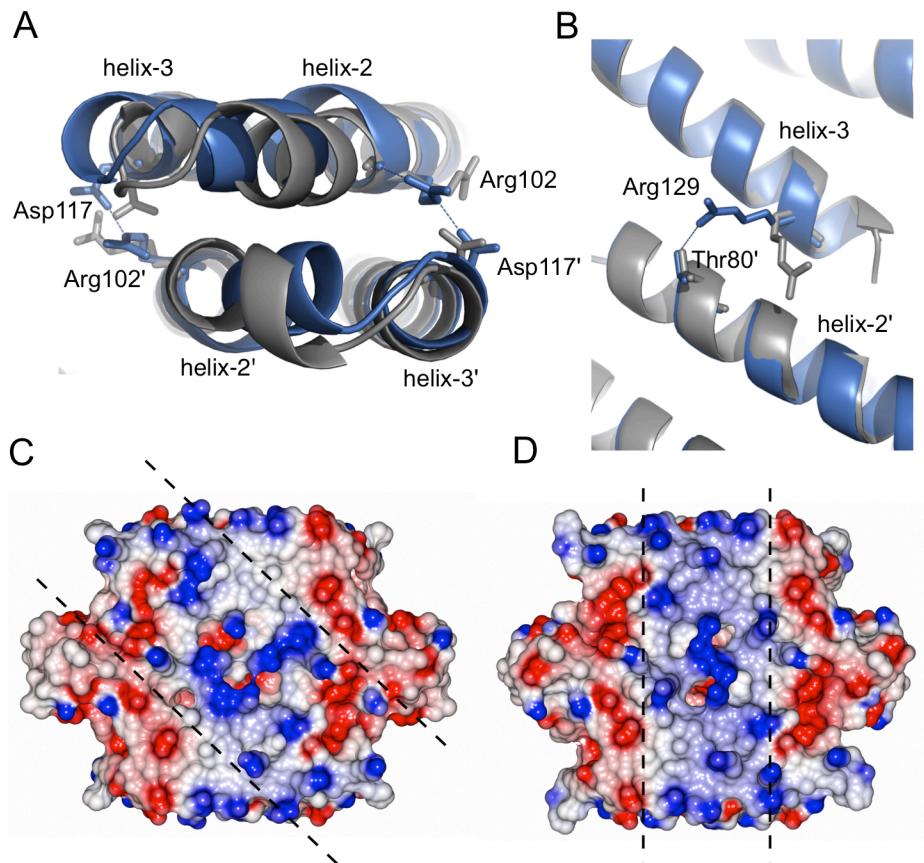


Figure 2.5 - Cross-tetramer interface interactions for (A) the Arg102 side-chain upon interaction with Asp117 and (B) Arg129 and Thr80 (dashed lines) in the quasi Cu(I)-bound structure (blue, pH 6). These interactions are absent in the apo-state (gray, pH4). Bottom: electrostatic surface representations of the pH 4 (C) and pH 6 (D) tetrameric assemblies. Dashed lines indicate in (C) indicate the electropositive corridor that binds DNA in the apo-state and in (D) the redistribution of electropositive charge in a 'north to south' direction.

2.3.5 The effect of pH on the conformational switching in *S. lividans*

CsoR

One of the basic principles of protein research is how changes at pH level can directly affect protein structure and subsequently its biological function. The amino and acidic groups of side chains are prone to protonation depending on the pH conditions, which can change the whole protein dynamics at molecular level. How both molecular and electrostatic surface representations for *S. lividans* CsoR pH 4 and pH 6 apo structures is affected is a very strong evidence of this effect combined with the shortening of the tetramer due to the concertina effect previously mentioned on section 2.3.3.

An interesting feature of the molecular surface representation of *S. lividans* CsoR pH 6 structure is the formation of a argine-rich (blue, Figure 2.1) rugged region in the shape of number '8' linking both Arg54-X-X-Arg57 DNA binding motif from one dimer of dimers to another via Gln81 (green) interconnected via Arg129/Arg132 (also suggested to be involved in DNA binding) in between, which is absent at pH 4 (Figure 2.1). Both Arg102 from each dimer are now less surface exposed at pH 6 than at pH 4, as a consequence of the reorientation of the side chain. These observations are also reflected after a 90° horizontal rotation of the tetramer, on which sharp blue rugged blobs are concentrated on a small area at the top middle at pH 6 and more uniform at pH 4.

Overall analysis of the electrostatic surface representations at pH 4 and pH 6 (Figure 2.5) can be also correlated to what was initially observed at molecular surface level. While at pH 4 the electropositive corridor is more diffused at a 'northwest to southeast' direction, at pH 6 it does shift to 'north to

south' with a considerable electropositive residue concentration localised at the vertical axis. In *G. thermodenitrificans* clade III Cu(I)-CsoR electrostatic surface representation (Chang *et al*, 2014), electropositive charges (blue) are mostly predominant over the tetrameric shape overall, especially at the Cu(I) binding region. For *S. lividans* at pH 6, electronegative charges (red) are more localised at the putative Cu(I) binding region within the tetramer.

Upon C α superposition of CsoR pH 6 apo structure (orange) with Cu(I)-CsoR from *M. tuberculosis* pH 7.5 (dark green) in Figure 2.6 in a similar manner as seen in Figure 1.13, the position of Cys104 supports evidence of a quasi-Cu(I) bound state at pH 6. This positioning of Cys104 is of vital importance to facilitate Cu(I) coordination with Cys75', due to the shortening of the distance between the two residues, a pattern observed for Cys65 in Cu(I)-CsoR from *M. tuberculosis*.

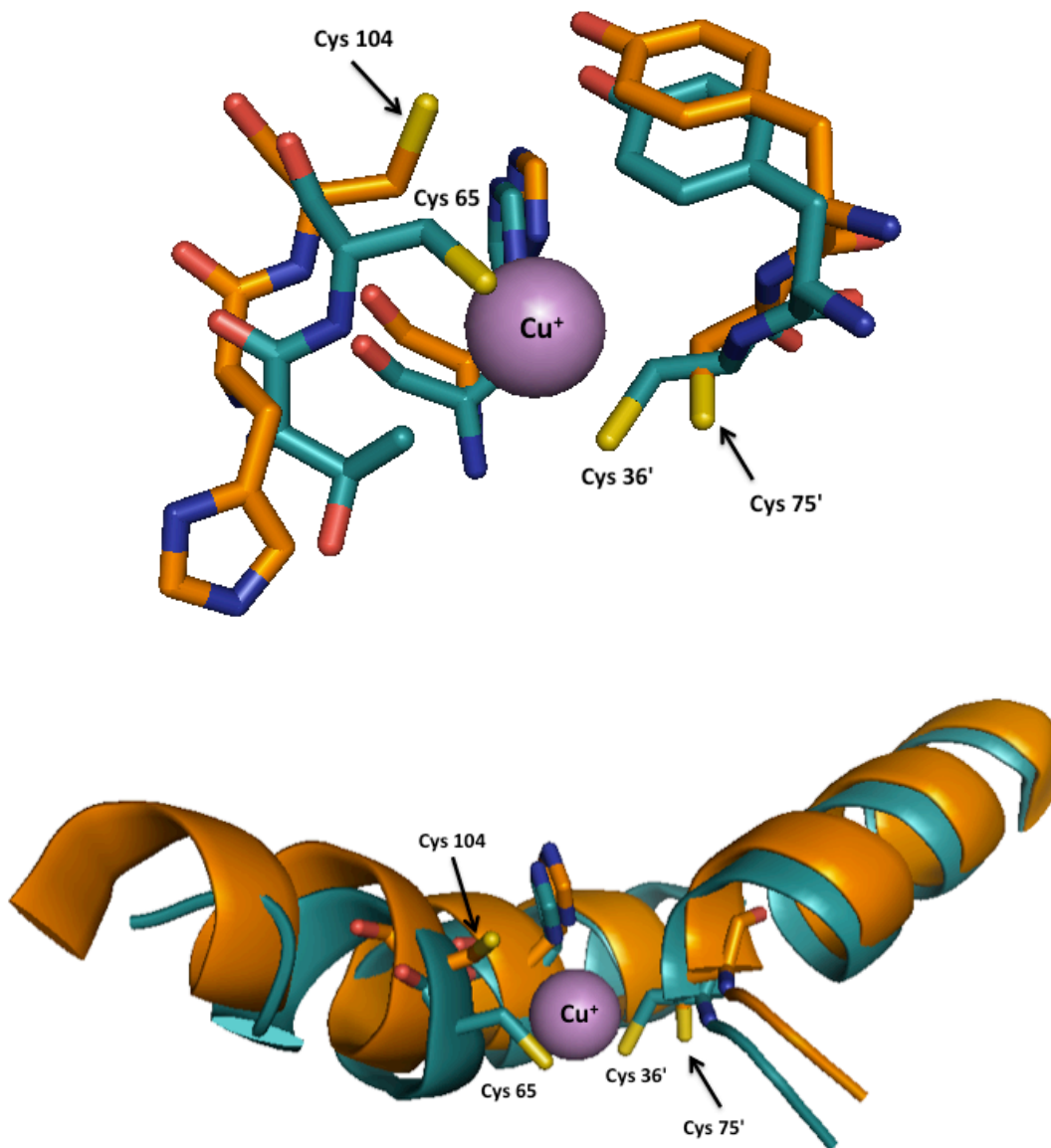


Figure 2.6 – (Top) C α superposition of the Cu(I) binding site of *M. tuberculosis* Cu(I)-CsoR (dark green) with *S. lividans* CsoR pH6 apo structure (orange). In the ‘quasi’-Cu(I) bound state in *S. lividans* CsoR pH6 , the position of Cys104 is favorable for Cu(I) binding due to the shortage of the distance between Cys75’. (Bottom) A closer look at α -helical level, with a visible kink or bulge present on CsoR pH 6 as a result of the movement of Cys104. Image generated with MacPyMOL.

Chapter 3

Structural Characterisation of CsoR mutants important for metal ion binding

3.1 Introduction

As first introduced in section 1.4.5, the crystal structure of *M. tuberculosis* Cu(I)-CsoR revealed that Cu(I) is coordinated by residues Cys36', Cys65 and His61 with a trigonal geometry, occupying positions X, Y and Z of the CsoR/RcnR first coordination sphere X-Y-Z fingerprint motif respectively (Liu *et al*, 2007; Foster *et al*, 2014b). The side chains of Cys and His residues function as copper ligands: deprotonation of sulphur and nitrogen atoms result on the formation of thiolate and imidazolate anions, respectively (Dupont *et al*, 2011; Rubino and Franz, 2012). In *S. lividans* CsoR, the putative Cu(I) binding site is formed by Cys75', His100 and Cys104, with His103 linked to His100 via a sulfate ion, as observed on the apo crystal structure at pH 4 (Dwarakanath *et al*, 2012). Other CsoR/RcnR family members share a similar pattern at the X-Y-Z primary coordination sphere, with Cys at positions X and Z (apart from *E.coli* RcnR, which features a His at positions Y and Z (Table 3.1). The distance between Cys35' and Cys65 is appropriate large to coordinate Cu(I) in *M. tuberculosis* CsoR; from the corresponding residues in CsoR, Cys75' and Cys104, the latter must undergo a significant movement for Cu(I) binding (Dwarakanath *et al*, 2012).

Table 3.1 - The X-Y-Z primary coordination sphere residues in CsoR/RcnR family. The asterisk (*) indicates that Cu(I) was found to be coordinated to these residues on the crystal structure. (Taken from Dwarakanath *et al*, 2012; Chang *et al*, 2014 and Foster *et al*, 2014b)

Metal Sensor	X (located at $\alpha' 1$)	Y (located at $\alpha 3$)	Z (located at $\alpha 3$)
<i>M. tuberculosis</i> CsoR*	Cys 36	His 61	Cys 65
<i>G. thermodenitrificans</i> CsoR*	Cys 50	His 75	Cys 79
<i>S. lividans</i> CsoR	Cys 75	His 100	Cys 104
<i>Synechocystis</i> PCC 6803 InrS	Cys 53	His 78	Cys 82
<i>E.coli</i> RcnR	Cys 35	His 60	His 64

In section 2.3.2, one of the features of the novel *S. lividans* CsoR apo structure at pH 6 was the rearrangement of Cys104 side chain and subsequent formation of a 'kink' or 'bulge' at the $\alpha 2$ helix. A closer look at the putative inter-protomer Cu(I) binding region revealed a water molecule between Cys75', His100 and Cys104, generating a molecular shape of a 'quasi Cu(I)-bound state'. Structurally speaking, a metalloregulator has two very distinct binding regions. One of these regions is specific to bind to all DNA sequences, in which the metalloregulator regulates within its regulon. A second binding region is metal-specific, on which the metal(s) sensed by a metalloregulator bind. When a metal binds to a metalloregulator, considerable structural changes must occur at the metal binding region and trigger an allosteric response at transcription level (Penella and Giedroc, 2005; Giedroc and Arunkumar, 2007; Smaldone and Helmann, 2007; Hobman, 2007; Ma *et al*, 2009; Rubino and Franz, 2012). It is of interest to understand from a structural and biochemical perspective the role of the putative Cu(I) binding residues from the X-Y-Z fingerprint and possible implications on DNA binding for *S. lividans* CsoR. In this chapter, structural and biochemical characterisation of the site-directed alanine mutants for the putative Cu(I) binding residues in *S. lividans* CsoR – C75A, H100A, H103A and C104A - were carried out. From the putative Cu(I) residues mutant set, C75A and H100A have been previously constructed and reported (Dwarakanath *et al*, 2012) while H103A and C104A are first reported in this work.

The crystal structures of C75A and C104A provided insights on how changes in the pH affects the repositioning of Cys104 to facilitate Cu(I) coordination with Cys75' and displacement of the sulfate ion.

3.2 Materials and Methods

3.2.1 Construction of the H103A and C104A CsoR mutants

Wild-type (WT) CsoR is cloned between the NdeI and HindIII restriction sites in a pET28a expression vector (Novagen). The nucleotide and corresponding amino acid sequence for CsoR is shown in Figure 3.1. The Quikchange site-directed mutagenesis method (Agilent Technologies) was used for the construction of the CsoR mutants, H103A and C104A. Quikchange is a method that permits the introduction of site-specific mutations into double-stranded plasmid DNA. Mutagenic primers (forward and reverse) for H103A and C104A were designed with the desired nucleotide change (Table 3.2)

Figure 3.1 - *S.lividans* WT CsoR sequence used as a template for site-directed mutagenesis using Quikchange method. Residues His103 and Cys104 are highlighted in blue and red, respectively.

```
ATGACGACCACCGAGGCCGGCGGAGTGCGCCCTCCCCGCCGTGGACGGGGCGGTG
M T T T E A G A S A P S P A V D G A V
AACCAGACGGCGCGCCAGGCCGAGGCGGACGGCACGGACATCGTGACCGACCACGAC
N Q T A R Q A E A D G T D I V T D H D
CGCGGCGTGCACGGGTACCACAAGCAGAAGGCCGAGCACCTCAAACGCCTGCGCCGC
R G V H G Y H K Q K A E H L K R L R R
ATCGAGGGCCAGATCCGCGGCCCTGCAGCGGATGGTCGACGAGGACGTCTACTGCATC
I E G Q I R G L Q R M V D E D V Y C I
GACATACTGACCCAGGTCTCCGCCTCCACGAAGGCCCTCCAGTCCTTCGCGCTGCAA
D I L T Q V S A S T K A L Q S F A L Q
CTGCTGGAGGAGCACCTGCGCCACTGCGTTCGCGGACGCGGCCCTCAAGGGCGGCACC
L L E E H L R H C V A D A A L K G G T
GAGATCGACGCGAAGGTGGAAGAGGCGACGAAGGCCATCGGCAGGCTACTGCGCACG
E I D A K V E E A T K A I G R L L R T
```

Table 3.2 - Site-directed mutagenic reverse and forward primers used to construct *S. lividans* CsoR mutants (A) H103A and (B) C104A. The nucleotides in red indicate the desired nucleotide change.

Mutant	Primers	GC(%)	Salt-adjusted T_m (°C)	Size (mer)
H103A	<p>Forward 5'-GAGCACCTGCGCGCCTGCGTCGCC-3'</p> <p>Reverse 5'-GGCGACGCAGGCGCGCAGGTGCTC-3'</p>	79.14	64	24
C104A	<p>Forward 5'-CACCTGCGCCACGCCGTCGCCGAC-3'</p> <p>Reverse 5'-GTCGGCGACGGCGTGGCGCAGGTG-3'</p>	79.14	64	24

Concentrations of plasmid DNA (pET28a containing the CsoR gene) and primers were 15 ng/ μ l and 75 ng/ μ l, respectively. The PCR volume was 30 μ l, consisting of 21 μ l of deionised water, 1 μ l of plasmid DNA, 1 μ l each of forward and reverse primer, 0.6 μ l of 10 mM dNTPs, 1.8 μ l of 100% DMSO, 3 μ l of 10xPfu Turbo polymerase (Agilent Technologies) buffer and 0.6 μ l of Pfu Turbo polymerase (Agilent Technologies). The PCR cycle shown in Table 3.3 was used.

Table 3.3 - PCR program set up used for the amplification of genes that encodes *S. lividans* mutants H103A or C104A using the Quikchange site-directed mutagenesis method.

Stage	Time	Temperature	Number of Cycles
Initialisation	2 min	95 °C	N/A
Denaturation	50 s	95 °C	Repeat 15 times
Annealing	1 min	58 °C	
Elongation	13 min	68 °C	
Final Hold	O/N	12 °C	N/A

PCR products were visualised on an agarose gel and then digested with DpnI for 2 h at 37 °C. DpnI is a restriction endonuclease that digests the template (i.e. parental DNA) by targeting methylated DNA present on the PCR amplification product. The digested plasmid features the desired mutation-containing PCR product, which is then subsequently used for transformation.

5 µl of DpnI-digested H103A or C104A product was inoculated into 50 µl *Escherichia coli* DH5α cells and then incubated on ice for 20 min. Cells were immediately heat shocked at 42 °C for 90 s, followed by shaking at 200 rpm for 45 min followed by plating on LB (Melford) kanamycin (50 µg/ml) agar plates for overnight incubation at 37 °C. Single colonies were picked and used to inoculate 3 ml of LB media (Melford) with 3 µl kanamycin (50 µg/l) and grown overnight at 37 °C with shaking at 200 rpm. From these cultures plasmid DNA was isolated using a GeneJet™ mini-prep kit (Thermo Scientific) and sent to GATC Biotech for DNA sequencing.

3.2.2 Over-expression and purification of CsoR and mutants

pET28a plasmids containing the desired CsoR gene for over-expression were transformed into *E. coli* BL21 (DE3) cells using the same transformation protocol as used for DH5α cells. Single transformants were picked and pre-cultured overnight in 3 ml of 2xYT media (Melford) with 3 µl kanamycin (50 mg/ml) at 37 °C and shaking at 200 rpm. A 1 ml aliquot from each of the overnight cultures was inoculated into 750 ml of 2xYT media in a 2 L Erlenmeyer flask with 750 µl kanamycin (50 mg/ml) and growth continued at 37°C and 220 rpm. The over-expression of N-terminal His₆-tagged CsoR was initiated at an OD₆₀₀ (optical density at 600 nm) range between 0.6 to

0.8, with the addition of IPTG (isopropyl- β -D-1-thiogalactopyranoside) to a final concentration of 1 mM, followed by a reduction in temperature to 25°C for overnight growth. Cultures were harvested by centrifugation at 4,000 rpm for 20 min at 4°C. The cell pellet was resuspended in Buffer A [50 mM Tris/HCl (Fisher Scientific), 500 mM NaCl (Fisher Scientific) and 20 mM imidazole (Sigma), pH 7.5]. Cell lysis was achieved through the use of an EmulsiFlex-C5 cell disrupter (Avestin). The cells were ruptured and homogenised under a dynamic high pressure between 10,000-15,000 psi, followed by subsequent centrifugation at 18,000 rpm for 20 min at 4°C. The clarified supernatant which contains the protein was loaded to a 5 ml Ni-NTA Sepharose column (GE Healthcare) previously equilibrated with 50 ml of Buffer A. On completion of loading the column was attached to an AKTAprime plus or AKTA purifier system (GE Healthcare) and linear imidazole gradient from 20 to 500 mM was initiated with Buffer B [50 mM Tris/HCl, 500 mM NaCl and 500 mM imidazole pH 7.5].

Fractions from the Ni-NTA column were pooled out and dialysed overnight against Buffer C (50mM Tris/HCl, 150 mM NaCl, 1 mM EDTA; pH 8). The dialysed protein was next loaded to a 5 ml HiTrap™ Heparin HP column (GE Healthcare) previously equilibrated with 50 ml of Buffer D [10 mM Na₃PO₄ (Sigma) pH 7] to remove DNA. A linear salt gradient from 0 to 2 mM NaCl was initiated with Buffer E (10 mM Na₃PO₄, 2 mM NaCl pH 7), with eluted fractions pooled and dialysed overnight in Buffer C to remove excess NaCl. Cleavage of the His-tag was carried out by overnight incubation with 75 KU of thrombin (Sigma) at room temperature. The thrombin-digested protein was then re-applied to the Ni-NTA column to remove any un-cleaved CsoR.

The flow-through was concentrated by using a 5,000 molecular weight cut-off centricon (Vivaspin). The concentrated protein was then applied to a G75 Sephadex gel filtration column (GE Healthcare) equilibrated with Buffer F (50 mM Tris/HCl pH 8, 150 mM NaCl, 2mM dithiothreitol (DTT) (Melford) and 4 mM EDTA. Eluted fractions from the major G75 peak were analysed by 15% SDS-PAGE gels and good-purity fractions were then concentrated, aliquoted and stored at -20 °C until required.

3.2.3 Absorbance and circular dichroism (CD) spectroscopy

Concentrations of CsoR and mutants were determined using an extinction coefficient for the monomer at 280 nm of $3105 \text{ M}^{-1}\text{cm}^{-1}$ using a Cary50 spectrophotometer (Varian). Samples for CD were exchanged into 10mM potassium phosphate (Fisher Scientific), 50 mM potassium fluoride (Fisher Scientific) pH 7.0 using a PD-10 column (GE-Healthcare) followed by concentrating. All CD experiments were performed with 300 μl of 20 μM protein on an Applied Photophysics Chirascan circular dichroism spectrophotometer (Leatherhead, UK) connected to a thermostatic cell holder with a controlled Peltier system. Far-UV circular dichroism spectra were acquired between 175 - 260 nm at 20 °C. Thermal denaturation studies for WT and CsoR mutants were carried out by monitoring the decrease in ellipticity at 222 nm over a temperature range of 0 – 96 °C. To assess helix-coil transitions from the CD spectra, fractional helicity (F_h) was calculated as follows (Tan *et al*, 2014):

$$Fh = \frac{\theta_{222} - \theta_x}{\theta_{222 \max} - \theta_x} \text{ (Eqn 3.1)}$$

with the following parameters:

θ_{222} = molar residue elipicity (MRE) at 222 nm

$\theta_{222 \max}$ (theoretical maximum for 100% helicity)

$$\theta_{222 \max} = (-44400 + 250T) * (1 - k/Nr) \text{ (Eqn 3.2)}$$

T = temperature (°C)

k (wavelength constant at 222 nm) = 2.4

Nr – number of residues of the protein, for CsoR/mutants = 133

3.2.4 Electrospray ionisation mass spectrometry (ESI-MS)

Samples for mass spectrometry were first exchanged into 1 M ammonium acetate and then diluted 1:20 with 50% methanol and 1% formic acid. A Micromass Quattro Ultima triple quadrupole instrument was used to acquire masses, at the following settings: capillary voltage 1.7 kV, cone voltage 80-120V, cone gas 100 litre/h. Data acquisition and processing were carried out through MassLynx software (Waters, Manchester, UK).

3.2.5 Crystallisation and structural determination of CsoR mutants

All CsoR mutant samples used for crystallisation were prepared in Buffer F (50mM Tris/HCl pH 8, 150 mM NaCl, 2mM DTT (Melford) and 4 mM EDTA) and concentrated to 1 mM in a 500 μ l sample. Initial random crystal screening was carried out using a set of commercially available 96-well screen blocks mounted on a Gryphon robotic crystallisation suite (Art Robbins

Instruments), each one with a different chemical composition per well. 96-well sitting drop crystallisation plates were used at this stage, and incubated at 20 °C. Crystals were grown in a period of a week. Crystals were optimised manually using 24-well plates using the hanging drop method. Optimisation of crystal conditions was based on further refinement of the original crystal hit condition, by detailed screening ranging from different precipitant and/or solvent concentration on the reservoir solution.

A 1 µl protein sample was mixed with either 1 or 2 µl of reservoir solution and protein crystals suitable for X-ray diffraction experiments were grown at 20 °C within a week. Single crystals were transferred to a cryoprotectant solution (reservoir solution with 20 % glycerol for all crystals). Subsequent flash-cooling to 100 K in liquid nitrogen was carried out for storage before transportation and measurement. Crystallography data was collected at Diamond Light Source beam line I04-1 using a Pilatus detector and an X-ray wavelength of 0.9163 Å.

3.2.6 Data processing and analysis

Diffraction images were initially indexed, refined and then integrated with iMosflm (Battye *et al*, 2011). Integrated diffraction data was later merged using Scala (Evans, 2006) and Aimless on the CCP4i suite (Collaborative Computational Project, Number 4, 1994). *S. lividans* apo-CsoR at pH 4 structure (PDB accession number: 4ADZ; Dwarakanath *et al*, 2012) was used as the search model for molecular replacement for C75A pH 4 and pH 5 structures, while C75A pH 5 was used for C104A pH5 and pH6 using Phaser (McCoy *et al*, 2007). Models were then refined by maximum likelihood methods in Refmac5 (Murshudov *et al*, 2011) and rebuilt between refinement

cycles in Coot (Emsley and Cowtan, 2004). Riding hydrogen atoms were added when refinement of the protein atoms had converged. Models were validated throughout using the Molprobit server (Davis *et al*, 2007).

3.3 Results and Discussion

3.3.1 Initial characterisation of the H103A and C104A mutants

DNA sequencing corroborated that the nucleotide changes introduced by PCR using the respective primers in Table 3.1 to give the H103A and C104A mutants of *S. lividans* CsoR were successful. The over-expression and purification of these mutants were as previously described for the WT CsoR (Dwarakanath *et al*, 2012). Gel-filtration gave a major peak eluting at ~ 53 ml (Figure 3.2), which was consistent with the wild-type protein, and from the calibration curve of the G75 column, it indicated that a tetramer assembly is maintained in solution for these mutants. SDS-PAGE analysis of the fractions eluted from the major peak in Figure 3.2A for the C104A mutant, showed relatively pure protein, deemed suitable for further experiments. Similar results were also obtained for the H103A mutant (data not shown). Denaturing mass spectrometry of the mutants gave masses for the monomer of 14,675.8 Da for H103A and 14,706.9 Da for C104A, which matched the values calculated in ProtParam without the His₆-tag (data not shown). The two new CsoR mutants, H103A and C104A were successfully over-expressed and purified from *E.coli* BL21 (DE3) cells (Figures 3.3A and B, respectively). Together with C75A and H100A (Dwarakanath *et al*, 2012), the full set of site-directed alanine mutants for the putative Cu(I) binding site residues was successfully completed.

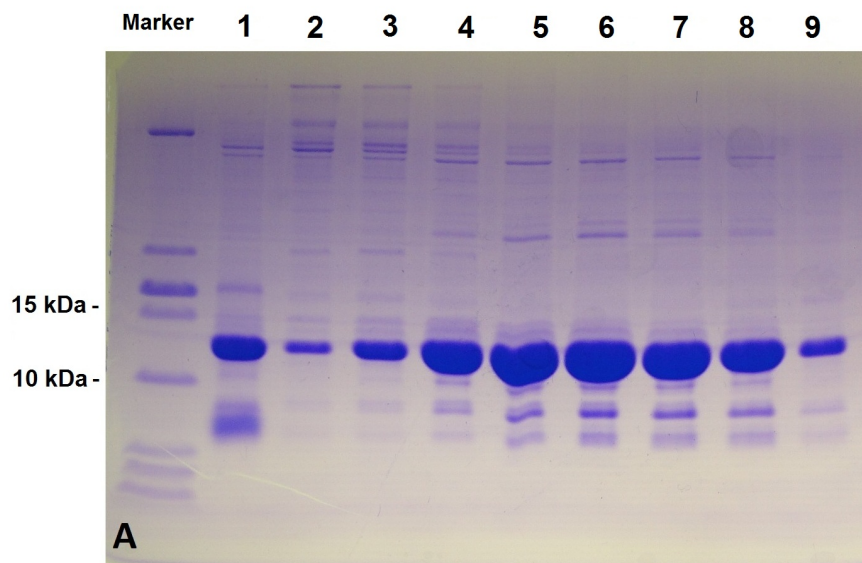
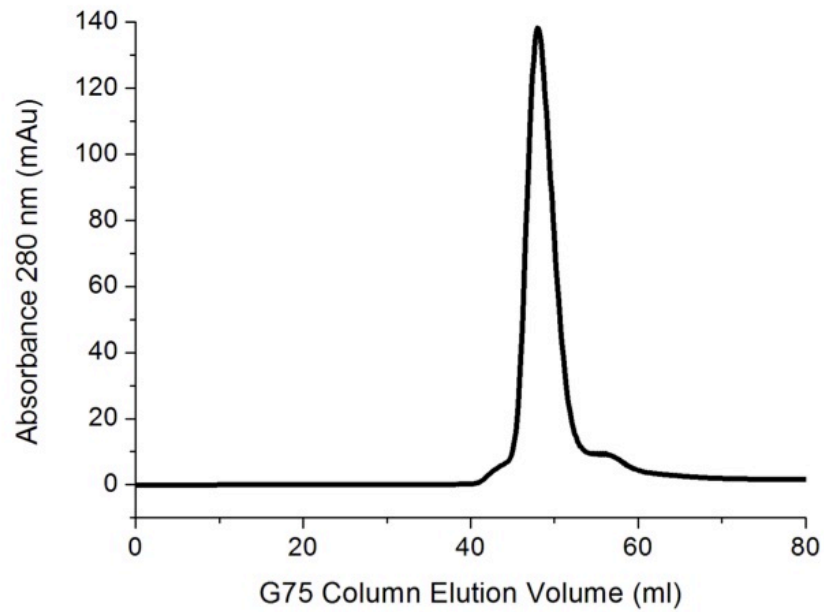


Figure 3.2 - (A) G75 gel filtration elution profile for CsoR mutant C104A. Buffer F (50mM Tris pH 8, 150 mM NaCl, 2mM DTT and 4 mM EDTA). (B) Coomassie stained 15% SDS-PAGE gel for G75 Sephadex column fractions of CsoR^{SI} mutant C104A. Marker is 10 ml PageRuler™ Unstained Low Range Protein Ladder (Fermentas). 10 ml of each corresponding fraction to a G75 peak at around 53 ml was loaded on lanes 2-9 (A). Lane 1 (A) is 10 ml C104A post thrombin digest.

3.3.2 CD spectroscopy of wild-type CsoR and mutants

The CD spectra of the *S. lividans* WT CsoR and mutants C75A, H100A, H103A and C104A are shown in Figure 3.3 for comparison. In all cases the CD spectra shows minimum mean residue ellipticity (MRE) at 208 and 222 nm, which were strongly indicative of a α -helical secondary structure. The introduction of an alanine residue on CsoR mutants did not have a major conformational change effect on protein folding. The mutations are located on a loop near the start of α_3 helix (C75A) and within α_3 helix itself (H100A, H103A and C104A). An increase in percentage helicity relative to WT CsoR was observed: CsoR (42%) < C104A (44%) < C75A (47%) < H103A (49%) < H100A (51%), which was attributed to the α -helical stabilising properties of alanine.

In comparison with WT CsoR, a slight increase in helicity was observed for the histidine mutants (H100A and H103A). This increase could be attributed to the loss of the imidazole ring, which has a strong aromatic character with a chromophore effect due to the presence of 6 delocalized π electrons on the ring. As for both cysteine mutants (C75A and C104A), the loss of the nucleophilic thiol side chain and its two electron pairs from the sulphur atom had no considerable impact on the helicity.

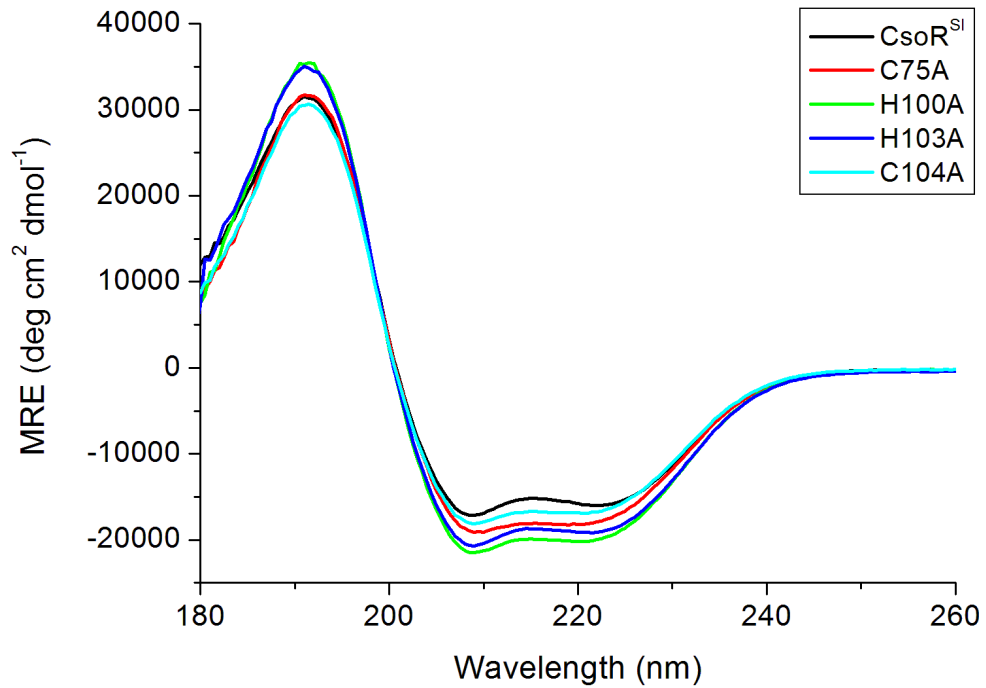


Figure 3.3 - Far-UV circular dichroism spectra for *S. lividans* WT CsoR (black) and C75A (red), H100A (light green), H103A (blue) and C104A (light blue) mutants at 20°C. Peaks at 208 and 222 nm were indicative of a α -helical character also for CsoR mutants, which were not affected with the introduction of an alanine mutation. Samples were 300 ml of 20mM protein in CD buffer (10mM potassium phosphate, 50 mM potassium fluoride pH 7.0).

Thermal denaturation profiles at 222 nm for the H103A and C104A mutants compared to WT and the C75A and H100A mutants are shown in Figure 3.4 below. The thermal melt temperature (T_m) for WT CsoR was 82°C, which indicated a high level of thermal stability. The T_m increase pattern for the CsoR mutants was observed:

H100A (76 °C) < C104A (79 °C) < H103A (80 °C) < C75A (81 °C).

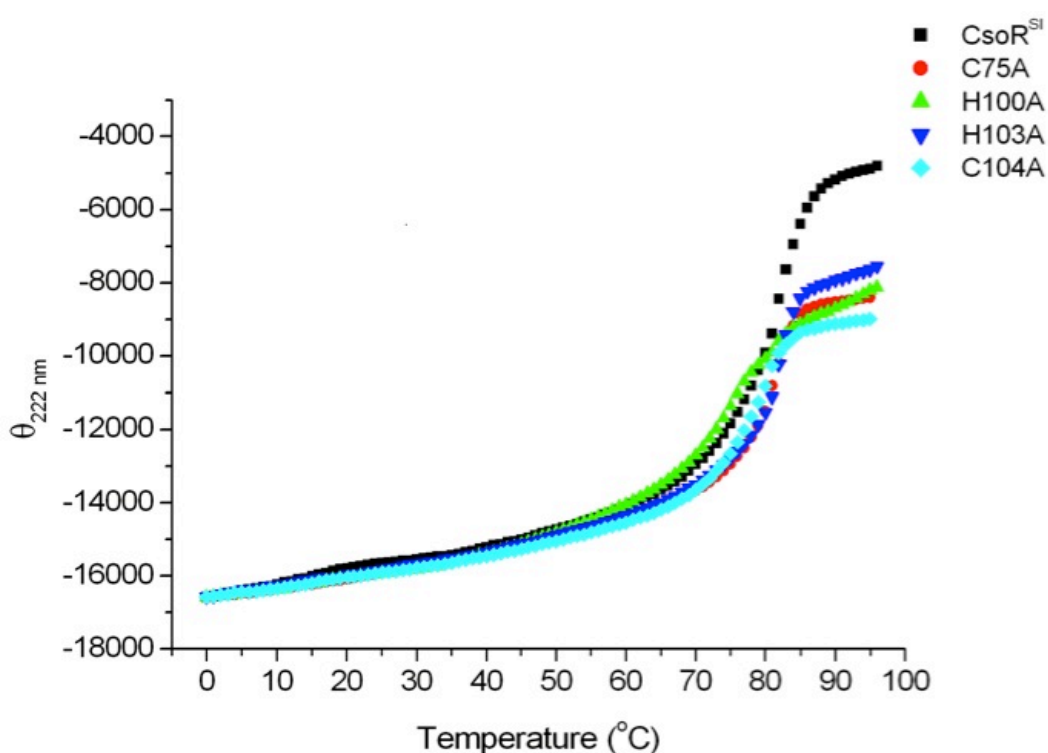


Figure 3.4 - Thermal denaturation spectra at 222 nm for *S. lividans* WT CsoR and C75A (red), H100A (light green), H103A (blue) and C104A (light blue) mutants. The temperature ranged between 0°C to 96°C was applied. Thermal melt temperatures were in the range between 76 °C to 82 °C. Samples were prepared with 300 μ l of 20 μ M protein in CD buffer (10 mM potassium phosphate, 50 mM potassium fluoride pH 7.0).

3.3.3 Crystallisation of CsoR mutants

All CsoR mutants (C75A, H100A, H103A and C104A) were subjected to crystallisation trials in their apo form, i.e., in the absence of Cu(I). Only the C75A and C104A proteins yielded crystals suitable for X-ray diffraction. Initial hits were observed on 96-well robot trays (Table 3.4), which were then further manually optimised on 24-well trays (Table 3.5) with a 1: 2 protein to precipitant ratio.

Table 3.4 - Crystallisation conditions for CsoR mutants C75A and C104A at initial screening stage using 96-well robot plates.

Protein Crystal	Composition of the Reservoir Solution
C75A	0.1 M sodium citrate pH 4.6, 1.6 M ammonium sulfate
C75A	0.1 M sodium citrate pH 5.0, 1.6 M ammonium sulfate,
C104A	0.1 M citric acid pH 5.0, 1.5 to 1.7 M ammonium sulfate, pH 5.0
C104A	0.1 M MES [2-(N-morpholino) ethanesulfonic acid] pH 6.0, 1.6-1.7 M ammonium sulfate

Table 3.5 - Crystallisation conditions for CsoR mutants C75A and C104A on 24-well optimisation plates.

Protein Crystal	Composition of the Reservoir Solution
C75A	0.1 M sodium citrate pH 4.0, 1.35 M ammonium sulfate
C75A	0.1 M sodium citrate pH 5.0, 1.6 M ammonium sulfate,
C104A	0.1 M citric acid pH 5.0, 1.56 M ammonium sulfate, pH 5.0
C104A	0.1 M MES [2-(N-morpholino) ethanesulfonic acid] pH 6.0, 1.7 M ammonium sulfate

3.3.5 Crystal structures of the C75A and C104A mutants of *S. lividans* CsoR

3.3.4.1 C75A pH 4 and pH 5 structures

The crystal structure of C75A pH 4 was determined to a resolution of 1.72 Å (Figure 3.5, left). From crystals of CsoR mutant C75A grown at pH 4 in its apo form, an orthorhombic $P2_122_1$ space group symmetry with two protomers (chain A and B) located in the asymmetric unit were observed, similar to WT CsoR at pH 4 (Dwarakanath *et al*, 2012). Well-defined electron density was only observed for residues 44 to 133 in each protomer, while residues 1 to 43 are suggested to be in disorder. Each C75A pH4 monomer was formed by 3 continuous α -helices in an anti-parallel alignment (α_1 – residues 44 to 70, α_2 – residues 76 to 105 and α_3 – 114 to 133), with connecting hairpin loops between α_1/α_2 and α_2/α_3 helices. A homotetrameric assembly formed by a dimer of dimers was observed, indicating that the punctual alanine mutation did not have an effect on the overall structure assembly. No major structural changes were observed at both N- and C-terminal regions. A $C\alpha$ secondary-structure superposition with the wild-type CsoR pH 4 structure at the putative Cu(I) binding site revealed that the mutation caused no rearrangement of any of the metal binding ligands, His100, Cys104 (Figure 3.6A). No major differences were present at the predicted DNA binding residues (Arg54, Arg57, Gln81, Arg129 and Arg132) due to the mutation of Cys to Ala75. In comparison with WT CsoR at pH 4, a corresponding electron density that matched to a sulfate ion was present between His103 and His100 respectively (Figure 3.7A).

The crystal structure of C75A pH 5 was determined to a resolution of 1.93 Å (Figure 3.6, right). From crystals of CsoR mutant C75A grown at pH 5 in its apo form, a tetragonal $I4_122$ space group symmetry was determined with a single protomer found in the crystallographic asymmetric unit, which was also observed for the WT CsoR at pH 6 structure in section 2.3.1 in Chapter 2. Well-defined electron density was only observed for residues 41 to 133 in each protomer, while residues 1 to 40 are suggested to be in disorder. Each C75A pH5 monomer was formed by 3 continuous α -helices in an anti-parallel alignment (α_1 – 41 to 70, α_2 - 76 to 105 and α_3 – 117 to 133), also with connecting hairpin loops between α_1/α_2 and α_2/α_3 helices. A homotetramer assembly formed by a dimer of dimers was also observed (and similar to C75A pH 4 structure), which indicated that the punctual alanine mutation did not have an effect on the overall structure assembly even at a higher pH. A $C\alpha$ secondary-structure with WT CsoR pH 4 structure revealed a similar disruption located at the α_2 -helix with the presence of a ‘bulge’ or ‘kink’ beginning at His103 (Figure 3.7C) as also observed for the WT CsoR pH 6 structure previously described in section 2.3.2. This event also affected the position of adjacent residue Cys104, moving upwards into a spatial position that mimics a metal ion coordination state of this residue (Figure 3.7C). No major differences were present at the predicted DNA binding residues (Arg54, Arg57, Gln81, Arg129 and Arg132) due to the mutation of Cys75 to Ala75. In comparison with WT CsoR at pH 4 and pH 6 structures, no corresponding electron density that matched either to a sulfate ion or a water molecule was present between His103 and His100 respectively (Figure 3.7B).

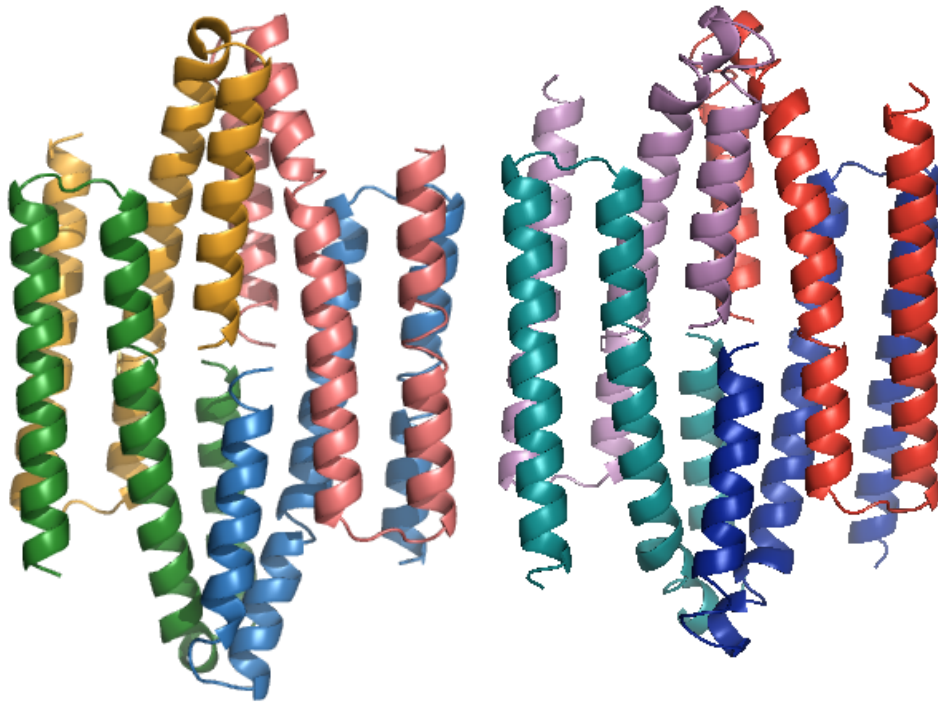


Figure 3.5 - Crystal structures of *S. lividans* CsoR 1.72 Å C75A pH 4 (left) and 1.93 Å C75A pH 5 (right) mutants. Both structures constitute a tetramer assembly. All images were generated with MacPyMOL.

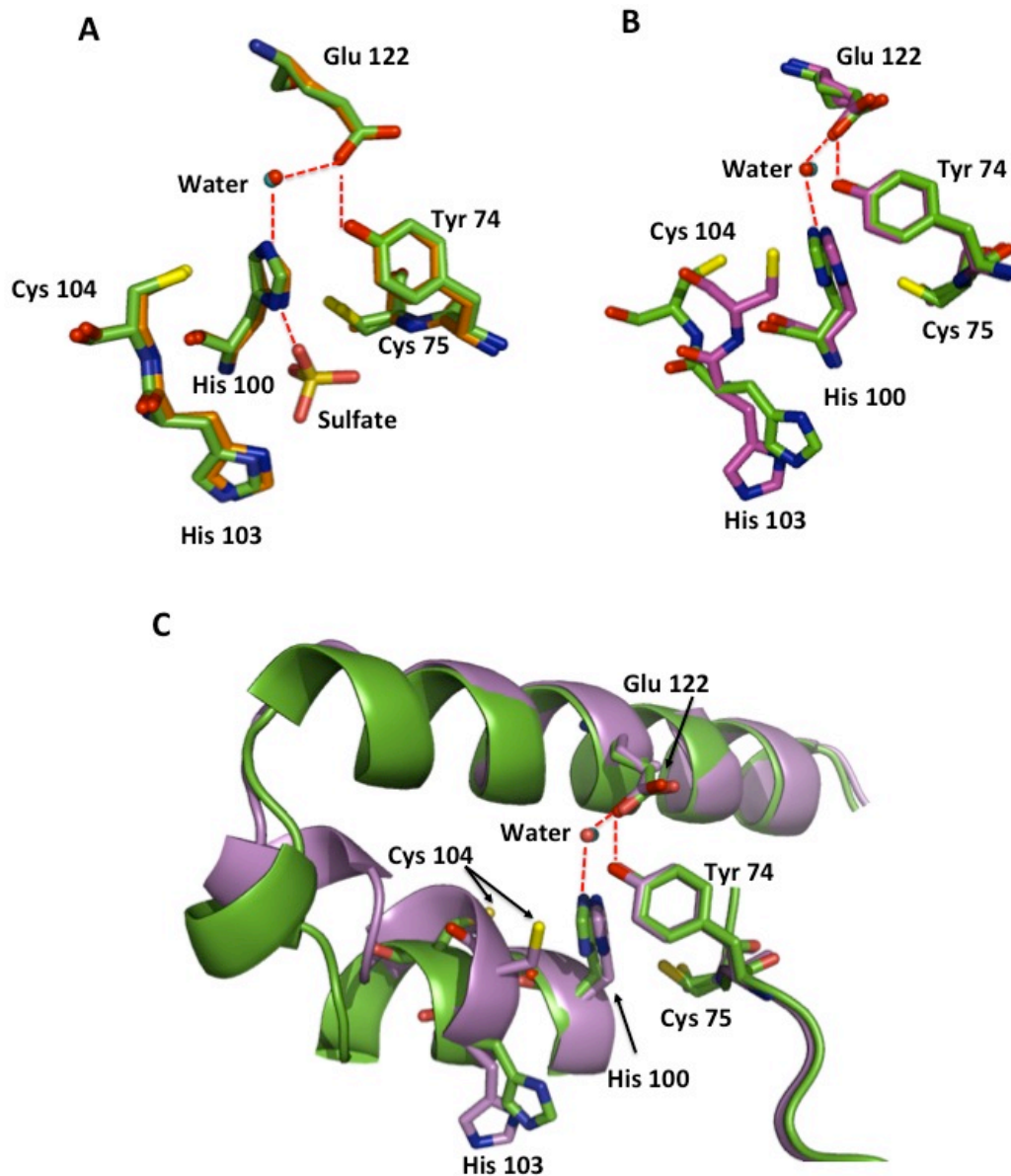


Figure 3.6 - (A) Superposition of *S. lividans* CsoR pH 4 (green) with C75A pH 4 (orange). (B) Superposition of *S. lividans* CsoR pH 4 (green) with C75A pH 5 (pink). For Cu(I) binding, Cys104 must undergo into a “locked” position and closer to Cys75. (C) Interruption or a kink is observed at α -helix 2 for C75A pH 5 (purple), which is absent on CsoR pH 4 (green). All images were generated with MacPyMOL.

As for the predicted DNA binding residues in CsoR located at α 1-helix (Arg54, Arg57), α 2-helix (Gln81) and α 3-helix (Arg129 and Arg132) (Tan *et al*, 2014), no major conformational changes were observed on the comparison between C75A pH 5 and both wild-type CsoR pH4 and pH6 structures (Figure 3.7) due to the introduction of a kink at the predicted Cu(I) binding site. Small rotational residue changes for residues Arg57 and Arg132 were observed but neither had an impact on the α -helical character of α 1 and α 2.

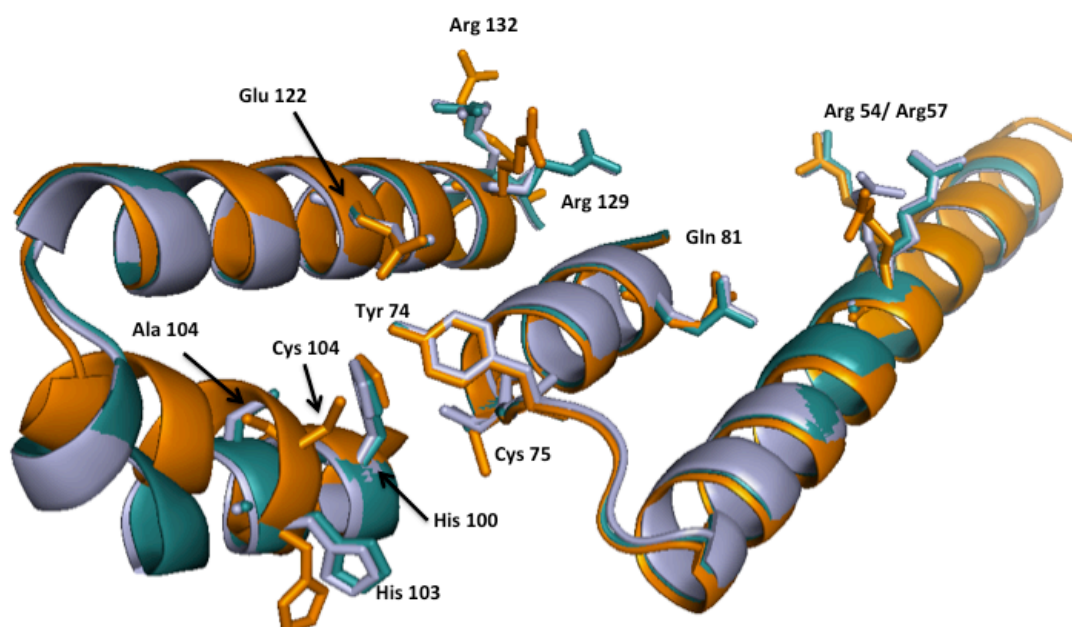


Figure 3.7 - Superposition of *S. lividans* CsoR pH 4 (light violet) with C75A pH 4 (deep teal) and pH 6 (orange). For Cu(I) binding, Cys104 must go into a “locked” position and closer to Cys75. An interruption or a kink is observed at α -helix 2 for C75A pH 5 (purple), which is absent on WT CsoR at pH4 structure (green). All images were generated with MacPyMOL.

3.3.4.2 C104A pH 5 and pH 6 structures

The crystal structure of C104A pH 5 was determined to a resolution of 2.02 Å (Figure 3.8, top). From crystals of CsoR mutant C104A grown at pH 5 in its apo form, a tetragonal $I4_122$ space group symmetry was determined with a single protomer found in the crystallographic asymmetric unit, similar to WT CsoR pH 6 and C75A pH 5 structures. Well-defined electron density was only observed for residues 42 to 133 in each protomer, while residues 1 to 41 are suggested to be in disorder. Each C104A pH5 monomer was formed by 3 continuous α -helices in an anti-parallel alignment ($\alpha1$ – residues 42 to 70, $\alpha2$ – 76 to 105 and $\alpha3$ – 117 to 133), also with connecting hairpin loops between $\alpha1/\alpha2$ and $\alpha2/\alpha3$ helices. As also observed for C75A pH 4 and pH 5 structures, C104A pH5 is a homotetramer assembly constituted of a dimer of dimers, which indicated the substitution of Cys104 to Ala 104 did not have an effect on the overall structure assembly, even at a higher pH in comparison to the WT CsoR structure at pH 4. A $C\alpha$ secondary-structure comparison with the WT CsoR pH 4 structure revealed a similar disruption located at the $\alpha2$ -helix with the presence of a ‘bulge’ or ‘kink’ beginning at His103 (Figure 3.9) as also observed for WT CsoR pH 6 and C75A pH 5. This event also affected the position of the adjacent residue Ala104, moving upwards into a spatial position in a similar fashion to what occurred to Cys104 on both CsoR pH 6 and C75A pH 5 structures. From the putative DNA binding residues, both Arg129 and Arg132 had their rotation altered. No corresponding electron density that matched either to a sulfate ion or a water molecule was present between His103 and His100 respectively (Figure 3.9).

The crystal structure of C104A pH 6 was determined to a resolution of 2.05 Å (Figure 3.8, bottom). From crystals of CsoR mutant C104A grown at pH 5 in its apo form, a tetragonal $I4_122$ space group symmetry was determined with a single protomer found in the crystallographic asymmetric unit, similar to WT CsoR pH 6 and C75A pH 5 structures. Well-defined electron density was also only observed for residues 42 to 133 in each protomer, while residues 1 to 41 are suggested to be in disorder. Each C104A pH 6 monomer was formed by 3 continuous α -helices in an anti-parallel alignment (α_1 – residues 42 to 70, α_2 - 76 to 111 and α_3 – 114 to 133), also with connecting hairpin loops between α_1/α_2 and α_2/α_3 helices. As also observed for WT CsoR pH 6, C75A and C104A pH 5 structures, C104A pH 6 is a homotetramer constituted of a dimer of dimers, which indicated the substitution of Cys104 to Ala104 did not have an effect on the overall structure assembly even at a higher pH.

A $C\alpha$ secondary-structure comparison with WT CsoR pH 4 structure also revealed a similar disruption located at the α_2 -helix with the presence of a 'bulge' or 'kink' beginning at His103 (Figure 3.10) as also observed for WT CsoR pH 6, C75A and C104A pH 5 structures. This event also affected the position of adjacent residue Ala104, moving upwards into a spatial position in a similar fashion to what occurred to Cys104 on both CsoR pH 6 and C75A pH 5 structures. From the putative DNA binding residues, small rotational conformational changes for residues Arg57 and Arg132 were observed (Figure 3.10).

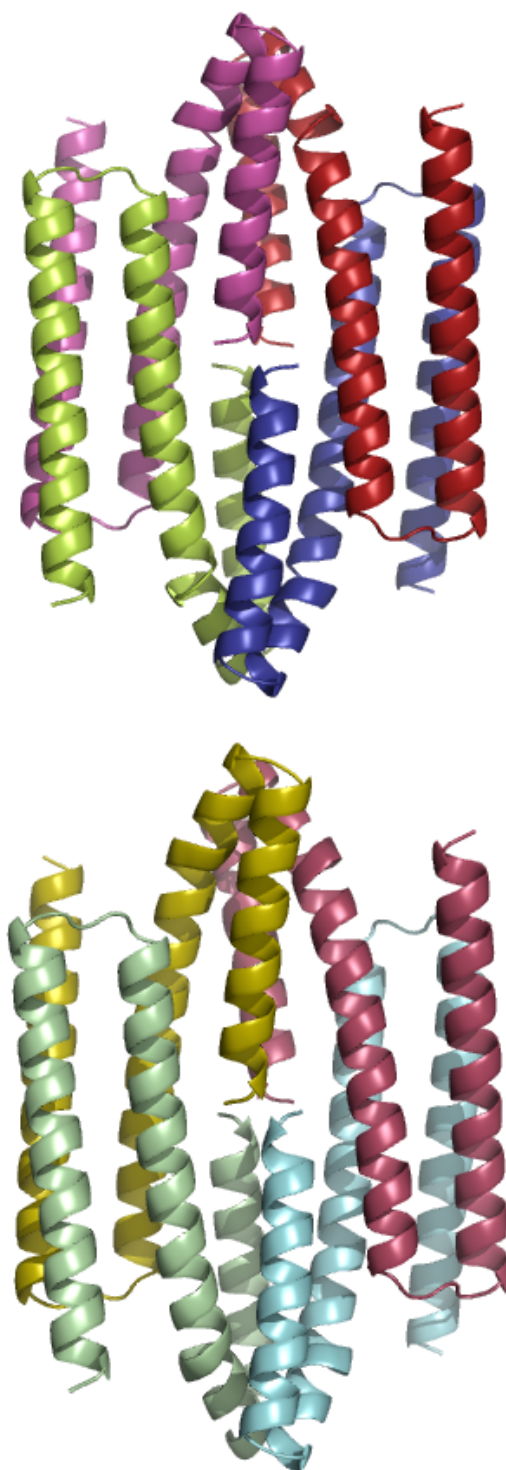


Figure 3.9 - Structures of 2.02 Å C104A pH 5 structure (above) and 2.05 Å C104A pH 6 (below). Both structures constitute a tetramer assembly. All images were generated with MacPyMOL.

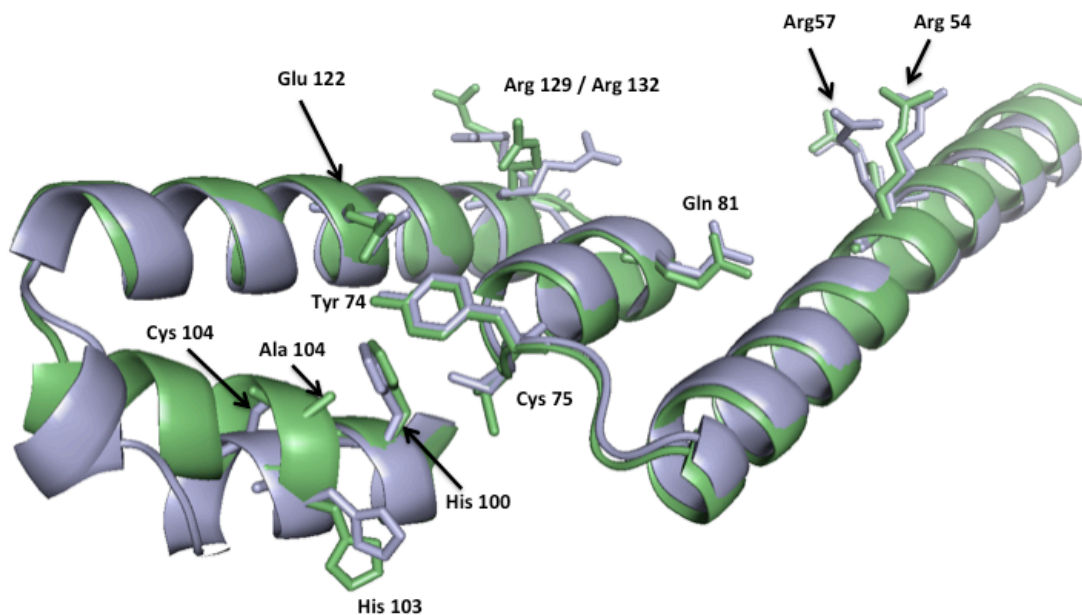


Figure 3.10 - Superposition of CsoR pH 4 (light purple) with C104A pH 5 (light green). Ala104 mocks a similar movement Cys104 must go into a “locked” position and closer to Cys75. An interruption or a kink is observed at α 2 for C104A pH 5 (light green), which is absent on CsoR pH 4 (light purple). All images were generated with MacPyMOL.

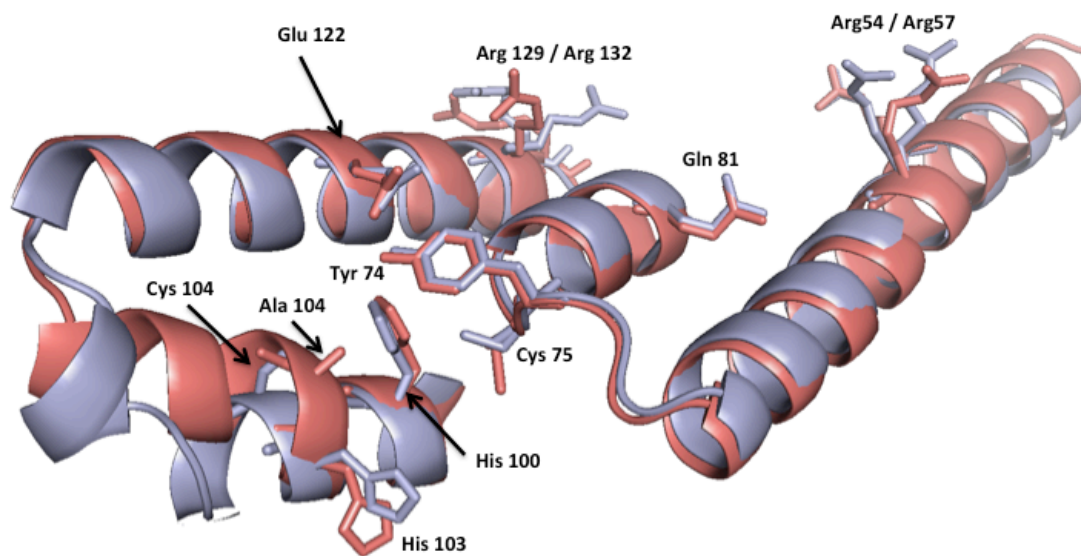


Figure 3.11 - Superposition of CsoR pH 4 (light purple) with C104A pH 6 (light red). Ala104 mocks a similar movement Cys104 must go into a “locked” position and closer to Cys75. Interruption or a kink is observed at α_2 for C104A pH 6 (light red), which is absent on CsoR pH 4 (light purple). All images were generated with MacPyMOL.

Table 3.6 summarises crystal data collection and processed statistics for C75A (pH 4 and pH 5) and C104A (pH 5 and pH 6).

Table 3.6 - Data collection and processing statistics of WT CsoR, C75A and C104A mutants obtained through Scala (Evans, 2006) and Refmac5 (Murshudov *et al*, 2011) on the CCP4i suite. Numbers in parentheses represent statistics of the outer shell. The resolution range for all structures is between 1.72 – 2.05 Å for the outer shell, which indicates high accuracy. Changes in the space group are pH dependent.

CsoR Mutants	C75A pH 4	C75A pH 5	C104A pH 5	C104A pH 6
Resolution range, overall (Å)	45.71 - 1.72	39.61– 1.93	28.67 - 2.02	39.80 – 2.05
Outer Shell (Å)	1.81 – 1.72	2.03 – 1.93	2.13 - 2.02	2.16 – 2.05
Space Group	P2 ₁ 22 ₁	I4 ₁ 22	I4 ₁ 22	I4 ₁ 22
Unit Cell Parameters (Å)	40.77, 54.50, 91.50	89.77, 89.77, 101.38	84.54, 89.54, 103.1	89.69, 89.69, 102.3
Total No. of Reflections, overall	102,799	129,306	92,641	48,149
No. of Unique Reflections, overall	21,713	15,759	13,294	13,662
Multiplicity	4.7 (4.1)	8.2 (7.8)	7.0 (6.7)	3.6 (3.5)
R_{merge}	0.097(0.583)	0.09 (0.515)	0.079 (1.136)	0.045 (0.529)
R_{crystal}	0.19060	0.21503	0.21239	0.20627
R_{free}	0.23761	0.25520	0.25137	0.22231
Completeness %	97.4 (92.0)	99.1 (99.2)	95.9 (94.1)	99.7 (99.7)
Mean I/σ	8.2 (2.0)	12.0 (2.9)	13.8 (1.8)	16.3 (2.1)
Wilson B-factor (Å)²	23.760	27.120	45.949	35.953

3.3.4.3 Structural changes at the putative Cu(I) binding site in CsoR are pH dependent

The suggested movement of Cys104 could be observed on the crystal structure of C75A pH 5 (Figure 3.7). The movement of Cys104 also affected His103, which moved towards the back, and the absence of a sulphate ion observed at both WT CsoR and C75A pH 4 crystal structures (Figures 3.6A and 3.6C). For both C104A pH 5 and pH 6 structures (Figure 3.8), Ala104 underwent through a similar movement towards His100 as observed for Cys104 on C75A pH5 towards Cys75', which reinforces the importance of Cys104 as a potential Cu(I) binding residue. His 103 also moved towards the back and no sulfate ion was observed either at pH 5 or pH 6.

The lack of the sulfate ion on the crystal structures of C75A pH 5 and C104A (pH 5 and 6) can be explained by an ionisation event involving His103, which also affects His100 at higher pH. Although the sulfate ion forms hydrogen bonds with His100 and His103, the movement of Cys104 towards His100 is strong enough for these strong bonds to be broken. This displacement of the sulfate ion is suggested to give space for Cu(I) binding in CsoR and it may be the reason behind the non-formation of H100A or H103A crystals.

Chapter 4

Kinetics and mechanism of metal ion binding to CsoR in *S.* *lividans*

4.1 Introduction

As mentioned earlier in section 1.3.3.8, the first coordination shell sequence W-X-Y-Z fingerprint is used for sub-family characterisation within the CsoR/RcnR family in terms of metal binding. For Cu(I)-sensing CsoRs, Cu(I) is coordinated by Cys – His – Cys located at X-Y-Z positions of the fingerprint with a trigonal planar geometry (Liu *et al*, 2007; Chang *et al*, 2014). For CsoR/RcnR members as in the case of CsoR-like sulfide sensor CstR, the Cys residues at positions X and Z become sulfur derivatised instead (Lubke *et al*, 2014). For clade II *E. coli* RcnR and clade VII InrS Ni(II) sensors, the metal binding residues are His – Cys – His located at W-X-Y positions, with His and Cys at position Z respectively (Iwig *et al*, 2008; Foster *et al*, 2012; Foster *et al*, 2014b).

The presence of a His residue at position W of the fingerprint is proposed to facilitate additional ligation to high coordination number metals like Ni(II) or Co(II) in comparison with Cu(I) – Ni(II), and is suggested to coordinate with a square planar to clade VII InrS (Foster *et al*, 2012; Higgins *et al*, 2012). Within the amino acid sequence of both RcnR and InrS, the W position is predicted to be located before the start of the N-terminal α 1-helix, while for CsoRs it has a more dynamic character. In the Cu(I)-bound structure of clade IV *G. thermodenitrificans* CsoR, part of the N-terminal region is folded and lies over the Cu(I) binding site which involves residues from the X-Y-Z portion of the fingerprint located at α 2' and α 2-helices (Chang *et al*, 2014).

From all reported Cu(I)-sensing CsoRs, clade IV *B. subtilis* CsoR has been shown to be the only one able to coordinate Co(II), Zn(II) and Ni(II) *in vitro* with a non-native coordination geometry, despite the presence of a non-

coordinating metal residue (Lys) located at the W position (Ma *et al*, 2009a). *In vitro* studies showed clade IV *B. subtilis* CsoR to bind to Ni(II) with a very high affinity, however it did not drive an allosteric response (i.e. derepression or dissociation of its *copZA* operator DNA), neither did Co(II) or Zn(II) (Ma *et al*, 2009a). *T. thermophilus* CsoR was shown to bind not only Cu(I) ions, but also, Cu(II), Zn(II), Ag(I), Cd(II) and Ni(II) leading to a transcriptional repressive response of the *copZRA* operon, which also encodes CopZ and Cop A (Sakamoto *et al*, 2010). In *E. coli* RcnR, Ni(II) sensing is facilitated by changes in the coordination number from six to four (Iwig *et al*, 2008) while *Synechocystis* PCC 6803 IrnS binds also to Cu(I), Cu(II) and Zn(II) with appropriate coordination geometries to accommodate these metals and still have an allosteric response both under *in vitro* and *in vivo* conditions (Foster *et al*, 2014b). This metal binding versatility of IrnS is a strong indicative of promiscuity in its allosteric regulation mechanism in this metalloregulator that has not been observed for other CsoR/RcnR family members yet (Foster *et al*, 2014b).

Phylogenetic analysis of CsoR/RncR proteins has revealed that the Cu(I)-sensing CsoRs are distributed in four out of seven distinct clades (I, III, IV and VI) as seen on Tables 1.1a and 1.1b (Chang *et al*, 2014). Multiple sequence analysis of CsoRs within each clade indicates that the major features that distinguish the CsoRs in the different groups lie outside the X-Y-Z fingerprint motif (Figure 4.1) (Chang *et al*, 2014), thus raising the possibility that the mechanism of Cu(I)-allosteric negative regulation of DNA binding may differ between clades (Chang *et al*, 2014). For CsoR this would be the binding of Cu(I), which for this highly competitive metal is likely to occur through an

associative metal-exchange from labile metal sites present in a Cu chaperone or from the myriad components of a polydisperse buffer (Waldron *et al*, 2009; Foster *et al*, 2014a). A recent study with the clade III CsoR from *Streptomyces lividans* has demonstrated that an associative metal-exchange mechanism involving the transfer of Cu(I) from a CopZ-like metallochaperone to the CsoR can occur *in vitro* (Chaplin *et al*, 2015). From this study it was suggested, based on differences in the ionization properties of the Cys residues in the CsoR that Cys75 was initially involved in instigating the metal-exchange reaction (Chaplin *et al*, 2015). Metalloregulators in bacteria have a pivotal role in controlling metal ion concentrations to maintain under cytosolic buffering/homeostatic conditions (Waldron *et al*, 2009; Foster *et al*, 2014a). Any cytosolic fluctuations beyond these conditions trigger an initial and specific response from the appropriate metalloregulator that affects at transcriptional level.

In this chapter, kinetic studies with *S. lividans* CsoR are reported, which were conducted through stopped-flow absorbance spectroscopy for both Cu(I) and a non-cognate metal ion, in this case Ni(II) was chosen. A binding mechanism for both Cu(I) and Ni(II) ions is proposed, with the aid of site-directed Ala mutations of the putative Cu(I) binding residues at the individual X-Y-Z positions of the first coordination W-X-Y-Z fingerprint motif plus an outside mutation (H103A) of interest as mentioned in section 1.4.5. These set of experiments were conducted in order to gain further insight and understanding on how metal ion binding occurs in the CsoR/RcnR family.

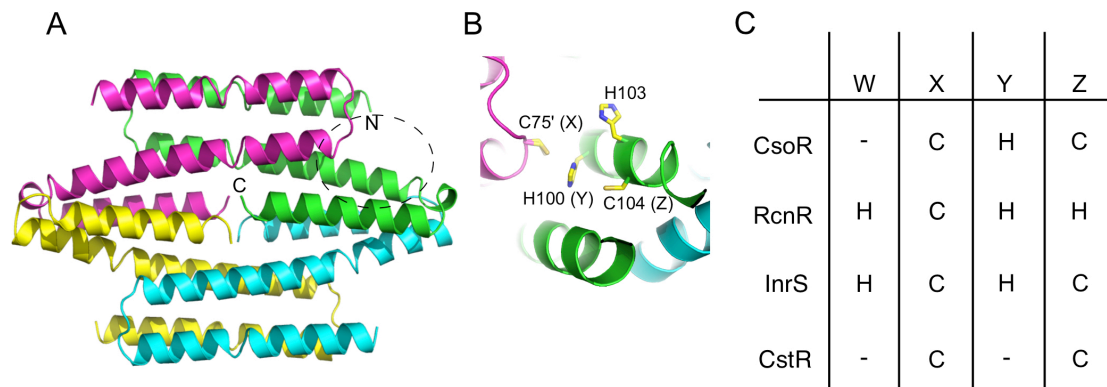


Figure 4.1 – The structural and metal binding features of *Streptomyces lividans* CsoR. A) Tetrameric assembly of the apo-form determined from crystals grown at pH 4 (Dwarakanath *et al*, 2012). Each protomer of the assembly is individually coloured and the helices of one protomer labeled. B) A close-up a Cu(I)-binding site indicated by the dashed circle in (A). In this apo-CsoR structure the Cys104 Cu(I)-ligand is too far away from the other Cu(I)-ligands, Cys75' and H100 to create a pre-formed site. The position of His103 relative to the Cu(I)-ligands is indicated. (C) Residues in the W-X-Y-Z fingerprint motif of CsoR/RcnR family members.

4.2 Material and Methods

4.2.1 Site-directed mutagenesis, over-expression and purification of *S. lividans* CsoR

WT CsoR and the C75A, H100A, H103A and C104A mutants were purified as previously described in sections 2.2.1 and 3.2.2.

4.2.2 Cu(I) sample preparation

CuCl (Sigma) was prepared in an anaerobic chamber (DW Scientific [O_2] < 2 ppm) by initially dissolving in 10 mM HCl (Fisher Scientific) and 500 mM NaCl and diluted in 10 mM MOPS (Melford), 150 mM NaCl pH 7.5. The Cu(I) working concentration was determined spectrophotometrically by step-wise addition to a known concentration of the Cu(I)-specific bidentate chelator bicinchoninic acid (BCA) (Sigma) using an ϵ at 562 nm of $7900 \text{ M}^{-1} \text{ cm}^{-1}$ for $[\text{Cu}^{\text{I}}(\text{BCA})_2]^{3-}$ (Xiao *et al*, 2008). Cu(I)-CsoR was prepared by the stoichiometric addition of CuCl in the anaerobic chamber and removed for stopped-flow studies in a gas tight syringe (Hamilton).

4.2.3 Protein preparation

Protein concentrations for all experiments were determined by UV-Vis spectroscopy (Varian Cary50 spectrophotometer) using an extinction coefficient (ϵ) for the CsoR monomer at 280 nm of $3105 \text{ M}^{-1} \text{ cm}^{-1}$.

Buffer exchange for Ni(II) experiments were aerobically carried out using a PD-10 desalting column (GE-Healthcare) pre-equilibrated in 20 mM HEPES (Melford), 50 mM NaCl, pH 7.4. For Cu(I) experiments, samples were anaerobically desalted twice using also a PD-10 column (GE-Healthcare) previously equilibrated with 10 mM MOPS, 150 mM NaCl pH 7.5 in the same anaerobic chamber from section 4.2.2. Protein samples were then anaerobically reduced overnight with 500 μ l of 5 mM DTT aqueous solution in between desalting to ensure the presence of reduced cysteines.

4.2.4 Cu(I) titrations monitored by UV-Vis absorption spectroscopy

A 1 ml sample of 40 μ M of protein in 10 mM MOPS, 150 mM NaCl pH 7.5 on a sealed 1 cm optical length quartz cuvette (Hellma) was anaerobically titrated at room temperature against 5 mM increments of the stock CuCl anaerobic solution prepared in section 4.2.2 until saturation. Titrations were monitored between wavelength ranges of 200-800 nm using a Varian Cary 50 UV-visible spectrometer.

4.2.5 Ni(II) titrations at equilibrium monitored by UV-Vis absorption spectroscopy

A 1 ml sample of 20 μ M of apo-protein in 20 mM HEPES, 50 mM NaCl, pH 7.4 on a quartz cuvette (1 cm optical length) was aerobically titrated at room temperature against 10 μ l increments of 1mM NiSO₄ (Fisher Scientific) prepared in de-ionised water in solution every minute (WT) or 2 min (H103A) until saturation. Titrations were monitored via an UV-Vis

spectroscopy in the range 200-800 nm using a Varian Cary 50 UV-visible spectrometer.

4.2.6 Electrophoretic mobility shift assay (EMSA)

DNA oligomers (Sigma) were prepared in 10 mM HEPES pH 7.5, 150 mM NaCl. Concentrations of individual oligonucleotides were determined using appropriate extinction coefficients at 260 nm on a Nanodrop2000 (Thermo Scientific). Equal concentrations of complementary strands were annealed by heating to 96 °C in a water bath for 5 min and then left to incubate to room temperature over-night. Samples for analysis by EMSA for Cu(I) experiments were all prepared in 10 mM HEPES pH 7.5, 150 mM NaCl, 1 mM DTT under anaerobic conditions and consisted of 0.5 mM of DNA duplex, 0.5 mM of DNA incubated with 4 µM WT CsoR and 0.5 mM of DNA incubated with 4 µM WT CsoR monomer followed by addition of excess Cu(I). For aerobic EMSA experiments with Ni(II), 20 µM DNA oligomer was incubated with either 10 µM or 30 µM CsoR in 10 mM HEPES pH 7.5, 150 mM NaCl followed by addition of a 2-fold excess of 10 mM NiSO₄ (also in the same buffer as protein/DNA duplex samples) for 30 minutes at room temperature. All samples were loaded (20 µl) to a pre-run 6% Tris-Borate EDTA (TBE) polyacrylamide gel (150 V for 1 hour). Gels were run (150 V for 30 minutes) and stained for 30 min in an ethidium bromide bath followed by imaging.

4.2.7 Stopped-flow spectroscopy

An Applied Photophysics SX20 stopped-flow spectrophotometer (Leatherhead, U.K.) connected to a thermostatic Peltier system at fixed

temperature of 20°C was used for all kinetic experiments. All proteins were prepared as in section 4.2.3 and later diluted in their respective buffers to give final concentrations of 20 μM (10 μM after mixing). Cu(I) and Ni(II) were mixed with the respective protein in the concentration ranges (after mixing) of 34 μM -137 μM and 50 μM - 800 μM , respectively. For the Cu(I) binding experiments and displacement studies anaerobic conditions were employed at all times whenever possible, including washing the mixing compartment of the stopped-flow spectrophotometer with degased buffer through its drive syringes. This was achieved by degasing both buffer and NiSO₄ solutions with argon.

For the Cu(I) kinetics, time courses were taken at 250 nm with various Cu(I) concentrations and the transients were best fitted using a triple exponential function. For Ni(II) binding kinetics time courses were taken at 300 nm and 350 nm with various Ni(II) concentrations and the transients fitted to a double and single exponential function, respectively. A point to point accumulation was carried out for Ni(II) binding to WT CsoR between 330-420 nm with a step of 5 nm using 20 mM of protein and 200 mM of Ni(II) before mixing. The rate constants reported are an average of triplicate experiments carried out on different days and with different protein batches with the errors reported being the standard deviation between the data sets.

4.3 Results and Discussion

4.3.1 Cu(I) Binding to CsoR mutants H103A and C104A

Upon the addition of anaerobic Cu(I) to H103A, a metal-dependent feature at 240 nm was generated which could be then assigned to the Cu(I) binding peak. The UV-Vis difference spectrum of H103A was very similar to WT CsoR (Dwarakanath *et al*, 2012). The binding isotherm at 240 nm was also similar to WT CsoR overall with a saturation point at 1:1 [Cu(I)]/[H103A] ratio (Figure 4.2). In the case of C104A UV-Vis difference spectrum, the absorbance values at 240 nm were reduced and the binding isotherm indicated a saturation point at 0.5 [Cu(I)]/[C104A] ratio, a reduction of 50% in comparison with wild-type CsoR (Figure 4.3). The results above suggested His103 is not a Cu(I) binding residue unlike Cys104, the latter being at position Z of the X-Y-Z fingerprint motif.

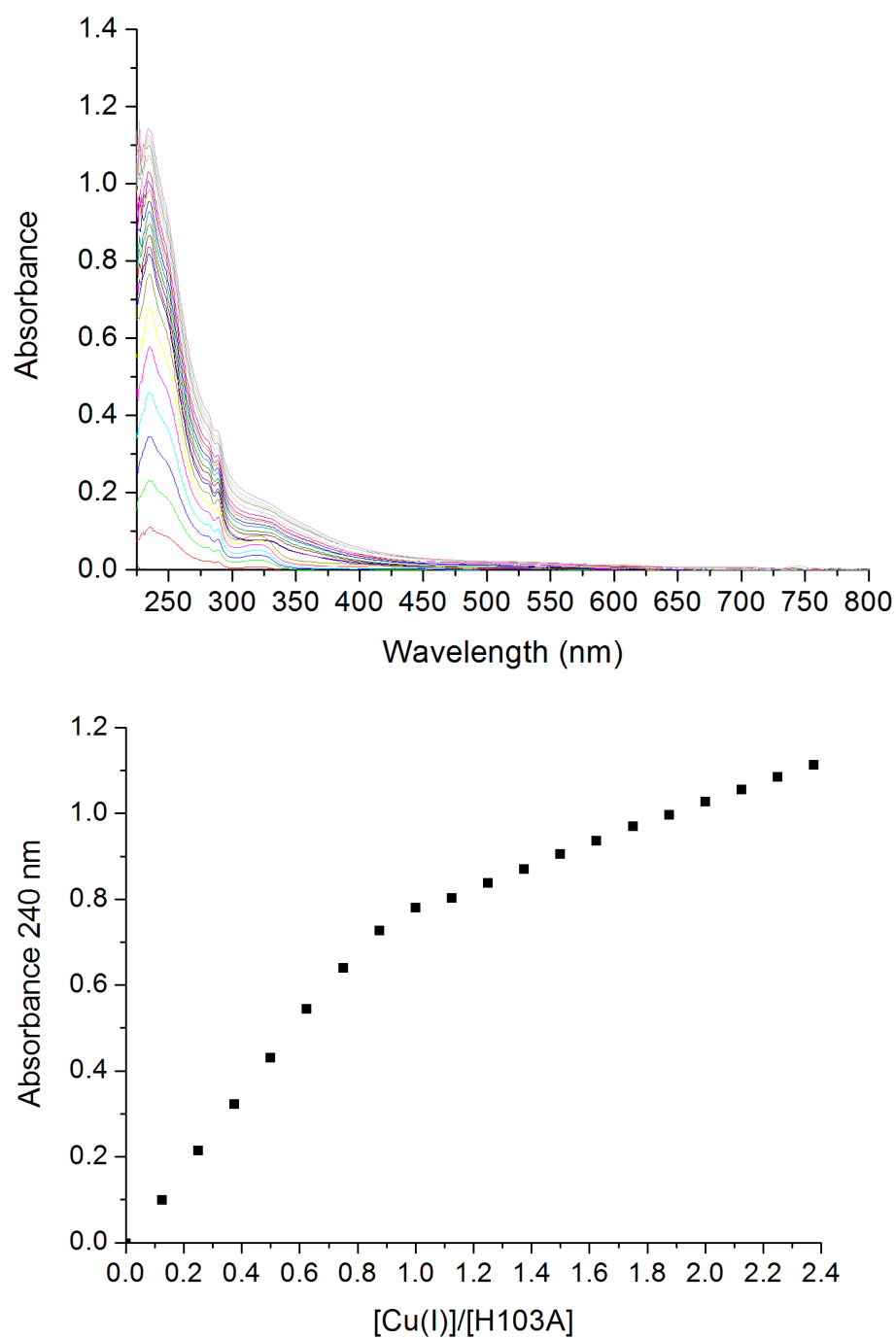


Figure 4.2 – Anaerobic UV-Vis absorption difference spectrum (top) and binding isotherm (bottom) at 240 nm of 36 μ M H103A mutant upon step-wise addition of 5 μ M CuCl (pH 7.5 and 20 $^{\circ}$ C). Changes were observed in the UV region, with a distinct increase in absorption at 240 nm.

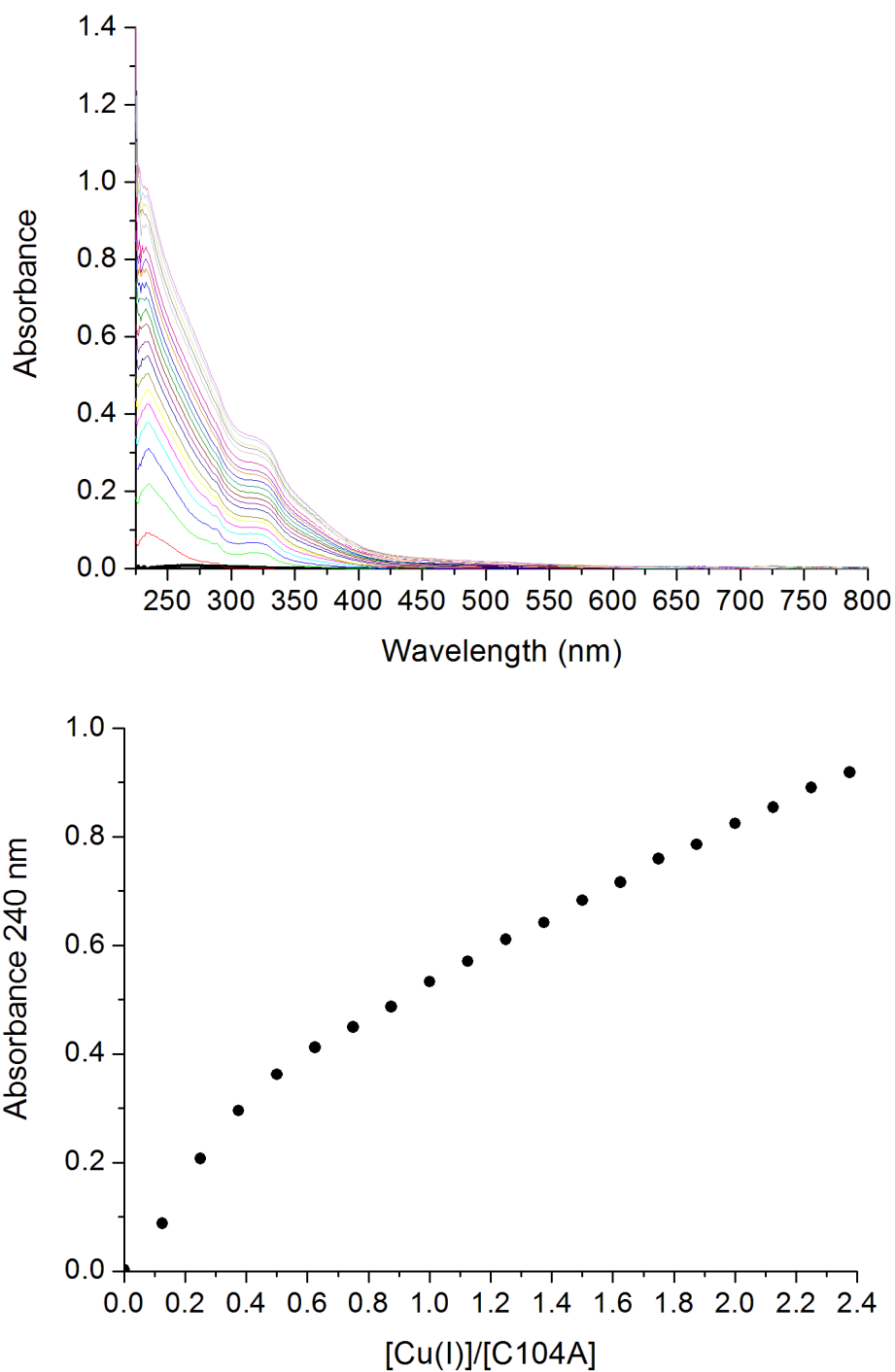


Figure 4.3 – Anaerobic UV-Vis absorption difference spectrum (top) and binding isotherm (bottom) at 240 nm of 40 μ M C103A mutant upon step-wise addition of 5 μ M CuCl (pH 7.5 and 20 $^{\circ}$ C). Changes were observed in the UV region, with a distinct increase in absorption at 240 nm.

4.3.2 Cu(I) binding kinetics to *S. lividans* CsoR and mutants

Stopped-flow kinetic studies under anaerobic conditions of Cu(I) binding to WT CsoR were monitored at 250 nm. Representative time courses with increasing Cu(I) concentrations are illustrated in Figure 4.4A. A very rapid phase occupying the first 5-10 ms after mixing is followed by a slower phase taking around 1 s to complete (Figure 4.4A). The time courses, however, were best fitted to a three component exponential function to give rate constants for a fast ($k_{1\text{Cu}}$), and two slower phases ($k_{2\text{Cu}}$ and $k_{3\text{Cu}}$), with the third phase comprising less than 10 % of the total amplitude change at 250 nm. For all phases the pseudo first-order rate constants were independent of [Cu(I)] between 5 and 100 μM of Cu(I) with the average across the concentration range reported in Table 4.1. The total amplitude change for the transition as a function of [Cu(I)]/[CsoR monomer] reveals a linear relationship until a break point is reached at a stoichiometry of $\sim 1:1$, indicative of a high affinity Cu(I) binding process (Figure 4.4B). This stoichiometry is consistent with previously reported titration experiments, where changes in the absorption spectrum at 240 nm, indicative of Cu(I)-thiolate bond formation was monitored (Dwarakanath *et al*, 2012).

The kinetics of Cu(I) binding to the H103A mutant and the X-Y-Z fingerprint mutants were next investigated. His103 is relatively well conserved amongst clade III and IV Cu(I)-CsoR members and is located between the Y (His100) and Z (Cys104) fingerprint residues. Structural data has revealed that in the apo-form of *S. lividans* CsoR the imidazole ring of His103 lies in an orientation that together with His100 and Cys75' could conceivably lead to participation in metal ion coordination (Dwarakanath *et al*, 2012) (Figure

4.1B). Stopped-flow experiments with the H103A mutant gave essentially identical Cu(I) concentration independent rates (Table 4.1), total amplitude change and stoichiometry of Cu(I) binding as WT CsoR. This implies that His103 is not involved in the Cu(I) binding process being observed. However, differences are apparent for the X-Y-Z fingerprint mutants. For C75A the rate constants remain the same as WT (Table 4.1), but the concentration of Cu(I) required to reach full saturation (i.e. to give the same amplitude change as observed for WT CsoR) increases (Figure 4.4). This finding suggest a weaker affinity for Cu(I) when Cys 75 is absent. For the other Cys mutant, C104A, the kinetics and rate constants are largely unaffected (Table 4.1). But in comparison with WT CsoR, the total amplitude change for C104A is not at ~35% despite a 1:1 stoichiometric binding ratio being present. With the H100A mutant, the total amplitude change at Cu(I) saturation also decreases, but to ~60% of what was observed for WT CsoR and a 1:1 stoichiometric binding ratio being maintained (Table 4.1). Therefore the H100 and C104 residues of the X-Y-Z motif are seemingly important to develop the full absorbance change at 250 nm on Cu(I) binding. These data along with that of wild-type suggest the observed kinetic phases are not reporting on the initial binding of Cu(I) due to the absence of a [Cu(I)] dependence on the rate constants. Instead a post binding event is likely being monitored that may be caused by a rearrangement of the metal binding site once Cu(I) is bound. Initial binding must therefore be optically silent and must be faster than the rates of the fastest process with a second order binding constant $> 10^7 \text{ M}^{-1}\text{s}^{-1}$.

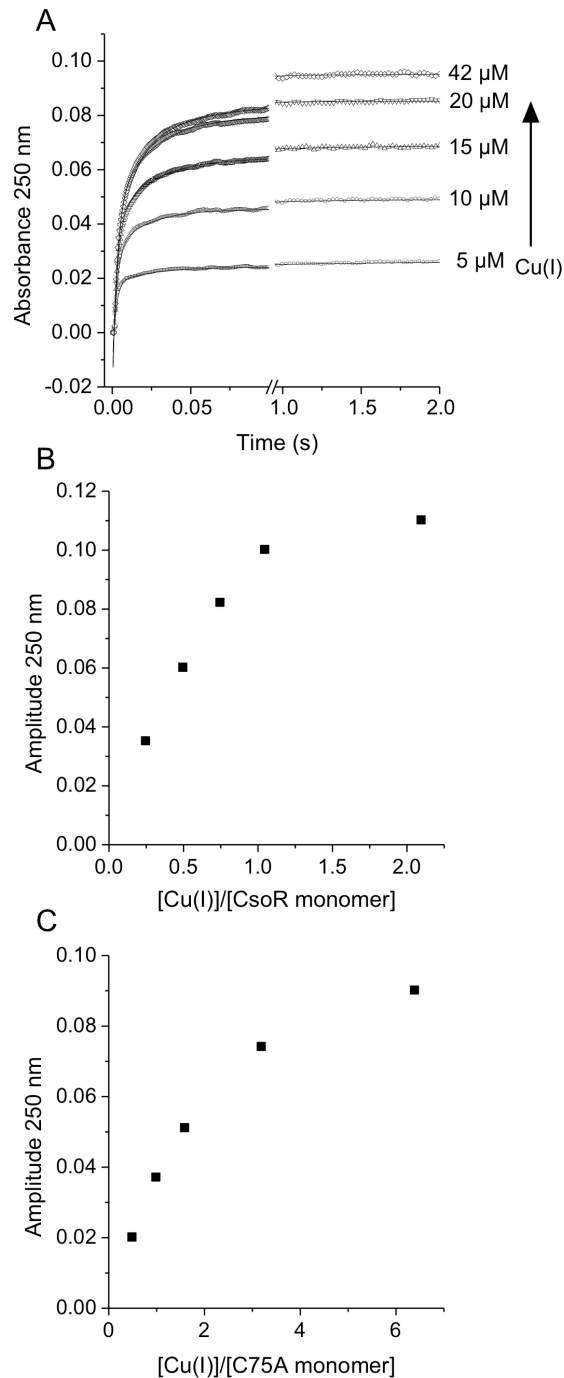


Figure 4.4 - Stopped-flow kinetics of Cu(I) binding to *S. lividans* CsoR. A) Representative time courses monitored at 250 nm for WT CsoR at increasing Cu(I) concentrations. Fits to the data points are indicated with the solid line. The break in the x-axis at 0.1 s enables for the end point absorbance to be observed. Total amplitude change at 250 nm derived from the kinetic data plotted as a function of the [Cu(I)]/[CsoR monomer] for WT CsoR (B) and the C75A fingerprint mutant (C).

Table 4.1 - Stopped-flow determined average pseudo first-order rate constants and amplitude change at 250 nm ($\Delta\epsilon$) for Cu(I) binding to *S. lividans* CsoR (10 μ M) and mutants (20 $^{\circ}$ C, pH 7.4). The Cu(I) concentrations used were between 34 - 137 μ M. Standard errors are given in parenthesis.

CsoR Protein	k_{1Cu} (s^{-1})	k_{2Cu} (s^{-1})	k_{3Cu} (s^{-1})	$(\Delta\epsilon)$ $M^{-1}cm^{-1}$
WT	312.6 (15.3)	38.7 (4.0)	2.3 (0.6)	10^4
H103A	312.8 (15.7)	53.2 (8.8)	4.4 (1.4)	1.1×10^4
C75A	320.6 (40.5)	62.4 (10.0)	9.8 (3.7)	9×10^3
H100A	249.4 (32.0)	22.8 (4.4)	1.3 (0.4)	6×10^3
C104A	367.6 (40.0)	35.3 (4.5)	2.5 (0.71)	3.5×10^3

4.3.3 Ni(II) binding to *S. lividans* CsoR and mutants

Upon addition of Ni(II) to WT CsoR, metal-dependent features at 275 nm and 340 nm in the UV-Vis difference absorption spectrum were generated (Figure 4.5A), which were reminiscent of the spectra for *B. subtilis* Ni(II)-CsoR (Ma *et al*, 2009a) and Ni(II)-InrS (Foster *et al*, 2012). In *B. subtilis* Ni(II)-CsoR and Ni(II)-InrS, the bands at 333 nm and 340 nm were assigned as ligand to metal charge transfers (LMCT) as a result of the formation of Ni(II)-thiolate bounds (Ma *et al*, 2009a; Foster *et al*, 2012). The binding isotherms of *B. subtilis* Ni(II)-CsoR and Ni(II)-InrS at their maximum absorbance peaks 333 nm against $[\text{Ni(II)}]/[\text{InrS}]$ and 340 nm against $[\text{Ni(II)}]$ alone indicated a saturation point at 1 equivalent of Ni(II), which is an evidence of a high affinity binding process (Ma *et al*, 2009a; Foster *et al*, 2012). For *S. lividans* CsoR, the shape for the binding isotherm at 340 nm (Figure 4.5A, inset) indicated that it did not saturate at 1 equivalent of Ni(II). An initial and possible explanation was of that it might be related to a cooperativity event, due to the structural nature of *S. lividans* CsoR as homotetramer. However, it was ruled out based on the calculation of a Hill coefficient of > 4 for a sigmoidal fit to the data. A more suitable and alternative explanation suggests the existence of at least two Ni(II) binding sites with different affinities and optical properties. A very weak transition at approximately 480 nm was observed at the saturation point in the wild-type UV-visible spectrum. Similar bands at this spectral region were observed in both *B. subtilis* Ni(II)-CsoR and Ni(II)-InrS spectra and attributed to d-d transitions due to Ni(II) to be coordinated in a square planar or distorted tetrahedral geometry (Ma *et al*, 2009a; Foster *et al*, 2012).

From the site-directed Ala mutants, the UV-Vis difference absorption spectrum of H103A upon [Ni(II)] addition is identical to wild-type CsoR (data not shown). However, the binding isotherm at 340 nm was less complex in comparison to the WT CsoR. On the other hand, the band at 340 nm was very weak in all the X-Y-Z fingerprint mutants (C75A, H100A and C104A) in the presence of saturating Ni(II). This observation illustrated the sensitivity of the proposed Ni(II)-thiolate LMCT band at 340 nm to be beyond the Cys residues at the X and Z positions, but also to the coordinating residue at the Y position of the X-Y-Z portion of the fingerprint as supported by the spectrum of H100A (Figure 4.5B). For *B. subtilis* Ni(II)-CsoR and Ni(II)-InrS, a histidine residue is also localized at the Y position (Ma *et al*, 2009a; Foster *et al*, 2012).

The allosteric response of WT CsoR in the presence of Ni(II) was investigated through EMSA experiments. Binding of Ni(II) to WT CsoR pre-incubated with *csoR* operator DNA does not induce the allosteric response observed with Cu(I) (Figure 4.5C). A similar response was previously reported in *B. subtilis* CsoR (Ma *et al*, 2009a) and reinforced the importance of cognate metal coordination geometry to the allosteric response in Cu(I)-CsoR members.

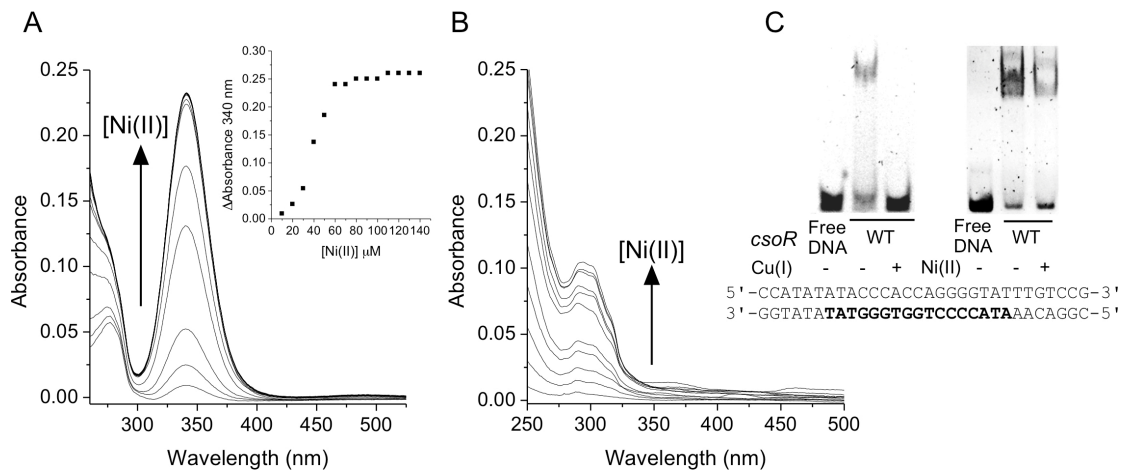


Figure 4.5 - Spectroscopic and regulatory properties of Ni(II) binding to *S. lividans* CsoR. A) Changes in the apo-CsoR base-lined absorption spectra (20 mM CsoR monomer) of A) WT CsoR and B) the H100A fingerprint mutant upon increasing Ni(II) concentration. The inset in (A) reports the binding isotherm generated from the Δ Abs at 340 nm as a function of Ni(II) concentration. C) EMSA of WT CsoR and the *csoR* operator DNA sequence in the presence and absence of either Cu(I) and Ni(II).

4.3.4 The kinetics of Ni(II) binding to WT CsoR and mutants

From a initial wavelength scan around the 340 nm peak observed at the static titrations (Figure 4.5A) on section 4.4.3 using a diode array detector, upon rapid mixing of excess Ni(II) in the stopped flow, time courses at different wavelengths were generated (Figure 4.6B). Maximum absorbance change was observed at 350 nm and also confirmed an increase of absorbance (Figure 4.6A) at a crescent timescale. These observations are consistent with the observation at 340 nm, with the 10 nm offset due to the settings applied. The time courses monitored around the 340 nm region (Figure 4.6B) indicated a short "lag phase" that occupied the first few seconds due to dead time of the equipment. Despite this observation, data (> 90 % of the total amplitude change) was then well fitted to a single exponential curve. Singular value decomposition (SVD) of the data indicated that no spectral distinct intermediates occurred in this process.

Ni(II) concentration dependence was further investigated by using total amplitude change and binding rate constants as parameters. At 350 nm, no [Ni(II)] dependence was observed over the concentration used (20-800 μ M) on the rate (k_{Ni}), implying that, at the time of the first observation, Ni(II) is already bound (Table 4.2). Ni(II) binding to CsoR was not stoichiometric according to the total amplitude change plotted as a function of [Ni(II)]/[CsoR monomer] consistent with the static titration (data not shown). Based on the initial wavelength scan in the diode array, an attempt to observe the initial binding phase the UV-region of the spectrum was explored, this time with the aid of a photomultiplier detector. A distinct faster process

was found to occur at 300 nm, subsequently followed by a slow phase (Figure 4.6C). Rate constants for the fast (k_{1Ni}) and slow phase (k_{2Ni}) for the process at 300 nm were obtained (Figure 4.6C and Table 4.2), with k_{2Ni} essentially equal to k_{Ni} determined for the formation of the 350 nm band (Table 2). In figure 3.6C, both time courses at 300 nm and 350 nm were presented under the same time scale. The lag-phase at 350 nm is more easily discerned within and was seen to occupy the duration of the time taken to complete the fast phase stage at 300 nm, implying that a sequential mechanism of Ni(II) binding is being observed. The rate constant for the fast process at 300 nm was also independent of $[Ni(II)]$, as an indication that the second order binding of Ni(II) to WT CsoR occurred more rapidly and without a spectroscopic signature within this particular spectral range.

However, once Ni(II) (a non-cognate metal to *S. lividans* CsoR) was bound, Ni(II) underwent through a rearrangement to form the final Ni(II)-CsoR complex with rates that were > 500 times slower than for Cu(I), as its cognate metal. Using the set of site-directed X-Y-Z fingerprint alanine mutants and H103A, the kinetics of Ni(II) binding were further investigated with more detail. The fast phase for the C104A mutant was essentially unperturbed at 300 nm (k_{1Ni}) (Figure 4.7A and Table 4.2). However, the slower phase (k_{2Ni}) is no longer detected as may have been expected based on the very small absorbance increase at 340 nm in the static spectrum with saturating $[Ni(II)]$. A relevant contrast was observed for the C75A mutant, on which both the fast phase at 300 nm and the slower 350 nm phase (Figure 4.7B) were abolished and this was also the case for the H100A (data not shown). The fast phase was also lost for the non-X-Y-Z fingerprint mutant H103A at 300 nm (Figure

4.7C) with the absorbance at 300 nm now showing a simple increase with the rate constant, k_{2Ni} , similar to that for the formation of the 350 nm band (Table 4.2). This evidence strongly suggested that His103 is a residue that is involved in the mechanism of Ni(II) binding.

Table 4.2 - Stopped-flow determined average pseudo first-order rates constants for Ni(II) binding to *S. lividans* CsoR (10 μ M) and variants (20 °C, pH 7.4). The Ni(II) concentrations used were between 50 - 800 μ M. Standard errors are given in parenthesis.

CsoR^a Protein	k_{Ni} 350 nm (s^{-1})	k_{1Ni} 300 nm (s^{-1})	k_{2Ni} 300 nm (s^{-1})
WT	0.072 (0.006)	0.65 (0.04)	0.10 (0.02)
H103A	0.083 (0.02)	-	0.09 (0.02)
C104A	-	0.97 (0.12)	-

^aNo rates were determined for the C75A and H100A variants as no spectral change was observed for.

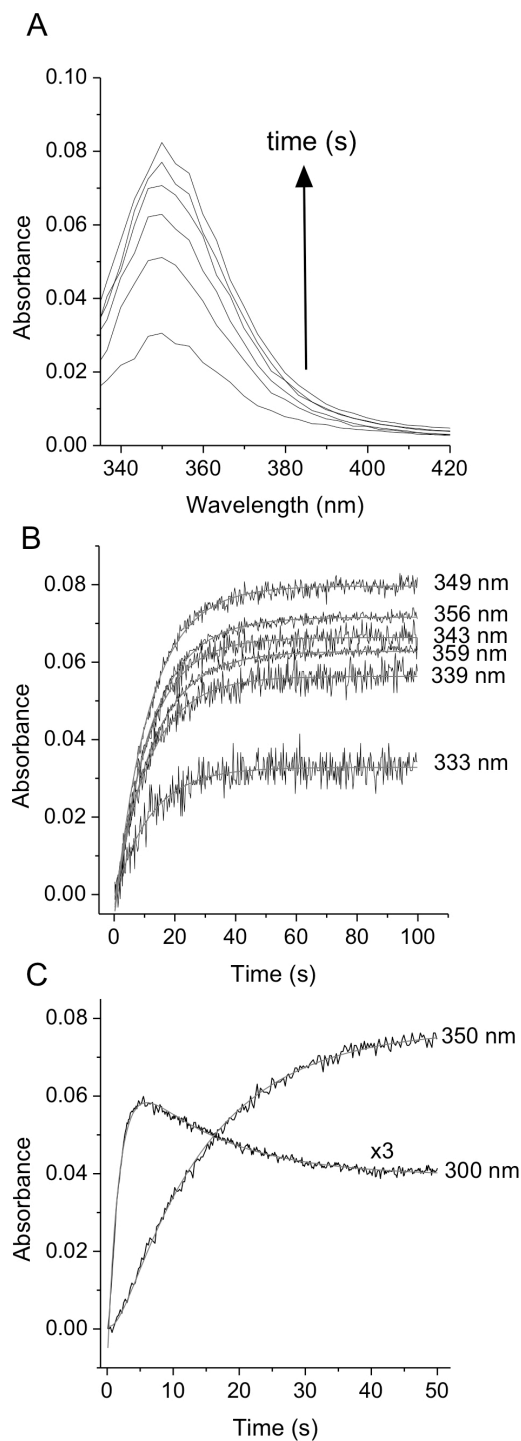


Figure 4.6 - Stopped-flow kinetics of Ni(II) binding to *S. lividans* WT CsoR. A) Spectra constructed at the following times, 6.5, 13, 18.5, 25, 35, 98 s, after mixing from the time courses at the indicated wavelengths shown in B) on reacting 20 mM of CsoR with 200 μ M of Ni(II). The solid lines in (B) represent a monophasic fit to the data excluding the initial 5 s as discussed in the main text. C) Overlay of representative time courses collected at 300 and 350 nm with the solid line a fit to a double exponential function to give $k_{1Ni} = 0.56 \text{ s}^{-1}$ and $k_{2Ni} = 0.074 \text{ s}^{-1}$.

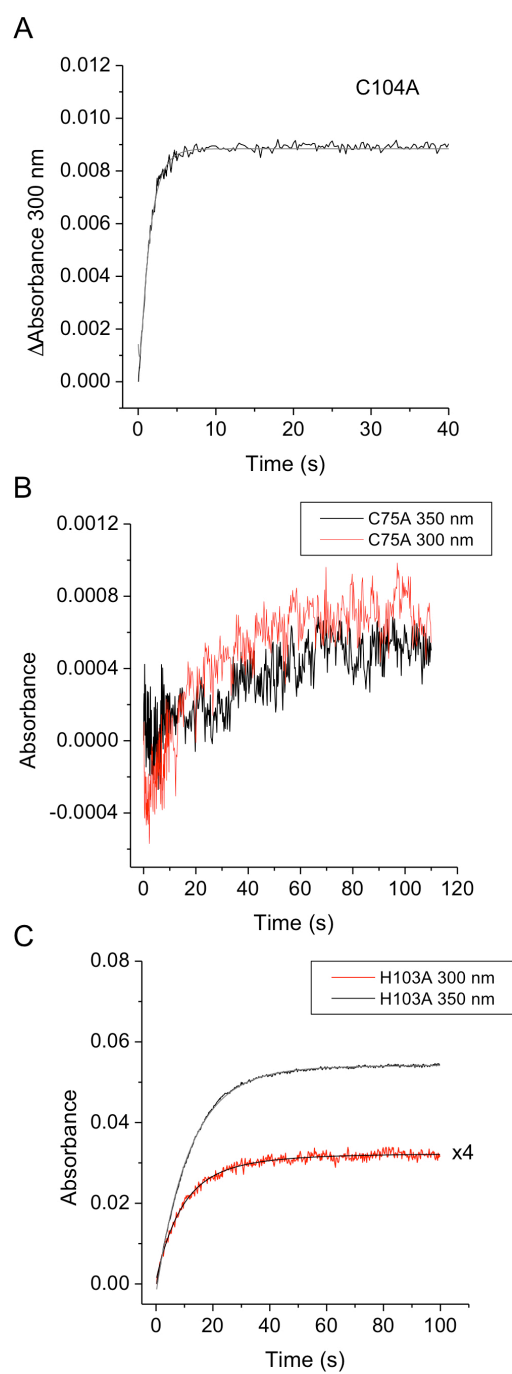


Figure 4.7 - Stopped-flow kinetics of Ni(II) binding to *S. lividans* CsoR mutants. Representative time courses for A) C104A monitored at 300 nm, 100 mM Ni(II) B) C75A, 800 mM Ni(II) and C) H103A, 100 mM Ni(II). The solid lines through the time course data for the C104A and H103A mutants are the fits to a single exponential function.

4.3.5 Metal displacement studies of *S. lividans* CsoR

In the absence of cellular control mechanisms to regulate metallation, i.e., when a metal ion binds to an organic molecule as in the case of a protein), a metallo-protein or -enzyme will select a divalent metal ion with a ranked order of preference that follows the Irving-Williams series as mentioned in section 1.3.1 (Coyne and Giedroc, 2013). Therefore the most competitive divalent metal ions will occupy the metal binding site(s), occluding weaker binding ions. In this respect Cu(II) will outcompete Ni(II) based on their respective positions in the Irving-Williams series, and this is thought to be also the case for Cu(I). An important issue to be resolved in this study and to gain further mechanistic insight into metal ion binding to this CsoR, is to confirm that Cu(I) and Ni(II) occupy the same binding site. To address this the kinetics of metal ion displacement were monitored. Cu(I)-loaded CsoR was mixed under anaerobic conditions in the stopped-flow with up to 31 μ M of Ni(II). No spectral changes (i.e. formation of a 350 nm band) assigned to Ni(II) binding were observed, indicating that Cu(I) is occupying the site where Ni(II) binds and is not displaced on addition of Ni(II). This finding is thus in keeping with their respective positions in the Irving-Williams series (Coyne and Giedroc, 2013). The reverse displacement experiments, whereby the protein is largely occupied by Ni(II) (2 Ni(II): 1 CsoR monomer) and the 350 nm band is developed was then mixed in the stopper-flow with excess Cu(I) ([Cu(I)] = 120 mM). This resulted in the bleaching of the 350 nm band in which the time course can be fitted to a triple exponential function (Figure 4.8) to give the rates reported in Table 4.3. These were assigned to the sequential displacement of Ni(II) from its ligand set and the subsequent substitution by

Cu(I). Concomitantly, absorbance changes monitored at 250 nm (i.e. binding of Cu(I)) showed a small fast phase (assigned to a small fraction of a Ni(II) free protein) and two phases with rates close to the k_1 and k_2 rates seen at 350 nm (Table 4.3), confirming the displacement of Ni(II) from ligation at the same site as Cu(I) is binding. On mixing wild-type CsoR with a single Ni(II) equivalent bound (300 nm band developed but little 350 nm absorbance developed) with excess Cu(I) resulted in the rates for the transition at 250 nm being essentially as observed in the absence of Ni(II) (Table 4.3). These data together with the earlier kinetic and static experiments support the notion that Ni(II) has two binding sites; one that has identical amino acid coordination as the Cu(I) binding site and the second involving His103, a residue not involved in the mechanism of Cu(I) binding. His103 has been identified above as being important for the formation of the fast phase at 300 nm and its absence changes the mechanism of Ni(II) binding. Stoichiometric addition of Ni(II) to the H103A mutant is sufficient to give almost full absorbance of the 350 nm band compared to the wild-type, which upon mixing with excess Cu(I) perturbed the kinetics in a similar manner as observed when two equivalents of Ni(II) were loaded to the WT CsoR; i.e. the rate constants obtained from a triple exponential fit for the bleaching of the 350 nm band were very similar to those for the formation of the 250 nm band (Figure 4.9 and Table 4.3).

Table 4.3 - Stopped-flow determined pseudo first-order rate constants for the displacement of Ni(II) from WT CsoR and the H103A mutant of *S. lividans* CsoR with Cu(I) (20 °C, pH 7.4). Standard errors are given in parenthesis.

Reaction	Bleaching of 350 nm band			Formation of 250 nm band		
	Rate constants (s ⁻¹)			Rate constants (s ⁻¹)		
	k ₁	k ₂	k ₃	k ₁	k ₂	k ₃
2 Ni(II)-WT CsoR + Cu(I)	90.9 (8.0)	3.5 (0.5)	0.6 (0.02)	553 (156)	66 (10.7)	10 (2.3)
1 Ni(II)-WT CsoR + Cu(I)^a	-	-	-	391 (85)	25.4 (8.3)	-
1 Ni(II)-H103A + Cu(I)	62 (12)	7.9 (1.5)	1.14 (0.52)	89 (15)	7.3 (2.3)	0.8 (0.1)

^aAt 1 equivalent of Ni(II) the 350 nm band is not formed and the formation of the 250 nm band fitted adequately to a double exponential.

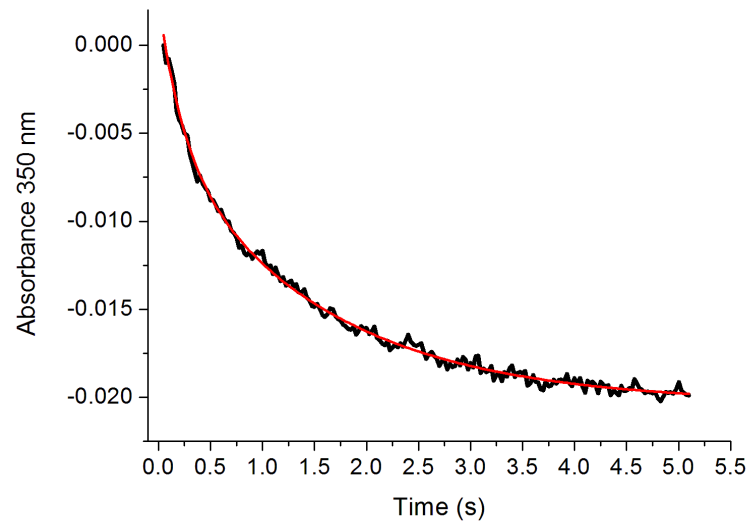
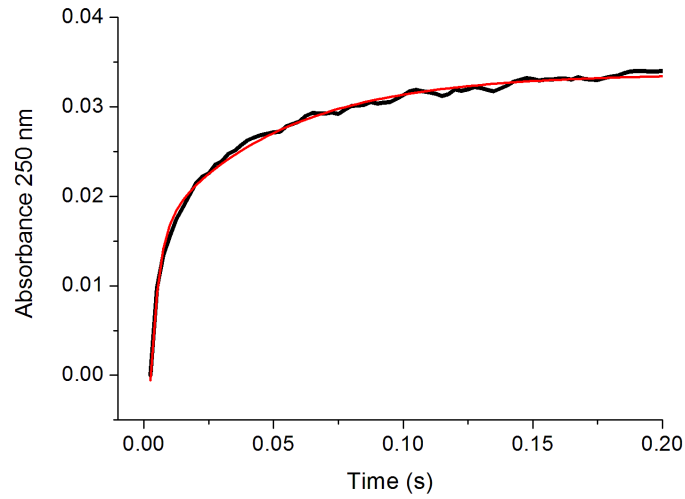


Figure 4.8 - Displacement studies for *S. lividans* CsoR. Representative time courses at 250 nm (top) and 350 nm (bottom) with 31 μM Ni(II) and 120 μM Cu(I) after mixing. The red lines through the time course data in black are the fits to a triple exponential function.

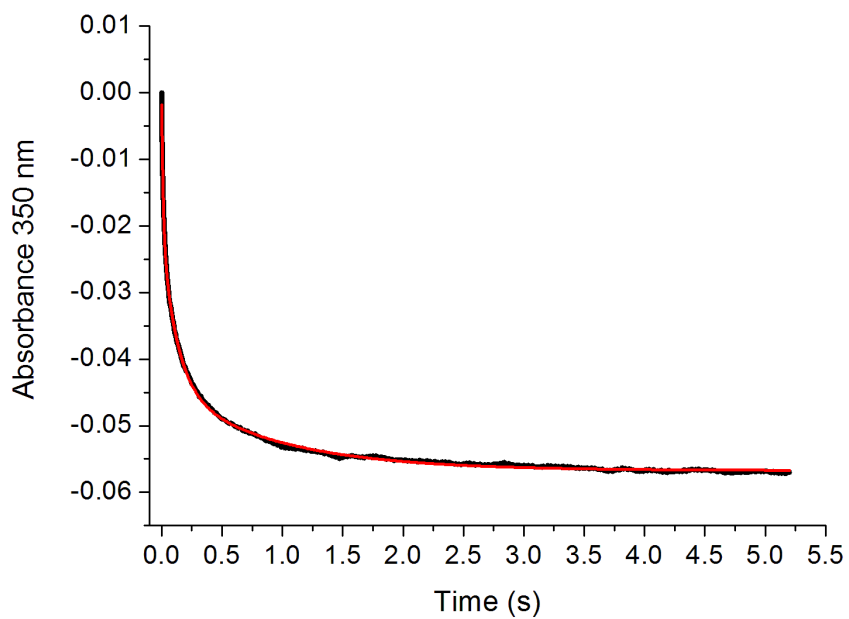
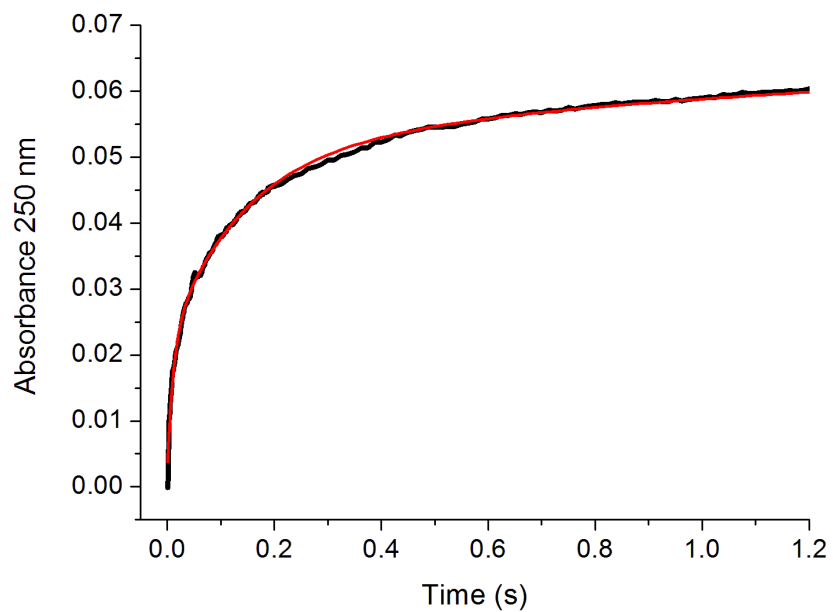


Figure 4.9 - Displacement studies for *S. lividans* CsoR mutant H103A. Representative time courses at 250 nm (top) and 350 nm (bottom) with 31 μM Ni(II) and 120 μM Cu(I) after mixing. The red lines through the time course data in black are the fits to a triple exponential function.

4.3.6 Mechanism of Cu(I) and Ni(II) binding to *S. lividans* CsoR

Within the framework of the kinetic and static spectroscopic data presented above, a mechanism which can provide a consistent picture for both Ni(II) and Cu(I) binding to *S. lividans* CsoR is depicted in the scheme presented in Figure 4.10.

To account for the absence of a step, the rate of which is either [Cu(I)] or [Ni(II)] dependent, it is proposed that the metal ion binds rapidly to species (A) to form species (B), a complex that is spectroscopically silent in the spectral range monitored. Based on known metal-ligand preferences and supported by the spectroscopic data it is suggested that Ni(II) binds initially to His103; Ni(II) is known to have a strong affinity with the imidazole side chain of histidine. Similarly, it is feasible that Cu(I) favours a Cys residue. This could be Cys75 as this makes a relatively small absorbance contribution in so far as the full absorbance change at 250 nm is observed in its absence (Table 4.1) and also based on it being predominately in the thiolate form at pH 7.4 (Chaplin *et al*, 2015). However, this explanation is not favoured, as this is not consistent with displacement studies (section 4.4.5) and therefore it is suggested that initial Cu(I) binding occurs at a site with ligands other than those depicted in species (A).

The Ni(II)-adduct formed in species (B) rearranges to form species (C) whereby the His103 ligation remains intact and further ligation by way of Cys75' and His100 occurs, which gives rise to the absorbance at 300 nm. Species (C) rearranges such that His103 is displaced from coordination and Cys104 takes its place to form species (D). This reorganization is driven by binding a second Ni(II) to the freed His103, thus accounting for the non-

stoichiometric binding observed in the static titration and the full formation of the 340 nm band. The rate constant (k_{2Ni}) for the transition between species (C) and (D) (Table 4.2), is most simply interpreted as the rate of His103 dissociation. To account for the observation of the weak absorption transition at 480 nm, an unknown ligand, L, is included, to give a favoured square planar Ni(II) geometry in the final Ni(II)-complex. The ligand switching between His103 and Cys104 determined through kinetic analysis is fully consistent with recent structural data from Chapter 2 on the 'quasi Cu(I) bound' state of *S. lividans* CsoR, whereby conformational switching between the apo- and 'quasi Cu(I)-bound' states causes the Cys104 to move into the Cu(I) coordination sphere and the His103 to move out.

Whereas His103 plays a key role in the mechanism of Ni(II) binding it appears to have no role in Cu(I) binding, as supported by both static titration data and stopped-flow spectroscopy experiments. Rather the encounter complex, species (B), with unknown Cu(I) coordination is rapidly transformed to species (E) in which Cu(I) coordinates to Cys104, the Cys residue that provides the most contribution to the absorbance at 250 nm (Table 4.1). Thereafter, rearrangement of the Cu(I) coordinated Cys104 brings the metal into full coordination leading to the final Cu(I) complex species (F). Species (F) and (D) both utilize the X-Y-Z fingerprint to bind the respective metal ion, thus the high affinity cognate Cu(I) once bound, cannot be displaced by Ni(II) (over the concentration explored in our experiments), whereas the Ni(II) may be displaced readily from this site by Cu(I) (species (H)) at rates we assign to Ni(II) dissociation from the X-Y-Z ligand set. This mechanism of Cu(I) binding is supported by the Ni(II) displacement studies from species (C) i.e. when a

stoichiometric Ni(II) is bound, in which the initial phases of Cu(I) binding at 250 nm are unperturbed by Ni(II) as expected for a model where Cys104 remains free in species (C). This leads to the formation of species (G) which converts into species (H) in which the Cu(I) occupies its normal binding site and the Ni(II) may remain coordinated to the His103.

Although not determined here, there is a possibility that on binding Ni(II) to His103 the highly conserved N-terminal tail residue His37 may participate. Structural evidence indicates this tail to be dynamic in the apo-state of CsoR members (Dwarakanath *et al*, 2012; Coyne and Giedroc, 2013; Chang *et al*, 2014) but has recently been shown that upon binding Cu(I) this region becomes folded and lies over the Cu(I) binding site (Chang *et al*, 2014a). It may therefore be conceivable that for Ni(II) binding, the tail may assist in the formation of the initial spectroscopically silent encounter complex (species (B)) enhancing the stabilization of this Ni(II)-adduct and also in species (D).

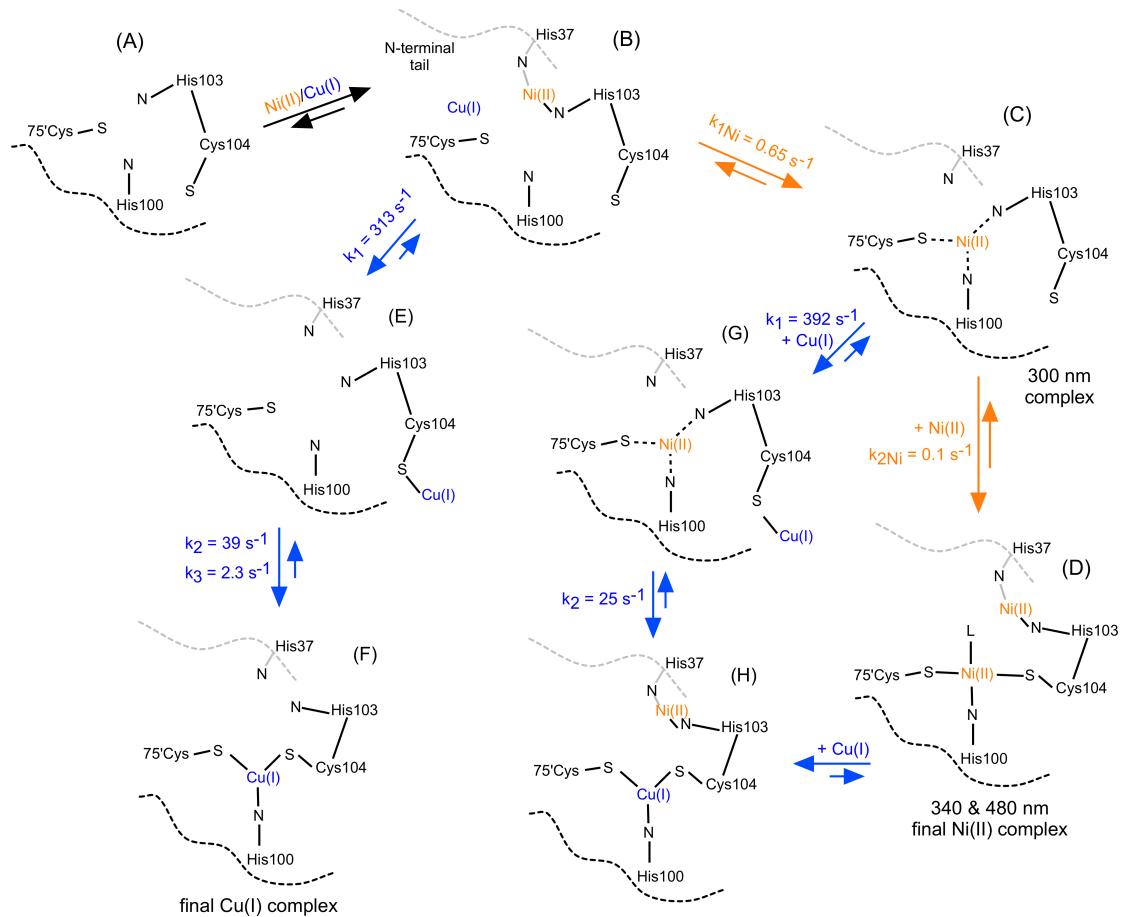


Figure 4.10 - Mechanism of Cu(I) and Ni(II) binding to *S. lividans* CsoR. The possibility of a role for the N-terminal tail residue His37 in Ni(II) binding as discussed in the text is indicated in grey. L is an unknown ligand.

Chapter 5

Major Conclusions

5.1 Concluding Remarks and Future Perspectives

The importance of a well-buffered metal homeostatic system in bacteria is of an underestimated value for metalloprotein research. In this thesis, further understanding of the mechanism of action of *S. lividans* CsoR were investigated through a structural and kinetic point of view, with two major findings.

In Chapter 2, together with the previously reported apo structure at pH 4 (Dwarakanath *et al*, 2012) the new apo structure at pH 6 and its quasi Cu(I)-bound state indicates that *S. lividans* CsoR can access different conformational states in crystals grown at different pH values. This work proposes that both states observed in the respective crystals are accessible in solution and are selected through either DNA or Cu(I) binding. Structurally speaking, the apo-state at pH 4 has conformational features that are tuned to enable binding to the operator DNA in its A-conformation to be stabilised, whereas upon binding Cu(I), the pH 6 conformer is favoured and dissociation occurs due to this Cu(I)-CsoR rigid state. From the crystal structures of the CsoR mutants discussed in Chapter 3, the kink or bulge observed at $\alpha 2$ helix was present at higher pH for C75A and both C104A pH 5 and pH 6 structures, reinforcing the role of pH in *S. lividans* CsoR.

The combination of physical and chemical properties is crucial to understand protein function, and in the case of *S. lividans* CsoR is no different. Changes in conformation and the different distribution of surface charge are considered to no longer be optimal for the tetrameric face to keep the bound DNA in the A-conformer. This latter observation highlights the importance of comparing different structural states between the same

species. Currently only two Cu(I)-bound structures from CsoR/RcnR members have been reported, clade I *M. tuberculosis* CsoR and clade IV *G. thermodenitrificans* CsoR. These structures were crystallised at pH 7.5 (Liu *et al*, 2007) and pH 7 (Chang *et al*, 2014) respectively, at a pH range similar to physiological conditions and may be in a similar conformational state as found *in vivo*. Finally, this work indicates that allostery in these disc-shaped tetrameric CsoR proteins, which possess no recognisable DNA binding domain as observed in other metalloregulator families (winged helix or ribbon-helix-helix), is controlled through rather modest structural perturbations that serve to regulate charge distribution over the tetrameric DNA binding face.

In the other major metalloregulator families, the N-terminal region constitutes part of the DNA binding region whereas the metal binding is located at the C-terminal, which is the case of NikR and CueR in *E. coli*. Despite the absence of protein-DNA complex structure for any CsoR/RcnR family member at the moment, it may seem that if is a novel DNA binding domain which does not involve the N-terminal region, the findings from this thesis and Chang *et al* (2014) may give a clue about a possible inverted role between N- and C-terminal regions (and vicinities). In *S. lividans* CsoR, residue Arg129 is located at the C-terminal region, and is suggested to be a DNA binding ligand. Arg129 is involved in a cross-tetramer interface interaction with Thr80 observed at the quasi Cu(I)-bound state at pH 6, which is suggested to not be able to interact with the DNA. In clade IV *G. thermodenitrificans* Cu(I)-CsoR structure the N-terminal region at the α 1 helix adopts an extended conformation and fold over the Cu(I) binding site region (Chang *et al*, 2014). From all reported *S. lividans* apo-CsoR structures

reported in this thesis in Chapters 2 and 3, no electron density for the N-terminal region was observed. An attempt to construct and over-express a truncated N-terminal CsoR involving the missing residues from the apo structure at pH 4 was performed without success. For *S. lividans* CsoR, the construction of a new truncation mutant with fewer residues absent from the N-terminal region may be possible, but it has to be taken in consideration to predict protein solubility issues according to the residues to be chosen and purification buffers.

In Chapter 4, kinetic studies of Cu(I) and Ni(II) binding to *S. lividans* CsoR, it is apparent that of the metal binding X-Y-Z fingerprint residues, Cys104 (Z) binds first to Cu(I). This finding contradicts a previous prediction, where based on the ionization properties of the two Cys residues, Cys75 was suggested to initiate initial Cu(I) interaction in the complex formed with a Cu(I)-bound CopZ (Chaplin *et al*, 2015). The interpretation here of Cu(I) binding first to Cys104 also strengthens the suggested mechanism of conformational switching between the apo- and Cu(I)-bound states highlighted in Chapter 2. Structural evidence suggested that Cu(I) would bind first to Cys104 in the apo-state, driving it into the vicinity of the Cys75' and His100 ligands to complete the first coordination Cu(I) sphere, which at the same time causes disruption to local secondary structure which is transmitted throughout the homotetramer causing disruption or disassembly of the DNA bound complex. *In vitro* *S. lividans* CsoR can accommodate Cu(I) in the X-Y-Z position and from the interpretation of displacement studies it also capable of binding Ni(II) in a binding site other than the X-Y-Z fingerprint that utilizes His103. These kinetic findings, combined with the results for the Cu(I) static

titrations from H103A and C104A mutants, combined with previously reported for C75A and H100A mutants (Dwarakanath *et al*, 2012), supports evidence that Cys75', His100 and Cys104 are suggested to be Cu(I) binding residues from the primary coordination shell X-Y-Z fingerprint motif in *S. lividans* CsoR and further attempts to crystallise in its Cu(I)-bound form will then confirm this hypothesis.

It has been suggested that beyond the first coordination shell W- X-Y-Z fingerprint motif, a secondary one denominated A-B-C which may have a role in aiding metal binding in CsoR proteins (Foster *et al*, 2014a). Sequence alignment revealed A and B residues to be Tyr and Glu respectively and in the case of *S. lividans* CsoR are residues Tyr74 and Glu122 (Figure 1.12). In the apo structure at pH 4, a H-bound network formed by His103 - sulfate ion – His100- water - Glu122 and Tyr74' (adjacent to Cys75') was observed (Dwarakanath *et al*, 2012). One future direction in further exploration of the metal binding properties of *S. lividans* CsoR can be taken by exploring the role of these residues combined with His37 located at the N-terminal from a structural and kinetic perspective as done in this thesis.

Taking in consideration the flexible nature of protein structures due to the nature of their chemical bond interactions and their imperfections in steric selection are one of the challenges to overcome under *in vivo* conditions (Foster *et al*, 2014b). Considerable changes in metal site geometry can also inactivate protein function, so it is important to explore this further in this field of metalloprotein research. With the economical important of *Streptomyces* and their Cu-dependent secondary metabolites production, the better understanding of the interplay between Cu(I), CsoR and the *csor* regulon is

important for further exploration of copper homeostasis with a biotechnological approach.

References

Anderson, A.S., Wellington, E. M.H. (2001) The taxonomy of *Streptomyces* and related genera. *Intl J Sys Evol Microbiol*, 51, 797-814.

Andrews, S.C., Robinson, A. K., Rodríguez-Quiñones, F. (2003) Bacterial ion homeostasis. *FEMS Microbiol Rev*, 27, 215-237.

Arunkumar, A.I., Campanello, G.C, Giedroc, D.P. (2009) Solution structure of a paradigm ArsR family zinc sensor in the DNA-bound state. *Proc Nat Acad Sci USA*, 106, 18177-18182.

Baker, J.; Sengupta, M.; Jayasawl, R.K.; Morrissey, J.A. (2011) The *Staphylococcus aureus* CsoR regulates both chromosomal and plasmid-encoded copper resistance mechanisms. *Environ Microbiol*, 13, 2495-2507.

Banci, L., Bertini, I., Cantini, F., Ciofi-Baffoni, S., Cavet, J.S., Dennison, C., Graham, A.I., Harvie, D.R., Robinson, N.J. (2007) NMR structural analysis of cadmium sensing by winged helix repressor CmtR. *J Biol Chem*, 282, 30181-30188.

Battye, T. G., Kontogiannis, L., Johnson, O., Powell, H. R., and Leslie, A. G. (2011) iMOSFLM. A new graphical interface for diffraction-image processing with MOSFLM. *Acta Crystallogr. D*, 67, 271–281.

- Bérdy, J. (2005) Bioactive microbial metabolites. J Antibiot. , 58, 1-26.**
- Bibb, M. (1996) The regulation of antibiotic production in *Streptomyces coelicolor* A3(2). Microbiol., 142, 1335-1344.**
- Bloom, S.L. , Zamble, D.B. (2004) Metal-selective DNA-binding response of *Escherichia coli* NikR. Biochem. , 43, 10029-10038.**
- Blundell, K. L. I. M., Wilson, M. T., Svistunenko, D.A., Vijgenboom, E., Worrall, J. A. R. (2013) Morphological development and cytochrome c oxidase activity in *Streptomyces lividans* are dependent on the action of a copper bound Sco protein. Open Biol., 3, 120163.**
- Blundell, K. L. I. M., Hough, M. A., Vijgenboom, E., Worrall, J. A. R. (2014) Structural and mechanism insights into an extracytoplasmatic copper trafficking pathway in *Streptomyces lividans*. Biochem J, 459, 525-538.**
- Brown, N.L., Stoyanov, J.V., Kidd, S.P., Hobman, J.L. (2003) The MerR family of transcriptional regulators. FEMS Microbiol Rev, 27, 145-163.**
- Busenlehner, L.S., Weng, T., Penner-Hahn, J. E., Giedroc, D.P. (2002) Elucidation of Primary (α 3N) and Vestigial (α 5) Heavy Metal-binding Sites in *Staphylococcus aureus* pl258. J. Mol Biol., 319, 685-701.**

Busenlehner, L.S., Penella, M.A., Giedroc, D.P. (2003) The SmtB/ArsR family of metalloregulatory transcriptional repressors: structural insights into prokaryotic metal resistance. FEMS Microbiol Lett, 27, 131-143. (a)

Butler, M. S. (2005) Natural products to drugs: natural product derived compounds in clinical trials. Nat Prod Rep, 22, 162 – 195.

Campbell, D.R., Chapman, K.E., Waldron, K.J., Tottey, S., Kendall, S., Cavallaro, G., Andreini, C., Hinds, J., Stoker, N.G., Robinson, N.J., Cavet, J.S. (2007) Mycobacterial cells have dual nickel-cobalt sensors. J Biol Chem, 32298-32310.

Cavet, J.S. , Meng, W., Penella, M. A., Appelhoff, R.J., Giedroc, D.P., Robinson, N.J. (2002) A nickel-cobalt sensing ArsR-SmtB family repressor. J Biol Chem, 277, 38441-38448.

Cavet, J. S. , Graham, A. I., Meng, W., Robinson, N.J. (2003) A cadmium-lead sensing ArsR-SmtB repressor with novel sensory sites. J Biol Chem, 278, 44560-44566.

Chalis, G. L., Hopwood, D.A. (2003) Synergy and contingency as driving forces for the evolution of multiple secondary metabolite production by Streptomyces species. Proc Nat Acad Sci USA, 100, 14555-14561.

Chang, F. M., Lauber, M. A., Running, W. E., Reilly, J. P., Giedroc, D. P. (2011) Ratiometric pulse-chase amidination mass spectrometry as a probe of biomolecular complex formation. *Anal. Chem.* , 83, 9092-9099.

Chang, F.M., Coyne, H.J., Cubillas, C., Vinuesa,P., Fang, X; Ma, Z., Ma, D., Helmann, J.D.,Garcia-de los Santos, A., Wang, Y.X., Dann, C.E. 3rd, Giedroc, D.P. (2014) Cu(I)-mediated allosteric switching in a copper-sensing operon repressor (CsoR). *J Biol Chem*, 289, 19204-19217.

Chang, F. M., Martin, J. E., Giedroc, D.P. (2015) Electrostatic occlusion and quarternary structural ion paring are key determinants of Cu(I)-mediated allostery in the copper-sensing operon repressor (CsoR). *Biochem.*, 54, 2463-2472.

Changela, A., Chen, K., Xue, Y., Holschen, J., Otten, C.E., O'Halloran, T.V., Mondragón, A. (2003) Molecular basis of metal-ion selectivity and zeptomolar sensitivity by CueR. *Science*, 301, 1383-1387.

Chaplin, A.K., Tan, B.G., Vijgenboom, E., Worrall, J.A.R. (2015) Copper trafficking in the CsoR regulon of *Streptomyces lividans*. *Metallomics*, 7, 145-155.

Chen, C.S., White, A., Love, J., Murphy, J.R., Ringe, D. (2000) Methyl groups of thymine bases are important for nucleic acid recognition by DtxR. *Biochem*, 39, 10397-10407.

Collaborative Computational Project, Number 4 (1994) The CCP4 suite: programs for protein crystallography. *Acta Crystallogr D* 50, 760-763.

Contreras, M., Thiberge, J-M, Mandrand-Berthelot, M-A., Labigne, A. (2003) Characterisation of the roles of NikR, a nickel-responsive pleiotropic autoregulator of *Helicobacter pylori*. *Mol Microbiol.*, 49, 947-963.

Cook, W.J., Kar, S.R., Taylor, K.B., Hall, L.M. (1998) Crystal structure of the cyanobacterial metallothionein repressor StmB: a model for metalloregulatory proteins. *J.Mol Biol*, 275, 337-346.

Corbett, D.; Schuler, S.; Glenn, S. ; Andrew, P.W.; Roberts, I.S. (2011) The combined actions of the copper-responsive repressor CsoR and copper-metallochaperone CopZ modulate CopA-mediated copper efflux in the intracellular pathogen *Listeria monocytogenes*. *Mol Microbio.*, 81, 457-472.

Coyne III, H.J.; Giedroc, D.P. (2012) Backbone resonance assignments of the homotetrameric (48 kD) copper sensor CsoR from *Geobacillus thermodenitrificans* in the apo- and Cu(I)-bound states: insights into copper-mediated allostery. *Biomol NMR Assign.*, 7, 279-283.

Cruz-Morales, P.; Vijgenboom, E.; Iruegas-Bocardo, F.; Girard, G.; Yáñez-Guerra, L.A.; Ramos-Aboites, H.E.; Pernodet, J.; Anné, J.; van

Wezel, G.P.; Barona-Gomez, F. (2013) The genome sequence of *Streptomyces lividans* 66 reveals a novel tRNA-dependent peptide biosynthetic system within a metal-related genomic island. *Genome Biol Evol.*, 5, 1165-1175.

D'Aquino, J.A., Tetenbaum-Novatt, J., White, A., Berkovitch, F. Ringe, D. (2005) Mechanism of metal ion activation of the diphtheria toxin repressor DtxR. *Proc Natl Acad Sci, USA* 102, 18408-18413.

Davis, A. V., O'Halloran, T. V. (2008) A place for thioether chemistry in cellular copper ion recognition and trafficking. *Nat Chem Bio*, 4, 148-151.

Davis, I.W., Leaver-Fay, A., Chen, V.B., Block, J.N., Kapral, G.J., Wang, X, Murray, L.W., Arendall, W.B., 3rd, Snoeyink, J., Richardson, J.S., Richardson, D. C. (2007) MolProbity: all-atom contacts and structure validation for proteins and nucleic acids. *Nucleic Acids Res.* , 35, W375-383.

De Pina, K., Desjardin, V. , Mandrand-Berthelot, M., Giordano, G., Wu, L. (1999) Isolation and characterisation of the nikR gene encoding a nickel-responsive regulator in *Escherichia coli*. *J Bacteriol.* ,181, 670-674.

Dosanjh, N., Michel, S.L.J. (2006) Microbial nickel metalloregulation: NikRs for nickel ions. *Curr Opin Chem Biol*, 10, 123-130.

Dupont, C. L., Grass, G., Rensing, C. (2011) Copper toxicity and the origin of bacterial resistance- new insights and applications. *Metallomics*, 3, 1109- 1118.

Dwarakanath, S., Chaplin, A.K., Hough, M.A., Rigali, S., Vijgenboom, E., Worrall, J.A.R. (2012) The response to copper stress in *Streptomyces lividans* extends beyond genes under the direct control of a copper sensitive operon repressor protein (CsoR). *J Biol Chem*, 187, 17833-17847.

Eicken, C., Penella, M.A., Chen, X., Koshlap, K.M., VanZile, M.L., Sacchettini, J.C., Giedroc, D.P. (2003) A metal-ligand mediated intersubunit allosteric switch in related SmtB/ArsR zinc sensor proteins. *J Mol Biol*, 333, 683-695.

Emsley, P., and Cowtan, K. (2004) Coot.Model-building tools for molecular graphics. *Acta Crystallogr. D60*, 2126–2132

Escolar, L., Pérez-Martín, J., de Lorenzo, V. (1999). Opening the iron box: transcriptional metalloregulation by the Fur protein. *J Bacteriol.* , 181, 6223-6229.

Evans, P. (2006) Scaling and assessment of data quality. *Acta Crystallogr. D62*, 72–82

Festa, R. A., Jones, M.B., Butler-Wu, S. , Sinsimer, D., Gerads, R., Bishai, W.R., Peterson, S.N., Darwin, K.H. (2011) A novel copper-responsive regulon in *Mycobacterium tuberculosis*. Mol Microbiol. ,79, 133-148.

Frantz, B., O' Halloran, T.V. (1990) DNA distortion accompanies transcriptional activation by the metal-responsive gene-regulatory protein MerR. Biochem, 29, 4747-4751.

Foster, A. W., Patterson, C. J., Pernil, R., Hess, C. R., Robinson, N. J. (2012) Cytosolic Ni(II) sensor in cyanobacterium: nickel detection follows nickel affinity across four families of metal sensors. J Biol Chem., 287, 12142-12151.

Foster, A.W., Osman, D., Robinson, N.J. (2014) Metal preferences and metallation. J Biol Chem, 289, 28095-28103. (a)

Foster, A.W., Pernil, R., Hess, C.R., Robinson, N.J. (2014) Metal specificity of cyanobacterial nickel-responsive represso InrS: cells maintain zinc and copper below the detection threshold for InrS. Mol Microbiol, 92, 797-812 (b)

Foster, T.J., Ginnity, F. (1985) Some mercurial resistance plasmids from different incompatibility groups specify *merR* regulatory functions that

both repress and induce the *mer* operon of plasmid R100. *J Bacteriol.*, 162, 773-776.

Gaballa, A. , Cao, M., Helmann, J.D. (2003) Two MerR homologues that affect copper induction of the *Bacillus subtilis copZA* operon. *Microbiol.*, 149, 3413-3421.

Gaggelli, E., Kozolowski, H.; Valensin, D.; Valensin, G. (2006) Copper homeostasis and neurodegenerative disorders (Alzheimer's, prion, and Parkinson's disease and amyotrophic lateral sclerosis). *Chem Rev*, 6, 1995 – 2044.

Giedroc, D.P.; Arunkumar, A.I. (2007) Metal sensor proteins: nature's metalloregulated allosteric switches. *Dalton Trans.*, 29, 3107-3120.

Glasfeld, A., Gueldon, E., Helmann, J.D., Brennan, R.G. (2003) Structure of the manganese-bound manganese transport regulator of *Bacillus subtilis*. *Nat Struct Biol*, 10, 652-657.

Grossoehme, N; Kehl-Fie, Thomas E.; Ma, Z.; Adams, K.W.; Cowart, D.M.; Scott, R.A.; Skaar, E.P.; Giedroc, D.P. (2011) Control of copper resistance and inorganic sulfur metabolism by paralagous regulators in *Staphylococcus aureus*. *J. Biol Chem*, 286, 13522-13531.

Gueldon, E., Helmann, J.D. (2003) Origins of metal ion selectivity in the DtxR/MntR family of metalloregulators. Mol Microbiol., 48, 495-506.

Guo, H., Johs, A., Parks, J.M., Olliff, L., Miller, S.M., Summers, A.O., Liang, I., Smith, J.C. (2010) Structure and conformational dynamics of the metalloregulator MerR upon binding of Hg(II). J Mol Biol. , 398, 555-568.

Hantke, K. (2001) Iron and metal regulation in bacteria. Curr Opin Microbiol., 4, 172-177.

Higgins, K. A., Chivers, P. T., Maroney, M. J. (2012) Role of the N-terminus in determining metal-specific responses in the E. coli Ni- and Co-responsive metalloregulator, RncR. J Am Chem Soc, 134, 7081-7093.

Higgins, K.A. ; Giedroc, D.P. (2014) Insights into protein allostery in the CsoR/RcnR family of transcriptional repressors. Chem Lett. , 5, 20 - 25.

Hobman, J.L. (2007) MerR family transcription activators: similar designs, different specificities. Mol Microbiol., 63, 1275-1278.

Hodgkinson, V. , Petris, M.J. (2012) Copper homeostasis at the host-pathogen interface. J Biol Chem, 287, 13549-13555.

Irving, H., Williams, R. J.P. (1948) Order of stability of metal complexes. *Nature*, 162, 746-747.

Iwig, J. S.; Rowe, J. L., Chivers, P.T. (2006) Nickel homeostasis in *Escherichia coli* – the rcnR-rcnA efflux pathway and its linkage to NikR function. *Mol Microbiol.*, 62, 252 – 262.

Iwig, J.S.; Leitch, S.; Herbst, M.J.; Chivers, P.T. (2008) Ni(II) and Co(II) sensing by *Escherichia coli* RcnR. *J Am Chem Soc*, 130, 7592-7606.

Keijser, B.J.F., van Wesel, G.P., Canters, G.W., Kieser, T., Vijgenboom, E. (2000) The ram-dependence of *Streptomyces lividans* differentiation is bypassed by copper. *J. Mol. Microbiol. Biotechnol.*, 2, 565-574.

Lee, C. W., Chakravorty, D. K., Chang, F-M J., Reyes-Caballero, H., Ye, Y., Merz, Jr, K. M., Giedroc, D. P. (2012) Solution structure of *Mycobacterium tuberculosis* NmtR in the apo state: insights into Ni(II)-mediated allostery. *Biochem*, 51, 2619-2629.

Lee, J.W., Helmann, J.D. (2007) Functional specialization within the Fur family of metalloregulators. *Biometals*, 20, 485-499.

Liu, T., Nakashima, S., Hirose, K., Shibasaki, M., Katsuhara, M., Ezaki, B., Giedroc, D.P., Kasamo, K. (2004) A novel cyanobacterial StmB/ArsR family repressor regulates the expression of a CPx-ATPase and a

metallothionein in response to both Cu(I)/Ag(I) and Zn(II)/Cd(II). *J Biol Chem*, 279, 17810-17818.

Liu, T., Ramesh, A., Ma, Z., Ward, S.K., Zhang, L., George, G.N., Talaat, A.M., Sacchettini, J.C., Giedroc, D.P. (2007) CsoR is a novel *Mycobacterium tuberculosis* copper-sensing transcriptional regulator. *Nat Chem Biol.*, 3, 60-68.

Liu, T., Chen, Z., Ma, Z., Shokes, J., Hemmingsen, L., Scott, R.A., Giedroc, D.P. (2008) A Cu(I)-sensing ArsR family metal sensor protein with a relaxed metal selectivity profile. *Biochem.*, 47, 10564-10575.

Luebke, J. L. , Shen, J., Bruce, K. E., Kehl-Fie, T. E., Peng, H., Skaar, E. P., Giedroc, D.P. (2014) The CsoR-like sulfurtransferase repressor (CstR) is a persulfide sensor in *Staphylococcus aureus*. *Mol Microbiol*, 94, 1346 – 1360.

Lund, P.A. , Ford, S.J., Brown, N.L. (1986) Transcription regulation of the mercury-resistance genes transposon Tn501. *J Gen Microbiol*, 132, 465-480.

Ma, Z., Cowart, D.M., Scott, R.A., Giedroc, D.P. (2009) Molecular insights into the metal selectivity of the copper (I) sensing repressor CsoR from *Bacillus subtilis*. *Biochem*, 48, 3325-3334. (a)

Ma, Z; Jacobsen, F.E.; Giedroc, D.P. (2009) Coordination chemistry of bacterial metal transport and sensing. *Chem Rev*, 109, 4644-4681 (b)

Macomber, L., Imlay, J.A. (2009) The iron-sulfur clusters of dehydratases are primary intracellular targets of copper toxicity. *Proc Nat Acad Sci USA*, 106, 8344-8349.

Macomber, L., Rensing, C., Imlay, J.A. (2007) Intracellular Copper Does Not Catalyze the Formation of Oxidative DNA Damage in *Escherichia coli*. *J Bacteriol.*, 189, 1616-1626.

McCoy, A.J., Grosse-Kunstleve, R.W. , Adams, P.D., Winn, M.D., Storoni, L.C., Read, R.J. (2007) Phaser crystallography software. *J. Appl Cryst*, 40, 658-674.

Moore, C. M., Helmann, J.D. (2005) Metal ion homeostasis in *Bacillus subtilis*. *Curr Opin Microbiol.*, 8, 188-195.

Morby, A.P., Turner, J.S., Huckle, J.W., Robinson, N.J. (1993) StmB is a metal-dependant repressor of the cyanobacterial metallothionein gene *stmA*: identification of a Zn inhibited DNA-protein complex. *Nuc Acids Res.* , 21, 921-925.

Murshudov, G.N., Skubak, P., Lebedev, A.A.; Pannu, N.S., Nicholls, R.A., Winn, M.D.; Long; Vagin, A.A. (2011) REFMAC5 for the refinement of macromolecular crystal structures. Acta Crystallogr. D67, 355-367.

Odermatt, A., Solioz, M. (1995) Two trans-acting metalloregulatory proteins controlling expression of the copper ATPases of *Enterococcus hirae*. J Biol Chem, 270, 4349-4354.

O'Halloran, T.V., Walsh, C. (1987) Metalloregulatory DNA-binding protein encoded by the *merR* gene: isolation and characterization. Science, 235, 211-214.

Keijser, C., Méndez, C., Salas, J.A. (2011) Molecular insights on the biosynthesis of antitumour compounds by actinomycetes. Microbiol Biotechnol, 4, 144-164.

Osman, D., Cavet, J.S. (2008) Copper homeostasis in bacteria. Adv Appl Micro Bio., 65, 217-247.

Otten, F.W., Otten, C.E., Hale, J., O'Hallaran, T.V. (2000) Transcriptional activation of an *Escherichia coli* copper efflux regulon by the chromosomal MerR homologue, CueR. J Biol Chem, 275, 31024-31029.

Penella, M.A.; Shokes, J.E.; Coper, N.J.; Scott, R.A., Giedroc, D.P. (2003) Structural elements of metal selectivity in metal sensor proteins. *P Natl Acad Sci USA*, 100, 37-13-3718.

Penella, M.A., Giedroc, D.P (2005) Structural determinants of metal selectivity in metal-responsive transcriptional regulators. *Biometals* , 18, 413 – 428.

Pohl, E., Haller, J.C., Mijovilovich, A., Meyer-Klaucke, W., Garman, E; Vasil, M.L. (2003) Architecture of a protein central to ion homeostasis: crystal structure and spectroscopic analysis of the ferric uptake regulator. *Mol Microbiol.*, 47, 903-915.

Posey, J. E., Hardham, J. M. , Norris, S. J., Gherardini, F. C. (1999) Characterisation of a manganese-dependent regulatory protein, TroR, from *Treponema pallidum*. *Proc. Natl. Acad. Sci. USA*, 96, 10887–10892.

Que, Q., Helmann, J.D. (2000) Manganese homeostasis in *Bacillus subtilis* is regulated by MntR, a bifunctional regulator related to the diphtheria toxin repressor family of proteins. *Mol Microbiol*, 35, 1454-1468.

Rensing, C., Grass, G. (2003) Escherichia coli mechanism of copper homeostasis in a changing environment. *FEMS Microbiol Rev*, 27, 197-213.

Reyes-Caballero, H.; Campanello, G.C.; Giedroc, D.P. (2011) **Metalloregulatory proteins: metal selectivity and allosteric switching. Biophys Chem, 156, 103-114.**

Rubino, J.T., Franz, K.J. (2012) **Coordination chemistry of copper proteins: how nature handles a toxic cargo for essential function. J Inorg Biochem, 107, 129-143.**

Sakamoto, K. , Agari, Y., Agari, K., Kuramitsu, S., Shinkai, A. (2010) **Structural and functional characterisation of the transcriptional repressor CsoR from *Thermus thermophilus* HB8. Microbiol. , 156, 1993-2005.**

Schmitt, M.P. , Holmes, R.K. (1994) **Cloning, sequence, and footprinting analysis of two promoter/operators from *Corynebacterium diphtheriae* that are regulated by the diphtheria toxin repressor (DtxR) and iron. J Bacteriol, 176, 1141—1149.**

Schreiter, E.R., Sintchak, M.D., Guo, Y., Chivers, P.T., Sauer, R.T., Drennan, C.L. (2003) **Crystal structure of the nickel-responsive transcriptional factor NikR. Nat Struct Biol, 10, 794-799.**

Schreiter, E.R., Wang, S.C., Zamble, D.B., Drennan, C.L. (2006) NikR-operator complex structure and the mechanism of repressor activation by metal ions. *Proc. Natl. Acad. Sci. USA*, 103, 13676-13681.

Shi, X.; Festa, R.A.; Ioerger, T. R.; Butler-Wu, S.; Sacchettini, J.C.; Darwin, K.H.; Samanovica, M.I. (2014) The copper-responsive RicR regulon contributes to *Mycobacterium tuberculosis* virulence. *mBio*, 5, pii: e00876-13. doi: 10.1128/mBio.00876-13

Smaldone, G.T.; Helmann, J.D. (2007) CsoR regulates the copper efflux operon copZA in *Bacillus subtilis*. *Microbio*, 153, 4123-4128.

Solioz, M. , Stoyanov, J. V. (2003) Copper homeostasis in *Enterococcus hirae*. *FEMS Microbiol Rev*, 27, 183-195.

Solioz, M. , Abicht, H.K., Mermod, M.; Mancini, S. (2010) Response of Gram-positive bacteria to copper stress. *J Biol Inorg Chem*, 15, 3-14.

Spering, M. M. , Ringe, D., Murphy, J.R., Marletta, M.A. (2003) Metal stoichiometry and functional studies of the diphtheria toxin repressor. *Proc. Natl. Acad. Sci. USA*, 100,3808-3813.

Stoyanov, J.V., Hobman, J.L., Brown, N.L. (2001) CueR (Ybbl) of *Escherichia coli* is a MerR family regulator controlling expression of the copper exporter CopA. *Mol Microbiol.*, 39, 502 - 511.

Tan, B.G., Vijgenboom, E., Worrall, J.A.R. (2014) Conformational and thermodynamic hall marks of DNA operator site specificity in the copper sensitive operon repressor from *Streptomyces lividans*. *Nuc Acid Res.*, 42, 1326-1340.

Traoré, D. A. K. , Ghazouani, A. E., Ilango, S., Dupuy, J., Jacquamet, L., Caux-Thang, C., Duarte, V., Latour, J. (2006) Crystal structure of the apo-PerR-Zn protein from *Bacillus subtilis*. *Mol Microbiol.*, 61, 1211-1219.

Van Wezel, G. P., McDowall, K.J. (2011) The regulation of the secondary metabolism of *Streptomyces*: new links and experimental advances. *Nat. Prod. Rep.* , 28, 1311-1333.

Xiao, Z., Donnelly, P. S., Zimmermann, M., and Wedd, A. G. (2008) Transfer of copper between bis(thiosemicarbazone) ligands and intracellular copper-binding proteins. insights into mechanisms of copper uptake and hypoxia selectivity, *Inorg Chem* 47, 4338-4347.

Waksman, S.A. , Henrici, A.T. (1943) The nomenclature and classification of the actinomycetes. *J. Bacteriol.* , 46, 337-341.

Waldron, K.J.; Robinson, N.J. (2009) How do bacterial cells ensure that metalloproteins get the correct metal? *Nat Rev Microbio.*, 6, 25-35.

Waldron, K. J., Rutherford, J. C., Ford, D., and Robinson, N. J. (2009)

Metalloproteins and metal sensing, *Nature* 460, 823-830.

Wang, S. C., Dias, A .V., Bloom, S.L., Zamble, D.B. (2004) Selectivity of metal binding and metal-induced stability of *Escherichia coli*. *Biochem.*, 43, 10018-10028.

Wang, Y., Hemmingsen, L., Giedroc, D.P.(2005) Structural and functional characterisation of *Mycobacterium tuberculosis* CmtR, a Pb^{II}/Cd^{II}-sensing StmB/ArsR metalloregulatory repressor. *Biochem.*, 44, 8976-8988.

Worrall, J.A.R.; Vijgenboom, E. (2010) Copper mining in *Streptomyces*: enzymes, natural products and development. *Nat Prod Rep*, 27, 742-756.

Wu, J., Rosen, B.P. (1993) Metalloregulated expression of the *ars* operon. *J Biolol Chem*, 268, 52-58.

Ye, J., Kandegedara, A., Martin, P., Rosen, B.P. (2005) Crystal structure of the *Staphylococcus aureus* pl258 CadC Cd(II)/Pb(II)/Zn(II)-responsive repressor. *J Bacteriol.*, 187, 4214-4221.

Appendix

Structural insights into conformational switching in the copper metalloregulator CsoR from *Streptomyces lividans*

Tatiana V. Porto, Michael A. Hough and Jonathan A. R. Worrall

Acta Cryst. (2015). D71, 1872–1878